
[All ETDs from UAB](#)

[UAB Theses & Dissertations](#)

1999

A Mossbauer spectroscopic study of iron-rich deposits of hydrothermal springs as Martian analogues.

Manson LaShawn Wade
University of Alabama at Birmingham

Follow this and additional works at: <https://digitalcommons.library.uab.edu/etd-collection>

Recommended Citation

Wade, Manson LaShawn, "A Mossbauer spectroscopic study of iron-rich deposits of hydrothermal springs as Martian analogues." (1999). *All ETDs from UAB*. 6313.
<https://digitalcommons.library.uab.edu/etd-collection/6313>

This content has been accepted for inclusion by an authorized administrator of the UAB Digital Commons, and is provided as a free open access item. All inquiries regarding this item or the UAB Digital Commons should be directed to the [UAB Libraries Office of Scholarly Communication](#).

INFORMATION TO USERS

This manuscript has been reproduced from the microfilm master. UMI films the text directly from the original or copy submitted. Thus, some thesis and dissertation copies are in typewriter face, while others may be from any type of computer printer.

The quality of this reproduction is dependent upon the quality of the copy submitted. Broken or indistinct print, colored or poor quality illustrations and photographs, print bleedthrough, substandard margins, and improper alignment can adversely affect reproduction.

In the unlikely event that the author did not send UMI a complete manuscript and there are missing pages, these will be noted. Also, if unauthorized copyright material had to be removed, a note will indicate the deletion.

Oversize materials (e.g., maps, drawings, charts) are reproduced by sectioning the original, beginning at the upper left-hand corner and continuing from left to right in equal sections with small overlaps. Each original is also photographed in one exposure and is included in reduced form at the back of the book.

Photographs included in the original manuscript have been reproduced xerographically in this copy. Higher quality 6" x 9" black and white photographic prints are available for any photographs or illustrations appearing in this copy for an additional charge. Contact UMI directly to order.

UMI

A Bell & Howell Information Company
300 North Zeeb Road, Ann Arbor MI 48106-1346 USA
313/761-4700 800/521-0600

**A MÖSSBAUER SPECTROSCOPIC STUDY OF IRON-RICH DEPOSITS OF
HYDROTHERMAL SPRINGS AS MARTIAN ANALOGUES**

by

MANSON L. WADE

A DISSERTATION

**Submitted to the graduate faculty of The University of Alabama at Birmingham,
in partial fulfillment of the requirements for the degree of
Doctor of Philosophy**

BIRMINGHAM, ALABAMA

1999

UMI Number: 9923504

UMI Microform 9923504
Copyright 1999, by UMI Company. All rights reserved.

**This microform edition is protected against unauthorized
copying under Title 17, United States Code.**

UMI
300 North Zeeb Road
Ann Arbor, MI 48103

ABSTRACT OF DISSERTATION
GRADUATE SCHOOL, UNIVERSITY OF ALABAMA AT BIRMINGHAM

Degree Ph.D. Program Physics

Name of Candidate Manson LaShawn Wade

Committee Chair David G. Agresti

Title A Mössbauer Spectroscopic Study of Iron-Rich Deposits of Hydrothermal Springs as Martian Analogues

In this work, results are reported of Mössbauer analysis focused on a suite of samples collected systematically along the outflow channel from an iron-rich hydrothermal vent mound in the Chocolate Pots area of Yellowstone National Park in the context of Mars exploration. Similar hydrothermal spring systems may well have been present on an early Mars and could have harbored primitive life. Mössbauer spectroscopy was chosen as the primary investigative technique in this study because of its ability to discriminate among the iron-bearing minerals in these samples. Those on the surface and near the vent are identified as predominantly ferrihydrite, $\text{Fe}_5\text{HO}_8 \cdot 4\text{H}_2\text{O}$ or $5\text{Fe}_2\text{O}_3 \cdot 9\text{H}_2\text{O}$. Subsurface samples, which seem to have been altered by either inorganic and/or biological processes, exhibit spectral signatures that include nontronite $[(\text{Ca},\text{Na})_{0.66}\text{Fe}^{3+}_4\text{Si}_{7.34}\text{Al}_{0.66}\text{O}_{20}(\text{OH})_4, n\text{H}_2\text{O}]$, in the smectite clay mineral group, hematite ($\alpha\text{-Fe}^{3+}_2\text{O}_3$), small-particle/nanophase goethite ($\alpha\text{-Fe}^{3+}\text{OOH}$), and siderite ($\text{Fe}^{2+}\text{CO}_3$). Evidence is presented that all these minerals, including those with the nanophase property, can have multi-billion year residence times and thus survive from their possible production in a putative early Martian hydrothermal environment to present day. Mössbauer spectroscopy will be a planned component of the instrument suite included on the 2001 Mars Surveyor Athena Rover mission. It is hoped that this work will aid in the

use of this instrument, in the service of exobiology, and in helping to identify hydrothermal sediments and samples suitable for subsequent return to Earth.

DEDICATION

This work is dedicated to both my parents and my loving wife. To my dad and my mom, especially, thanks for all that you have done in support of my endeavors. You have always been there when needed, and yet were able to teach the very important lesson of independence and self-reliance. You always taught me that without God nothing was possible. Well, without your love and support, achievement of this would not have been possible. I love you both. To my loving and supportive wife, thanks for your patience, love, and understanding. You are the only one who truly understands all the sacrifices and pressures involved. Thanks for helping me keep my sanity through all the really tough times and convincing me to stick it out when I was truly considering throwing in the towel. You are truly my rock and inspiration. Thanks, I love you, and I'll save some of that midnight oil for you.

ACKNOWLEDGEMENTS

I would like to gratefully acknowledge the time, patience, understanding, and assistance given to me by Dr. David G. Agresti, my graduate advisor. He has been a parent of sorts because I know I have acted like a spoiled little child at times. I have always heard that the only difference between a pat on the back and a kick in the behind is a couple of inches. Thanks for understanding and, more importantly, teaching me that difference. He has continually and consistently been one of my greatest advocates. For that I thank you. I would like to give a special heart-felt thanks to Dr. Thomas J. Wdowiak not only for his invaluable insight on this project and his confidence in me as a scientist, but also for his foresight. I thank Dr. Robin Griffin (Department of Materials Science and Engineering, UAB), for her undying support and guidance during the completion of this project. She always seemed to be genuinely glad to see me even during times when I know I was being a pest with these strange samples. She always had a smile for me and found time to devote to my problems and concerns. For these reasons, I truly consider him a friend and I hope that we can find other opportunities to work together in the future; she is the consummate professional. I would also like to thank Dr. Jack Farmer (NASA Ames Research Center (SETI)) for all of his time and effort in providing samples and lending his expertise in the areas of terrestrial thermal systems and exobiology. I would like to thank the remaining members of my Ph.D. graduate committee, Dr. Ed Wills and Dr. Denny Bearce (Geology Dept., UAB), for their assistance and guidance.

I am grateful to all members of the UAB Physics Department's faculty and staff for their assistance and support. I would like to give special thanks to Dr. David Shealy for giving me the opportunity and to Jerry Sewell for all his help in making the completion of this project possible and trusting me with his equipment. I would also wish to thank Dr. Richard V. Morris (NASA, Johnson Space Center) for his insight. Thanks to all of the secretaries who have given of themselves, especially Donna Andrews, a friend who made adjusting to a new city without family and friends easier, and Kathy Baier, who is a complete joy to work with, making everyday life in the department more bearable for all.

I would like to once again thank my wife, parents, family, and friends for all their support and sacrifices that have allowed me to pursue this degree. Their belief in me is the true measure of success. To my extended family at the Alabama School of Fine Arts and fellow graduate students, thanks for the patience, understanding, and the camaraderie. The friendships formed with Kervin Evans, Lody Armendarez, and Luke Beegle, especially, shall be treasured.

Finally, I am very grateful for the financial and overall support given to me by the UAB Graduate School over the years, especially by Wanda Jordan and Julie Bryant, both as a Comprehensive Minority Faculty Development Program Fellow (CMFDP) and as friends. Again, special thanks to Dr. David Agresti and Dr. Thomas Wdowiak, whose participation in the work was funded by a NASA exobiology grant.

TABLE OF CONTENTS

	<u>Page</u>
ABSTRACT.....	ii
DEDICATION.....	iv
ACKNOWLEDGEMENTS.....	v
LIST OF TABLES.....	ix
LIST OF FIGURES.....	x
CHAPTER	
1 INTRODUCTION.....	1
2 THEORY.....	6
A. Mössbauer Spectroscopy.....	6
1. Isomer “Center” Shift.....	9
2. Electric Quadrupole Splitting.....	10
3. Magnetic Hyperfine (Zeeman) Splitting.....	15
B. X-ray Powder Diffraction (XRPD).....	19
3 EXPERIMENTAL METHODS.....	25
A. Samples and Preparation.....	25
B. Mössbauer Spectroscopy.....	26
C. X-ray Powder Diffraction.....	29
D. Calibration.....	29
4 MÖSSBAUER SPECTRAL ANALYSIS.....	34
5 RESULTS AND DISCUSSION.....	38
A. Manitou Springs and Obsidian Pool.....	38
B. “Surface” Samples.....	41
C. “Subsurface” Sample.....	43
6 CONCLUSIONS.....	71

TABLE OF CONTENTS (Continued)

APPENDIX

A	THEORETICAL SUPPLEMENT.....	74
B	X-RAY POWDER DIFFRACTION SPECTRAL ANALYSIS.....	81
	REFERENCES.....	89

LIST OF TABLES

<u>Table</u>		<u>Page</u>
1	Fe ⁵⁷ Excited-State Transition Percentages and Half-Lives.....	8
2	Relative Transmission Probabilities for Specific Photon Directions Relative to B_{hf}	17
3	Summary of Nuclear-Electronic Properties and Interactions.....	18
4	Chocolate Pots Mössbauer Samples.....	26
5	Quantities Used for the Production of Mössbauer Absorbers.....	27
6	Calibration Results for Peak Positions (mm/s) of Combined Hematite and Natural Iron Foil (Experimental and Standards) with deviations.....	30
7	Manitou Springs Mössbauer Parameters.....	39
8	Obsidian Pool Mössbauer Parameters.....	40
9	Mössbauer Parameters for Surface Samples at 300 K.....	42
10	Sample 6C1 Mössbauer Parameters.....	43
11	Sample 2C1 Mössbauer Parameters.....	44
12	Sample 2C3 Mössbauer Parameters.....	46

LIST OF FIGURES

<u>Figure</u>		<u>Page</u>
1	Mössbauer spectra of chert-stromatolite showing the characteristic disappearance or movement of the siderite peak at low temperature.....	5
2	Illustration showing the nuclear resonance effect for Fe ⁵⁷	21
3	Co ⁵⁷ nuclear decay diagram (706,366 levels omitted for clarity).....	21
4	Illustration of the nuclear charge distribution and the electron densities for s and p-state.....	22
5	Energy level diagram showing the effect of the isomer shift.....	22
6	Illustration showing exaggerated nuclear shape with the two possible orientations that the nucleus may have for the nuclear spin state, I = 3/2 (⇒ m _I = ±3/2 (right), ±1/2 (left); e.g. ⁵⁷ Fe, first excited state).....	23
7	Energy level diagram showing the effect of the electric quadrupole.....	23
8	Energy level diagram showing the effect of the magnetic hyperfine splitting and isomer shift with a corresponding Mössbauer spectrum showing the magnetic sextet.....	24
9	Picture of vent mound collection site in Chocolate Pots region of Yellowstone.....	31
10	Plot showing variations in temperature, pH, and Eh versus distance from vent.....	31
11	Schematic diagram of the Mössbauer spectroscopy experiment.....	32
12	Picture of the harness housing the Mössbauer experiment, designed to isolate the sample chamber from the drive and detector and to minimize possible vibration.....	32

LIST OF FIGURES (Continued)

<u>Figure</u>		<u>Page</u>
13	Illustration of the powder x-ray diffraction experiment.....	33
14	Mössbauer spectra of Manitou Springs temperature sequence.....	49
15	Fit of Manitou Springs spectra at 300 K, 150 K, and 12 K.....	50
16	Mössbauer spectra for Obsidian Pool temperature sequence.....	51
17	Fit of Obsidian Pool 250 K Mössbauer spectrum showing component sites.....	52
18	Variation of B_{hf} with temperature for the Manitou Springs, Obsidian Pool, and a bulk goethite sample [<i>Mørup et al.</i> , 1983].....	53
19	Mössbauer spectra for the 2C core sample.....	54
20	Mössbauer spectra for the 3C core sample.....	55
21	Mössbauer spectra for the 5C core and 6C1 sample.....	56
22	Fits of the 6C1 and 2C1 Mössbauer spectra at 300 K.....	57
23	Fits of the 5C1-4 and 3C1 Mössbauer spectra at 300 K.....	58
24	Mössbauer spectra of the 6C1 temperature sequence.....	59
25	X-ray diffraction spectra for powdered 'surface' samples.....	60
26	Mössbauer spectra for the 2C3 temperature sequence.....	61
27	Fit of 2C3 sample at 300 K showing component spectra.....	62
28	Mössbauer spectra of the natural (Nova Scotia) siderite temperature sequence.....	63
29	Fit of the natural (Nova Scotia) siderite at 14 K.....	64

LIST OF FIGURES (Continued)

<u>Figure</u>		<u>Page</u>
30	Fit of the 2C3 sample at 14 K showing the component spectra.....	64
31	Variation of B_{hf} with temperature for the 2C3 (component), Nova Scotia, and a synthetic (pure) siderite.....	65
32	Variation of QS with temperature for the 2C3 (component), Nova Scotia, and a synthetic (pure) siderite.....	65
33	X-ray diffraction spectrum for the powdered 2C3 sample.....	66
34	Mössbauer spectra for the 2C2 sample temperature sequence.....	67
35	Mössbauer spectra for the 2C4 sample temperature sequence.....	68
36	X-ray diffraction spectra for powdered 2C core samples.....	69
37	X-ray diffraction spectra for powdered 3C core samples.....	70

CHAPTER 1

INTRODUCTION

Since Viking, advances in molecular biology have dramatically changed our view of phylogenetic relationships among living organisms on Earth. The universal tree of life derived from comparisons of genetic sequences found in 16S ribosomal RNA suggests that life can be subdivided into three major domains: bacteria, archaea, and eukarya. A number of authors have suggested that terrestrial life may have actually originated at high temperatures [*Corliss et al.*, 1981; *Baross and Hoffman*, 1985; *Russell et al.*, 1988; *Corliss*, 1990]. Using thermodynamic models, *Shock and Shulte* [in *Wade, et al.*, 1998] have shown that hydrothermal systems are indeed favorable environments for the synthesis of complex organic molecules. Could such hydrothermal environments have provided an environment for the synthesis of prebiotic building blocks for the origin of life on Mars or for the subsequent evolution of Martian life? Although a high temperature origin for terrestrial life is still debatable, the high biological productivity and rapid mineralization that are typical of thermal spring environments make them particularly favorable places for the preservation of a microbial fossil record. For this reason, hydrothermal deposits are regarded as important targets in exploring for fossil evidence of ancient Martian life [*Walter and Des Marais*, 1993; *Farmer and Des Marais*, 1994; *Farmer*, 1995].

Much of the surface of Mars is covered by deposits of fine-grained materials consisting of nanophase iron oxides, silicate mineraloids, and salts (see *Banin et al.*, 1997a). These authors have suggested that the elemental composition of the soils at the Viking and Pathfinder sites can be explained as the by-product of recent weathering of mafic volcanic rocks in the presence of acidic volatiles produced during periodic episodes of volcanism. The lack of surface water during the younger epochs of Martian history, along with low temperatures, is likely to have halted the transformation of metastable amorphous mineraloids to more ordered, crystalline mineral phases. In many places, thick deposits of such materials may overlie older deposits of aqueous sediments formed during the warmer, wetter period in Martian history. Could hydrothermal systems have been common on Mars during this earlier period?

On Earth, subaerial hydrothermal springs are common features of continental volcanic settings. Evidence suggests that volcanic terrain [*Mouginis-Mark et al.*, 1992 in *Wade et al.*, 1998] and hydrothermal systems may have been widespread on early Mars [*Farmer*, 1996]. It is suggested that hydrothermal systems on Mars may have evolved from water-dominated (neutral chloride surface springs) to vapor dominated (fumerolic) systems as the planet lost its atmosphere and surface water dried up. If widespread hydrothermal systems became progressively vapor dominated over time, this should be detectable by comparing differences in surface mineralogy for different ages of terrain.

A decade ago, the utility of miniature Mössbauer spectrometers as in situ instruments for landed spacecraft was recognized [*Morris et al.*, 1988, 1989a; *Shelfer*, 1992]. In addition, Mössbauer spectrometers would have a definite role to play in exobiological investigations because deposits of putative Martian hydrothermal environments would

likely be rich in iron, making them amenable to Mössbauer [Agresti and Wdowiak, 1992]. In fact, a Mössbauer spectrometer, employing the 14.4-keV resonance in ^{57}Fe and functioning in the backscatter mode, is a component of the Athena rover instrument suite to be launched to Mars as part of the NASA Mars Surveyor Program. Among the stated capabilities of the Mössbauer instrument is the ability to detect "nanophase and amorphous hydrothermal Fe minerals that could preserve biological materials" [Squyres, 1998].

Terrestrial hydrothermal springs, including deep-sea vents, harbor complex ecosystems that have evolved entirely on the basis of nutrients and energy supplied by vent effluent. Results have been previously reported on the Mössbauer investigation of samples [collected by *J.C. Alt*] from submarine hydrothermal vents ("black smokers") in an area of the East Pacific Rise [Agresti et al., 1994]. The iron-rich minerals were shown by scanning electron microscopy (SEM) to be associated with bacterial filaments [Alt, 1988]. Mössbauer spectra taken over a range of sample temperatures revealed that the material collected at active vents was amorphous. When a vent becomes inactive, the iron-rich amorphous coating crystallizes to a stable phase in which organic materials are oxidized, leaving behind a filament mold. In the deposits of inactive vents, the microbial fossils are preserved within nanophase (superparamagnetic) material.

There is evidence that Mössbauer signatures of hydrothermal deposits can survive for billions of years. A 2.09 billion year old, hematite-rich chert stromatolite from the Gunflint Iron Formation, Southern Ontario (Nolalu), PPRG #2443 [provided by *J.W. Schopf, UCLA*] has also been subjected to a Mössbauer temperature study. As temperature is decreased, the sample shows a characteristic Mössbauer signature

associated with the iron carbonate, siderite (discussed later in this work; Figure 1). Although the iron carbonate may not be organic in origin, its occurrence in this 2.09 billion-year-old rock strongly suggests a survival time for siderite in the billion-year time scale.

This work reports on a study of iron-rich hydrothermal springs as Martian analogues. Samples investigated were collected at Manitou Springs, CO, and in Yellowstone National Park. The study focuses on a suite of samples collected systematically along an outflow channel of this mound at East Chocolate Pots, Yellowstone National Park, over a range of temperature, pH, and Eh; a preliminary report appeared as *Agresti et al.* [1997].

The primary analytical technique employed was transmission iron Mössbauer spectroscopy, carried out over a range of cryogenic temperatures, supplemented by powder x-ray diffraction (XRPD), field emission scanning electron microscopy (FESEM), and energy dispersive x-ray (EDX) spectroscopy [*Wade et al.*, 1998].

Results of this work support the utility of a Mössbauer spectrometer as an in situ instrument that can prospect for ancient hydrothermal deposits on Mars. It has the potential for identifying exobiologically relevant samples to cache for delivery to Earth as part of the planned 2005 Mars Surveyor sample return mission.

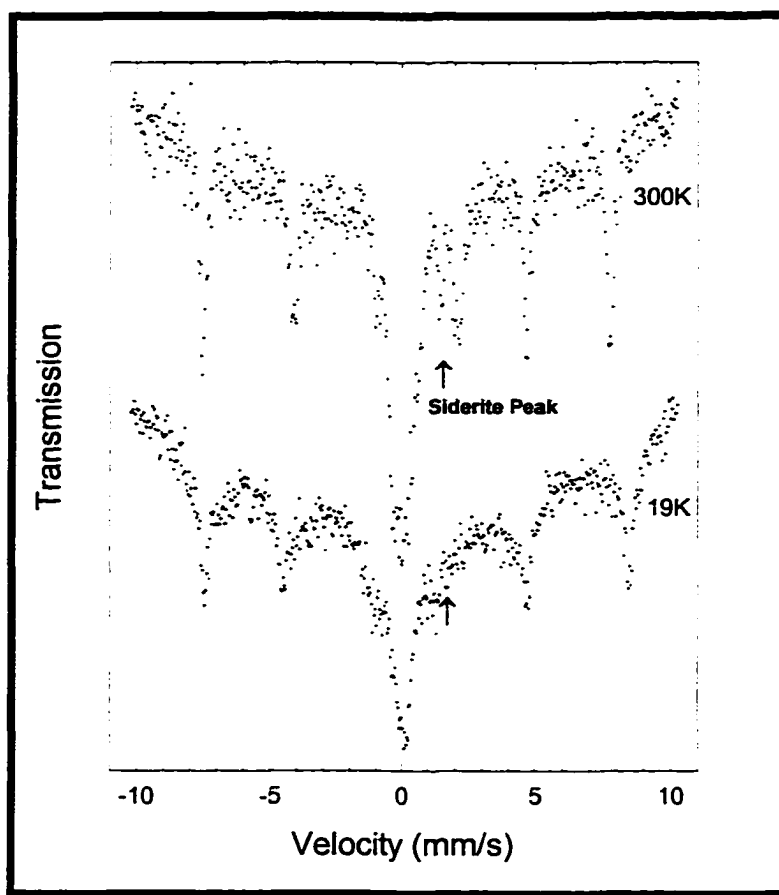


FIGURE 1. Mössbauer spectra of chert-stromatolite showing the characteristic disappearance or movement of the siderite peak at low temperature.

CHAPTER 2

THEORY

In this chapter, theoretical background for the experimental methods used in the analysis of the YNP core samples is presented, with the primary focus placed on Mössbauer spectroscopy. A more detailed description of the Mössbauer effect XRPD with energy dispersive spectroscopy (EDS) can be found in several texts on the subject [*Bancroft, 1973; Whan, 1986; Mitra, 1992*].

A. Mössbauer Spectroscopy

Iron Mössbauer spectroscopy is a non-destructive nuclear resonance spectroscopy technique that employs the 14.4-keV transition between the ground state and the first excited state in the Fe^{57} nucleus. The Mössbauer effect, recoil-free nuclear resonance is a resonance effect by which radiation from a source is resonantly absorbed in the sample. In most simple terms, the effect occurs when an isolated Fe^{57} nucleus decays from the first excited state to the ground state, emitting a gamma (γ) ray of energy 14.4 keV which can then be resonantly absorbed by another Fe^{57} nucleus (Figure 2). However, this illustration is an over-simplification because it does not account for the emitted gamma ray energy lost due to recoil, E_R , of the emitting nucleus. One can calculate this energy lost due to recoil by starting with conservation of linear momentum for the emitting nucleus and emitted gamma ray, p_{nucleus} and $p_{\gamma\text{-ray}}$, as shown.

$$p_{\text{nucleus}} = p_{\gamma\text{-ray}} \quad (1)$$

The magnitude of the γ -ray momentum is given by the equation

$$p_{\gamma\text{-ray}} = E_{\gamma\text{-ray}} / c \quad (2)$$

where $E_{\gamma\text{-ray}}$ is the energy of the γ -ray photon and c is the speed of light. E_R , for the emitting nucleus, can now be written using the non-relativistic approximation as follows:

$$E_R \approx p_{\text{nucleus}}^2 / 2M \Rightarrow E_R \approx E_{\gamma\text{-ray}}^2 / 2Mc^2 \quad (3)$$

where M is the nuclear mass. From this equation, E_R for the 14.4-keV photon emission of Fe^{57} is approximately 1.96×10^{-3} eV.

The parent nucleus that usually provides the Fe^{57} nuclei in the first excited-state is the Co^{57} source, which undergoes nuclear decay according to the diagram shown in Figure 3. The levels in the diagram are shown with their energies and spin quantum numbers, I , all with a parity of -1 . The relative transition probabilities and excited-state half lives for specific energies in the decay process are listed in Table 1. Level energies are listed across the top of Table 1 with transition energies listed along the left side of the table. The natural line width (full-width at half maximum) of the energy distribution) of the 14.4 keV gamma ray, $\Gamma_{\gamma\text{-ray}}$, can be calculated from the half-life of the first excited level, 97.7 ns, using the relationship

$$\Delta E \cdot \Delta t \geq \hbar / 2 \quad (4)$$

where ΔE represents the uncertainty in energy, Δt is the uncertainty in time, and \hbar (6.5855×10^{-16} eV·s) is Planck's constant divided by 2π . Equation (4) can be rewritten in terms of the natural line width (full width at half maximum of a Lorentzian energy distribution [Shelfer, 1992] and the mean lifetime, τ , of the excited state as

$$\Gamma_{\gamma\text{-ray}} \cdot \tau = \hbar \quad (6)$$

where τ is the excited state half-life divided by $\ln 2$ resulting in a recoil energy of 9.7×10^9 eV that is five orders of magnitude greater than the line width. Therefore, it is obvious that the condition required for resonance will not be satisfied.

Table 1. Fe⁵⁷ Excited-State Transition Percentages and Half-Lives

	LEVEL		ENERGIES	
Transition Energies (keV)	706.41 (keV)	366.74 (keV)	136.471 (keV)	14.4125 (keV)
366.74	2.5	---	---	---
136.471	8	8	---	---
14.4125	86	77	89	---
0	3.5	15	11	100
Half-life (ns)	0.003	0.0069	8.5	97.7

In 1961, Rudolph L. Mössbauer discovered the recoil-free emission and absorption of gamma rays in nuclei and was awarded the Nobel Prize in physics for his efforts. This was achieved, essentially, by embedding the emitting nucleus into a crystalline lattice (or other solid host material). Quantum mechanics predicts that an appreciable fraction of γ -rays can and will be emitted without loss of energy to the host environment (i.e., recoil-free fraction). High quality Co⁵⁷ Mössbauer sources typically have recoil-free fractions of about 95%.

The truly amazing power of this technique lies in the fact that the electronic and magnetic environments surrounding the nucleus affect the energy levels of the nucleus in

a manner that can be detected. The simple nuclear level diagram shown in Figure 5, for example, is altered by two hyperfine interactions, which are interactions between the nucleus and electronic environment on the order of $10^{-7}\sim 10^{-8}$ eV regardless of the atom or nucleus involved. The three interactions of importance, which aid in the complete characterization of most samples or minerals, are the isomer shift, IS, the electronic quadrupole splitting, QS, and the magnetic hyperfine splitting, B_{hf} .

1. Isomer "Center" Shift

The isomer shift arises from the electrostatic interaction between the nuclear charge distribution and those electrons that have a finite probability of being found in the region of the nucleus (i.e., the s-state electrons only; see Figure 4). If the nucleus is approximated to be a positive uniformly charged sphere, located at the origin, with radius, R , and the s-electron density at the nucleus, $[\Psi_s(0)]^2$, is slowly varying (i.e., constant) over the dimensions of the nucleus, the interaction energy is given by

$$\Delta E = K [\Psi_s(0)]^2 R^2 \quad (7)$$

where K is a nuclear constant, and $R = \sqrt{\langle r^2 \rangle} = r_{\text{rms}}$ of the nucleus. Thus, the energy shift between the excited and ground states is given by

$$\Delta E_e - \Delta E_g = K [\Psi_s(0)]^2 (R_e^2 - R_g^2) \quad (8)$$

where R_e and R_g are the root mean square radii of the excited and ground states, respectively. Since their are two s-state wavefunctions, $[\Psi_s(0)]^2$, of the source and $[\Psi_s(0)]^2_a$ of the absorber, which may not be equal, the isomer shift is then the difference between source and absorber energies E_s and E_a , expressed by Equation (9) and shown in

Figure 5:

$$\text{I.S.} = E_2 - E_3 = \Delta E_2 - \Delta E_3 = K (R_c^2 - R_g^2) \{ [\Psi_2(0)]^2 - [\Psi_3(0)]^2 \}. \quad (9)$$

2. Electric Quadrupole Splitting

Electric quadrupole splitting occurs as a result of an interaction between the non-spherical charge distribution of the nucleus and the electronic environment of less than cubic symmetry. The total energy of interaction may be written as

$$U = \int \rho_{\text{nucleus}}(\vec{r}) \phi_{\text{elec.}}(\vec{r}) dV \quad (10)$$

where ρ_{nucleus} is the nuclear charge density and $\phi_{\text{elec.}}$ is the electric potential established by the electrons and ions that surround it; the integral is carried out over the dimensions of the nucleus. A multipole expansion of $\phi(r)$ about $r = 0$ is appropriate since the size of the nucleus, at the origin, is much less than that of the atom, and since $\phi(\vec{r})$ varies very slowly over the nuclear dimensions.

With this assumption, the potential can be expanded, giving the equation

$$\phi(\vec{r}) = \phi(0) + \sum_{i=1}^3 x_i \left. \frac{\partial \phi}{\partial x_i} \right|_0 + \frac{1}{2} \sum_{i,j=1}^3 x_i x_j \left. \frac{\partial^2 \phi}{\partial x_i \partial x_j} \right|_0 + \dots \{2^n \text{ poles}\} \quad (11)$$

where the origin is located at the center of the nucleus, the derivatives are evaluated at the origin, and $\vec{r} = (x_1, x_2, x_3)$. The total energy, U , is then composed of a series of terms as shown:

$$U = \sum_{n=0}^{\infty} U_n. \quad (12)$$

The first term in this series, U_0 , represents the monopole term as follows:

$$U_0 = \int \rho_{nucleus}(\bar{r}) \phi_{elec.}(0) dv = \int \rho_{nucleus}(\bar{r}) dv \phi_{elec.}(0) = Ze \phi_{elec.}(0) = const. \quad (13)$$

where Z is the nuclear charge and e is the magnitude of the electronic charge. U_0 contributes the same to all nuclear levels and can be ignored when transitions are considered. The next term in the series, U_1 , is the dipole term. This term will be zero because the nuclear charge density is symmetric about the origin, which makes the product of $x_i \rho(\bar{r})$ an odd function of x_i . The integral of an odd function over the symmetric limits of the nuclear volume is zero:

$$U_{dipole} = U_1 = \sum_{i=1}^3 \left(\int x_i \rho(\bar{r}) dv \right) \frac{\partial \phi}{\partial x_i} \Big|_0 = 0 = U_n \text{ for all } n = \text{odd} \quad (14)$$

because $\rho(r)$ is centrally symmetric. The next term is the quadrupole term, U_2 , is given by the expression

$$U_{quadrupole} = U_2 = \frac{1}{2} \sum_{i,j=1}^3 \left(\int x_i x_j \rho(\bar{r}) dv \right) \frac{\partial^2 \phi}{\partial x_i \partial x_j} \Big|_0 \neq 0 \quad (15)$$

which is the only remaining term that contributes to the total energy, because either the others integrate to zero (i.e., odd function over symmetric limits) or the contribution will be negligible because of higher order derivatives of slowly varying functions. Therefore, the quadrupole term is the only contribution of importance. We now define the tensor,

$$\phi_{ij} = \frac{\partial^2 \phi}{\partial x_i \partial x_j} \Big|_0$$

for simplification. This gives rise to a 3 x 3-tensor matrix whose trace, T , is given by equation (16) below:

$$T = \frac{\partial^2 \phi}{\partial x_1^2} \Big|_0 + \frac{\partial^2 \phi}{\partial x_2^2} \Big|_0 + \frac{\partial^2 \phi}{\partial x_3^2} \Big|_0 = \nabla^2 \phi \Big|_0 \quad (16)$$

By applying Poisson's equation, the equation for T becomes

$$T = \nabla^2 \phi|_0 = -4\pi\rho_{elec}(0) = 4\pi e |\Psi_{elec}(0)|^2 \quad (17)$$

where $\rho_{elec}(0)$ is the electron charge density within the nuclear volume, $|\Psi_{elec}(0)|^2$ is the total electronic probability density at the nucleus, and $-e$ is the charge of an electron. We can now define a new tensor V_{ij} that has a trace of zero as shown

$$V_{ij} = \phi_{ij} - 1/3 T \delta_{ij} \quad (18)$$

where $\delta_{ij} = 0$ if $i \neq j$, and $\delta = 1$ if $i = j$. This results in the electric quadrupole interaction energy, Q_{ij} , which is directional in nature and serves to split nuclear energy levels with spins $I \geq 1$. The explicit form of Q_{ij} is given by the equation

$$Q_{ij} = \frac{1}{6} \sum_{l,j=1}^3 \left[\int (3x_i x_j - r^2 \delta_{ij}) \rho(\vec{r}) dv \right] Y_{ij} \quad (19)$$

where Q_{ij} has been written in conventional notation using the fact that $\sum V_{ii} = 0$.

A new "principal axis" coordinate system (x,y,z) may now be chosen in such a way to preserve physical consequences while simplifying the mathematics. Thus, the diagonalized matrix shown below now gives the same convenient V_{ij} tensor in a different axis system.

$$[V_{ij}] = \begin{bmatrix} V_{xx} & 0 & 0 \\ 0 & V_{yy} & 0 \\ 0 & 0 & V_{zz} \end{bmatrix} \quad (20)$$

By convention, the axes are chosen such that $|V_{xx}| \leq |V_{yy}| \leq |V_{zz}|$. The trace is invariant under rotation and we still have $V_{xx} + V_{yy} + V_{zz} = 0$, implying that the tensor is determined by only two independent parameters, which may be defined by

$$eq = V_{zz} = - \frac{\partial}{\partial z} E_z \text{ and } \eta = \frac{V_{xx} - V_{yy}}{V_{zz}} \quad (21)$$

where eq is the negative axial component of the electric field gradient and η is the asymmetry parameter. The electric quadrupole interaction (19) can now be written as

$$Q_{ij} = \frac{eq}{4} \left[\int (3z^2 - r^2) \rho(\vec{r}) dv + \eta \int (x^2 - y^2) \rho(\vec{r}) dv \right] \quad (22)$$

The Wigner-Eckart theorem can now be used to simplify Q_{ij} and make further computations much clearer. This theorem states that since \vec{r} transforms like the angular momentum vector, \vec{I} , under certain rotations, the matrix elements of Q_{ij} formed between two states are proportional to matrix elements formed by replacing the coordinates x , y , and z with the angular momentum operators I_x , I_y , and I_z , respectively. Mathematical representation of the theorem is illustrated as follows:

$$\int f(x, y, z) \rho(\vec{r}) dv = \text{const} \times \langle f(\hat{I}_x, \hat{I}_y, \hat{I}_z) \rangle \quad (25)$$

where $\rho(\vec{r})$ is evaluated in the particular quantum mechanical state, $|R(r)\rangle |I, m_1\rangle$, and the proportionality constant is independent of m_1 . To evaluate the constant, we begin by defining the nuclear electric quadrupole moment, Q [Preston, 1962],

$$eQ = \int (3z^2 - r^2) \rho(\vec{r}) dv \quad (24)$$

where $\rho(r)$ is evaluated in the state $m_1 = I$. Thus,

$$eQ = C \langle I, I | 3\hat{I}_z^2 - \vec{I}^2 | I, I \rangle = C [3I^2 - I(I+1)] = C(2I^2 - 1) \quad (25)$$

where C is a proportionality constant which may be written as follows

$$C = \frac{eQ}{I(2I-1)}. \quad (26)$$

The second term in the brackets of equation (22) is zero because we have an odd function integrated over the symmetric limits of the state $|I, I\rangle$ as shown

$$\int (x^2 - y^2) \rho dv \propto \langle I_x^2 - I_y^2 \rangle = 0. \quad (27)$$

The Hamiltonian operator for the electric quadrupole interaction can now be written with raising and lowering operators, I_+ and I_- , instead of I_x and I_y related by the equation

$$\hat{I}_x^2 - \hat{I}_y^2 = \frac{1}{2}(\hat{I}_+^2 + \hat{I}_-^2). \quad (28)$$

Now, the full Hamiltonian, H_Q , is expressed as follows

$$\hat{H}_Q = \frac{e^2 q Q}{4I(2I-1)} [3\hat{I}_z^2 - I(I+1) + \eta(\hat{I}_+^2 + \hat{I}_-^2)]. \quad (29)$$

As stated earlier, the electric quadrupole interaction removes some of the degeneracy of nuclear levels with $I \geq 1$. In the case of ^{57}Fe , the presence of an electric field gradient at the nucleus results in the splitting of the excited state $I = 3/2$ into two levels and leaves the ground state unchanged since $I = 1/2$. The energy of interaction, which is the solution to Schrödinger's equation of the electric quadrupole interaction Hamiltonian, equation (29), is given by the expression

$$E_Q = \langle \hat{H}_Q \rangle = \pm \frac{e^2 q Q}{4} \sqrt{1 + \frac{\eta^2}{3}} \quad (30)$$

where $e^2 q Q$ is defined as the electric quadrupole coupling constant, and $e^2 q Q/2$ is the electric quadrupole splitting (QS) term typically used in the literature. The quadrupole splitting is the separation between the two $I = 3/2$ sublevels. Figure 6 shows a simple illustration representative of the interaction between the non-spherical nuclear charge distribution and an electronic environment of less than cubic symmetry. As a

consequence of this interaction, there are two possible transitions between the ground state and first excited state. Thus, there are two energies at which resonant absorption can occur.

Figure 7 shows an energy-level diagram of the combined isomer shift and electric quadrupole splitting along with the Mössbauer spectrum of sodium nitroprusside ($\text{Na}_2[\text{Fe}(\text{CN})_5\text{NO}] \cdot 2\text{H}_2\text{O}$) that is typical of such transitions. The effect of the isomer shift will be to shift the centroid of the spectrum from zero velocity, towards negative velocities for this example. There are also two resonant absorption lines, corresponding to allowed transitions caused by the electric quadrupole interaction. This type of splitting in a spectrum is termed a “doublet.” The amount of the isomer shift, δ , and size of the quadrupole splitting, QS, are characteristic of a given sample and, thus, can be used for identification. This discussion ignores any magnetic interactions.

3. Magnetic Hyperfine (Zeeman) Splitting

Nuclei with spin, $I \neq 0$, give rise to a nuclear magnetic moment, $\vec{\mu}_N$, given by the equation

$$\mu_N = g_N \beta_N I \quad (31)$$

where g_N is the nuclear Lande' g-factor or gyromagnetic ratio and β_N is the nuclear Bohr magneton given by equation (32) where e and m_p are the charge and mass of the proton.

$$\beta_N = \frac{e\hbar}{2m_p} = 5.051 \times 10^{-27} \frac{\text{Joules}}{\text{Tesla}} \quad (32)$$

The interaction between the nuclear spin, \vec{I} , and a steady magnetic field, $\vec{B} = B_N \hat{e}_z$,

produced by the electronic environment and/or an externally applied field serves to split the nuclear levels or “lift the degeneracy” into $2I+1$ levels as expressed by the Hamiltonian operator

$$\hat{H}_M = -\vec{\mu} \cdot \vec{B} = -g\mu_N B_{hf} \hat{I}_z \quad (33)$$

where B_{hf} is the effective magnetic field seen at the nucleus. One can find the energies of these $2I+1$ levels by solving Schrödinger’s equation using the Hamiltonian in equation (33) giving the following:

$$E_M = \langle I, m_I | \hat{H}_M | I, m_I \rangle = -g\mu_N B m_I \quad (34)$$

where m_I is the magnetic quantum number.

The splitting of the nuclear energy levels of ^{57}Fe due to the magnetic dipole interaction is shown in Figure 8 along with the Mössbauer spectrum of a natural iron foil sample. The Zeeman splitting has removed the degeneracy for both nuclear energy levels. As can be seen, there are only six possible nuclear transitions allowed, governed by the selection rule ($\Delta m_I = 0, \pm 1$ for an m_I transition). The corresponding resonant absorption energies (lines) produce what is termed a “sextet.” The quadrupole shift in a magnetic sextet (also QS), as opposed to that of a doublet, is measured by evaluating the difference between the 1-2 and the 5-6 energy level transitions given by the expression

$$\text{QS} = (\Delta E_{5,6} - \Delta E_{1,2}) / 2. \quad (35)$$

The effective magnetic field, B_{hf} , experienced by the nucleus can be found by measuring the separation between the outer absorption lines of a sextet. Both these values are characteristic of a given sample and can be used to identify a material. For ^{57}Fe , there is

an inversion of levels in the excited state which is due to the negative g-factor of the excited state ($g_{\text{ground}} = 0.0907$, $g_{\text{excited}} = -0.0518$) [Stevens, 1978 in Shelfer, 1992].

The transition intensities (or probabilities) for each of the six possible resonant energies are proportional to the squares of the Clebsch-Gordan coefficients, which couple any two quantum states, and also depend on the angle, Θ , between the direction of the γ -rays and the magnetic field. Table 2 lists the relative intensities for the six transitions for the cases of randomly oriented powders, $\Theta = 0^\circ$, and $\Theta = 90^\circ$.

Table 2. Relative Transition Probabilities for Specific Photon Directions Relative to B_{hf} .

Transition	M_I -Ground State	M_I -Excited State	Random	$\Theta = 0$	$\Theta = 90^\circ$
1	-1/2	-3/2	3	3	3
2	-1/2	-1/2	2	0	4
3	-1/2	+1/2	1	1	1
4	+1/2	-1/2	1	1	1
5	+1/2	+1/2	2	0	4
6	+1/2	+3/2	3	3	3

In Table 3, a summary of the nuclear properties and the nuclear-electronic interactions, which give rise to the Mössbauer spectral features, is shown. These interactions fall into three distinct categories. Main atomic structure results from interactions between electronic and nuclear properties that give rise to the principle quantum numbers (n, l, m_l, m_s) with energies on the order of ~ 1 eV. Fine structure results from electron-electron (intra-atomic) interactions (e.g., spin-orbital effects) with energies on the order of $\sim 10^{-4}$ eV. Lastly, hyperfine structure arises from interactions between

nuclear-electronic properties with energies on the order of $\sim 10^{-7} - 10^{-8}$, which is the same as the Mössbauer effect, thus the name hyperfine interactions.

The number and position of absorption peaks (sextets and doublets) can be numerous and varied with different minerals, giving a superposition of these sextets and doublets depending on the crystallographic environments. Each iron-containing mineral is unique in this respect and will, accordingly, give a unique Mössbauer signature (spectrum) that can be used for “fingerprinting” and mineral identification. However, it is the detail of the information about the electronic and magnetic environment of each individual iron nuclei that makes Mössbauer spectroscopy such a powerful technique and mineralogical tool.

Table 3. Summary of Nuclear-Electronic Properties and Interactions

Mössbauer Spectral Feature	Nuclear Properties	Electronic Properties
Isomer Shift	finite nuclear size charge distribution	s-orbital electron density (wave function)
Electric Quadrupole Splitting	non-spherical charge distribution Quadrupole moment, Q	Electric Field Gradient (EFG)
Magnetic Hyperfine Splitting	nuclear spin, I g-factor magnetic moment (μ)	magnetic field created by the electronic environment

B. X-Ray Powder Diffraction (XRPD)

XRPD is a technique used to characterize samples in the form of loose powders or aggregates of finely divided material. The powder method is most often used as a phase characterization because of its ability to routinely differentiate between phases having the

same chemical composition but different crystal structures (polymorphs). For example, although chemical analysis can indicate that the empirical formula for a given sample is FeTiO_3 , it cannot determine whether the sample is a mixture of two phases (FeO and one of the three polymorphic forms of TiO_2) or whether the sample is the single-phase mineral FeTiO_3 or ilmenite. The ability of XRPD to perform these identifications simply and conveniently as a primary technique or as a supplementary one is why it is such an important technique. Characterization of a substance consists of placing a powder sample in a collimated monochromatic beam of x-ray radiation. The radiation, of specific wavelength, λ , enters the sample at specific angles and is diffracted by lattice planes of randomly oriented crystallites in the powder. The scattered radiation will experience either constructive or destructive interference.

For there to be constructive interference, the total path traveled by the scattered radiation within the sample must be equal to an integral number of wavelengths. Only radiation undergoing constructive interference will be detected. This constructive interference condition is given by the relationship known as Bragg's (equation) Law,

$$n \lambda = 2 d \sin \Theta \quad (36)$$

where n is an integer, λ is the wavelength of the x-ray radiation, d is the spacing between lattice planes of atoms in a crystalline phase, and Θ is the angular position of the diffracted beam in relation to the scattering planes. A resulting diffraction pattern is then produced, typically displayed as a graph of intensity as a function of interplanar distance, d , or diffraction angle, 2Θ , which is unique for most crystalline phases. Much as a fingerprint is unique for each person, the diffraction pattern can act as an empirical

fingerprint for that phase, and qualitative identification of these phases can be accomplished by using a manual or electronic database published and maintained by the Joint Committee on Powder Diffraction Standards.

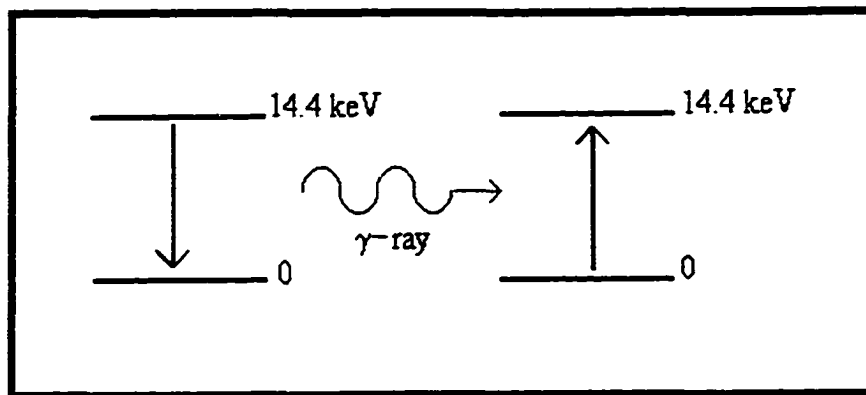


Figure 2. Illustration showing the nuclear resonance effect for Fe^{57} .

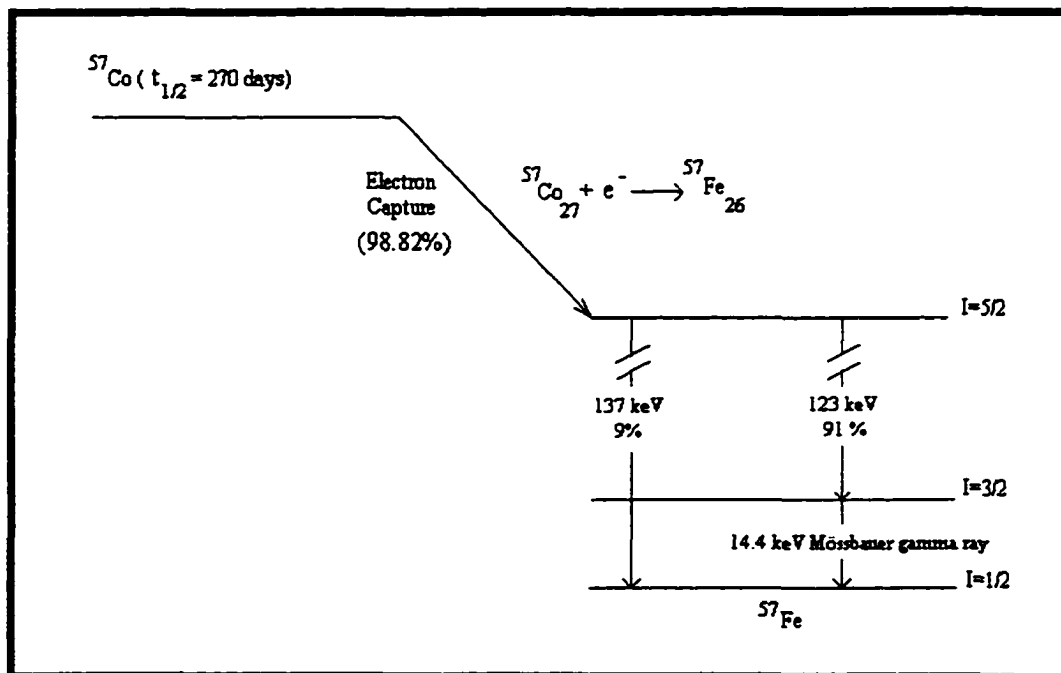


Figure 3. Co^{57} nuclear decay diagram (706,366 levels omitted for clarity).

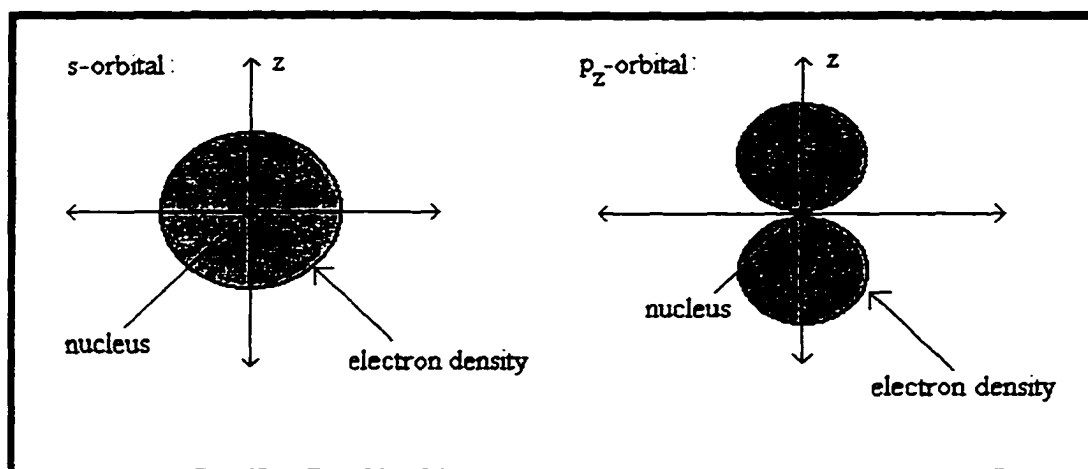


Figure 4. Illustration of the nuclear charge distribution and the electron densities for the s and p-states.

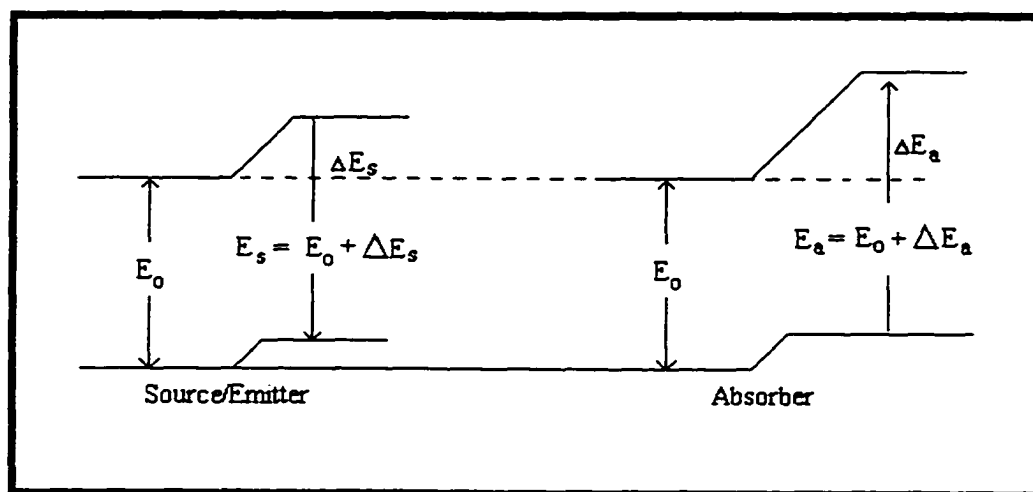


Figure 5. Energy level diagram showing effect of the isomer shift.

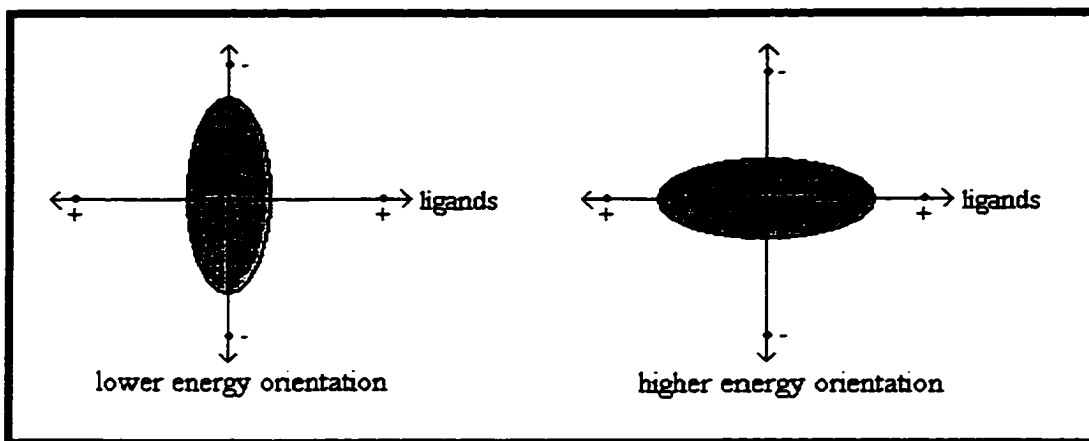


Figure 6. Illustration showing exaggerated nuclear shape with the two possible orientations that the nucleus may have for the nuclear spin state, $I = 3/2$ ($\Rightarrow m_I = \pm 3/2$ (right), $\pm 1/2$ (left)); e.g. ^{57}Fe , first excited state).

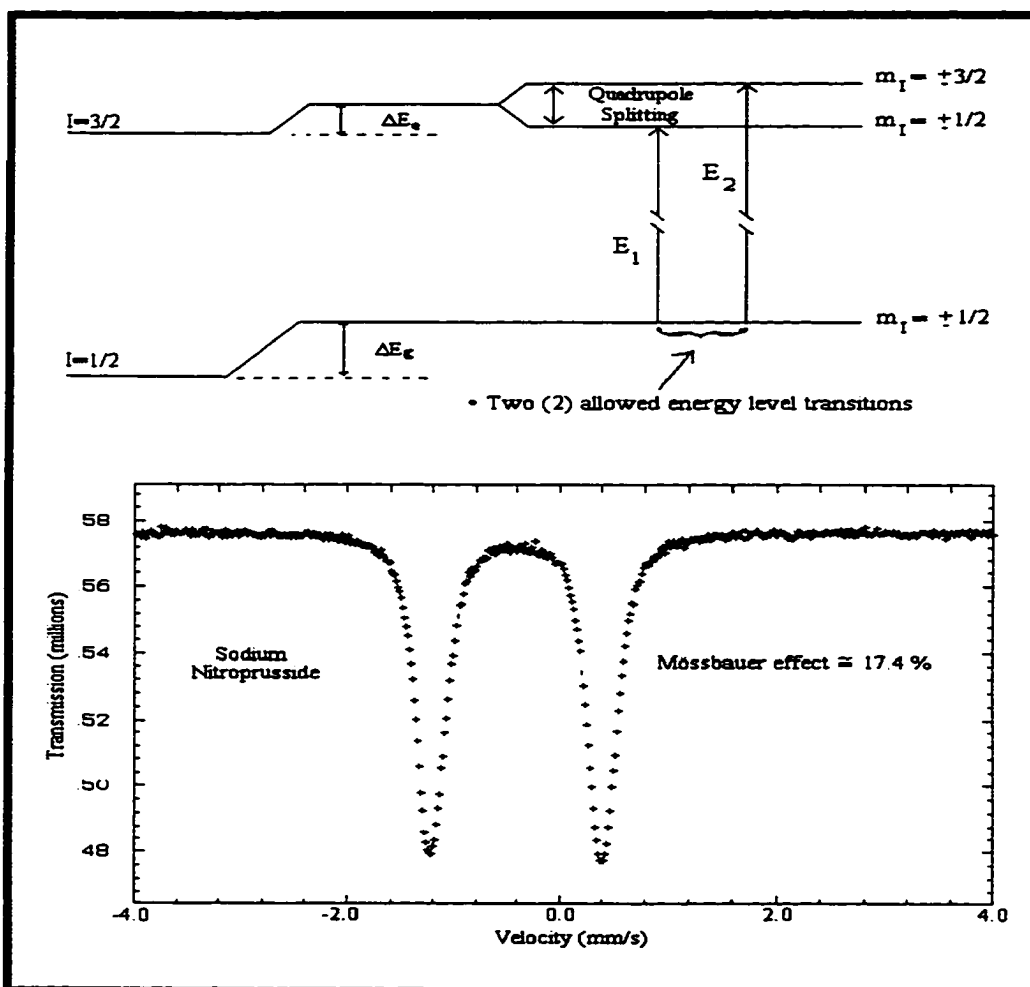


Figure 7. Energy level diagram showing the effect of the electric quadrupole.

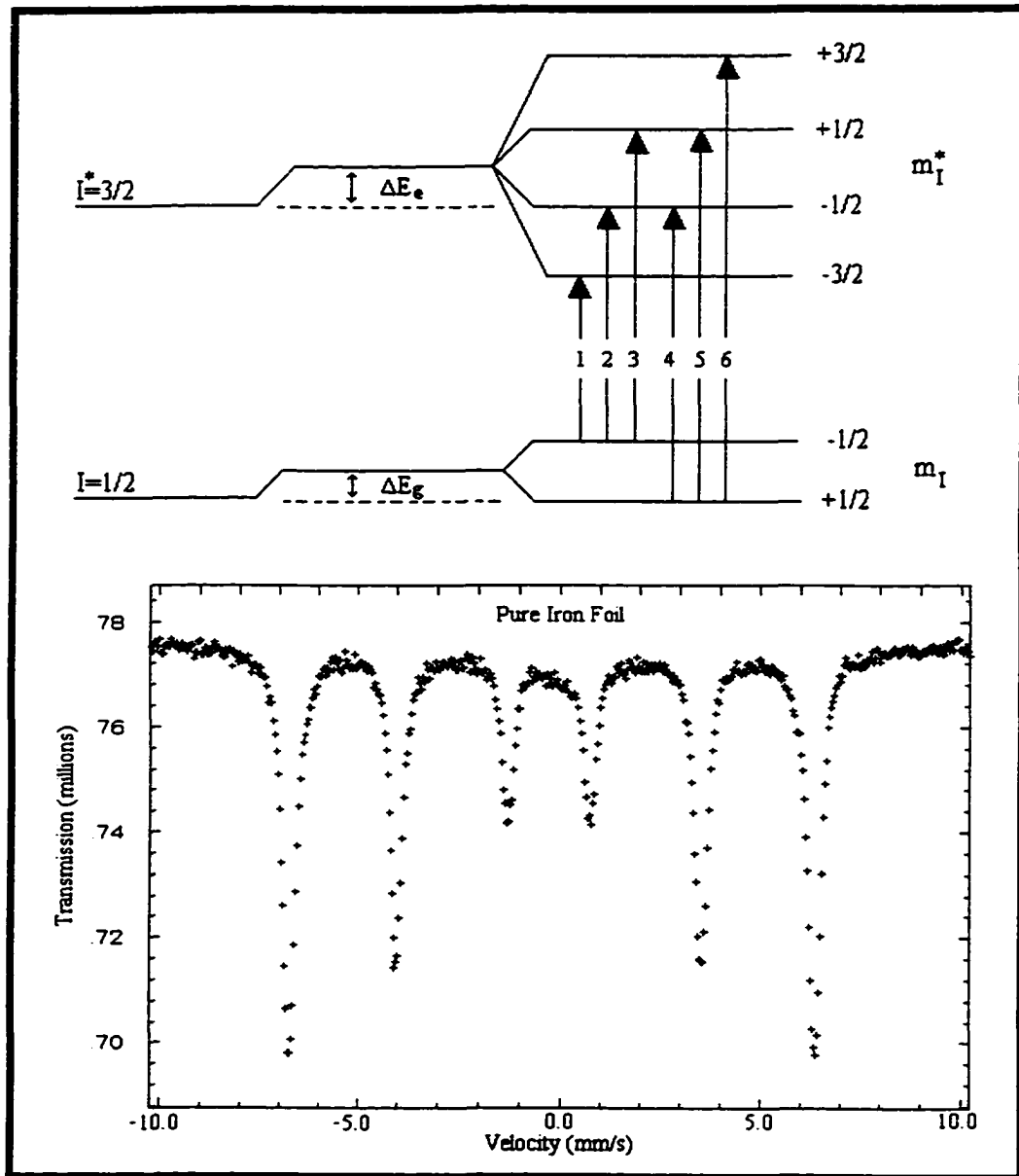


Figure 8. Energy level diagram showing the effect of the magnetic hyperfine splitting and isomer shift with a corresponding Mössbauer spectrum showing the magnetic sextet.

CHAPTER 3

EXPERIMENTAL METHODS

A. Samples and Preparation

Samples in this work were obtained from several hydrothermal settings (collected by Dr. Jack Farmer, NASA Ames Research Center). Initial discussion pertains to two samples collected from an iron-rich outflow stream at Manitou Springs, CO, and along the margins of Obsidian Pool in Yellowstone National Park, WY, where several small iron-oxide-depositing thermal springs exist. We also collected a suite of 13 samples at four locations (Table 4) along the main outflow channel of a large, iron-rich thermal spring mound in the Chocolate Pots area of Yellowstone National Park, which lies adjacent to the Gibbon River (Figure 9).

Properties of the water (T, pH-hydrogen ion concentration, Eh-redox potential) in the channel above each collection site were also measured (Table 4 and Figure 10). Each site was cored to a depth of at least 1 cm, except at the vent, where materials were too friable. Cores were then subdivided into depth intervals (see Table 4) using a razor blade. Immediately following field collection, samples were preserved for transport at about -5°C to inhibit further chemical change and then stored at about -25°C in the laboratory. Upon drying, samples collected near the stream (2C1-2C4, 3C1-3C4) all formed a fine powder; whereas material collected closer to the vent (5C1-4, 6C1) formed a glassy, laminated material. A microscope (20X) shows this material to consist of thin ($\sim 50\ \mu\text{m}$) alternating light and dark (reddish) bands which fractured readily on handling, and it was easily pulverized with a mortar and pestle. For Mössbauer analysis, the

powdered samples were dispersed in molten paraffin ($\sim 55^{\circ}\text{C}$), then quickly pressed into 1.6-cm diameter pellets as shown in Table 5.

FESEM and EDX spectroscopy [Wade *et al.*, 1998] were employed for elemental analysis. Duplicate cores were collected at each sample site and fixed in the field using a mixture of 2% glutaraldehyde and 4% formalin in filtered spring water. Upon returning to the laboratory, the upper few millimeters were subsampled from cores, fixatives were removed, and samples were dehydrated by passing them through a graded ethanol series (10-25-50-75-95-100-100%). Samples were stored in 100% ethanol and later critical point dried using a Pelco model CPD-2 critical point dryer.

Table 4. Chocolate Pots Mössbauer Samples

	Distance from vent (m)			
Depth (mm)	7	6	2	0
Depth (mm)	7	6	2	0
0-1	2C1	3C1	5C1	-
0-1	2C1	3C1	5C1	-
1-4	2C2	3C2	5C2	-
1-4	2C2	3C2	5C2	-
4-8	2C3	3C3	5C3	-
4-8	2C3	3C3	5C3	-
>8	2C4	3C4	5C4	-
>8	2C4	3C4	5C4	-
0-10	-	-	-	6C1
0-10	-	-	-	6C1
T (C)	48.0	53.2	54.2	55.0
T (C)	48.0	53.2	54.2	55.0
pH	7.9	7.8	7.2	5.8
Eh (mV)	-49.0	-45.7	-2.0	81.7

13 samples from the main outflow channel at East Chocolate Pots (YNP), collected at four location along the channel, measured from the vent, and cored to four depths, as indicated. Included also are temperature (T), pH, and redox potential (Eh) of the water immediately above the collection site.

Table 5. Quantities Used for the Production of Mössbauer Absorbers

Core Sample	Wax Used, mg	Sample Used, mg	Yield %	Absorber mg of sample/cm ²
2C1	141.8	40.2	97.5	19.5
2C2	142.5	40.3	94.4	18.9
2C3	155.5	44.0	97.3	21.3
2C4	156.1	40.6	96.7	19.5
3C1	142.6	43.4	98.1	21.2
3C2	131.3	40.6	98.1	19.8
3C3	183.2	45.9	97.3	22.2
3C4	121.5	44.4	97.7	21.6
5C1	167.7	43.0	97.3	20.8
5C2	135.1	44.6	98.0	21.7
5C3	145.0	48.2	93.7	22.5
5C4	160.7	46.2	95.3	21.9
6C1	143.0	45.3	97.7	22.0

The percentage yield refers to the amount of sample surviving the production process.

B. Mössbauer Spectroscopy

Mössbauer experiments were carried out with gamma rays being produced via radioactive decay of a ⁵⁷Co source in rhodium matrix to the ground state of ⁵⁷Fe, as shown previously in Figure 3 from Chapter 2. The activity of the cobalt source (270-day half-life) ranged from 50 to ~20 mCi, depending on the age of the source. The Mössbauer gamma ray energy is modulated via the Döppler effect, causing shift in the γ -ray energy given by the equation

$$\Delta E = (\nu / c) E_{\gamma} \quad (37)$$

where E_{γ} is the gamma ray energy, c is the speed of light, and ν is the velocity of the source relative to the absorber. This source modulation is achieved by using a standard Mössbauer drive (Ranger Scientific VT-700). By doing this, we can scan a range of energies looking for nuclear resonant absorption of γ -rays.

For iron Mössbauer spectroscopy and the interactions discussed in Chapter 2, velocities up to 10 mm/s ($|\Delta E| < 4.8 \times 10^{-7}$ eV) are generally required to scan the full range of possible resonant energies in a typical sample. After the γ -rays are shifted and

emitted from the source along with the other photons, they pass through a collimator, forming a defined photon beam that interacts with the sample (Figure 11).

In transmission geometry (Figure 11), when the shifted γ -ray has the precise energy to satisfy the resonant condition of a ^{57}Fe nucleus in a sample, the γ -ray may be resonantly absorbed. The detector, placed opposite the Mössbauer drive relative to the sample, detects γ -rays as voltage pulses, whose signals are then amplified. The pulse height analyzer function of the multichannel analyzer sorts the pulses according to voltage. The single channel analyzer then sets a window, “the gated signal,” referenced by the pulse height analyzer, allows only those pulses of energy ± 14.4 keV to be detected. The multichannel scaler then opens channels for all these pulses and then recycles spending an equal amount of time in each channel [Wade, 1991]. For this associated time period, a square wave is produced for one complete cycle of motion calibrated to 1024 channels. This square wave is then integrated, producing a linear triangle wave that is used as the reference velocity signal. The reference signal, along with negative feedback that minimizes any distortion in the triangle wave, is responsible for the motion of the drive, which is automatically correlated with the multichannel scaler. The resulting Mössbauer spectrum, which is a graph of radiation intensity as a function of the Doppler velocity (shifted γ -ray energy), will show an absorption “dip” or line in the background at the resonant energy transitions for the sample being probed. Examples of spectra are shown in Figures 7 and 8. For temperature studies (300 K to 12 K), an APD “Displex” closed-cycle refrigerator is coupled by gaseous helium to the vibration-insulated Mössbauer shroud. A Lakeshore 330 temperature controller was used to control the sample chamber temperature. To minimize mechanical vibrations that

could affect the modulation of the source, a special harness had to be designed and constructed, which is shown in Figure 12.

C. Powder X-Ray Diffraction

Diffraction experiments were performed on a Siemens D500 Diffractometer using Cu K_{α} radiation of wavelength, λ , 1.5401 Å. Scans were carried out over the range of 2 degrees (2θ) to 90 degrees (2θ) with a scan rate of 0.02 degrees per second. Dry powdered samples were placed in a sample holder and locked into position on the goniometer, which rotates along with the detector (Figure 13). The sample is then exposed to a divergent beam of Cu K_{α} radiation produced by an x-ray generator. As the goniometer sweeps through a specified angle, θ , the radiation is scattered by the lattice planes of the randomly ordered particulate in the powdered sample. This divergent scattered beam enters a slit of predefined width, which acts as a collimator, and is then detected by a detector that sweeps through an angle 2θ , producing a graph of radiation intensity (number of counts) versus angle in degrees, 2θ .

D. Calibration

Spectral data were analyzed and parameter values obtained by least-squares fitting with a sum of Lorentzian line shapes model based on the standard hyperfine interactions appropriate for Mössbauer spectroscopy [Agesti *et al.*, 1969; Bent *et al.*, 1969]. To make sure that the reference velocity signal was linear, calibrations were performed at regular intervals using a combination absorber of iron oxide (Fe_2O_3) and natural iron foil 6 microns thick. By doing this, peak velocities throughout the entire energy range can be obtained, allowing for the correction of non-linearities in the spectrum. Calibration

results with standard velocity peak-positions and standard deviations are given in Table 6. A velocity model given by a fifth-order polynomial was used to correct for nonlinearities, giving errors in reported parameter values of less than 0.02 mm/s on average.

Table 6. Calibration Results for Peak Positions (mm/s) of Combined Hematite and Natural Iron Foil (Experimental and Standards) with Deviations

Fe-foil (Std.), mm/s	Hematite (Std.), mm/s	Std. Positions, mm/s	Exp. Positions, mm/s	Deviations, mm/s
5.1983	8.4640	8.4640	8.4711	-0.0071
2.9620	5.1580	5.1983	5.2409	0.0426
0.7257	1.6580	5.1580	5.1609	0.0029
-0.9537	-0.9720	2.9620	2.9676	0.0056
-3.1900	-4.4700	1.6580	1.6658	0.0078
-5.3123	-8.3160	0.7257	0.6953	-0.0304
		-0.9537	-0.9288	0.0249
		-0.9720	-0.9733	-0.0013
		-3.1900	-3.2033	-0.0133
		-4.4700	-4.4706	-0.0060
		-5.4263	-5.4313	-0.0050
		-8.1680	-8.2051	-0.0371



Figure 9. Picture of vent mound collection site in Chocolate Pots region of Yellowstone.

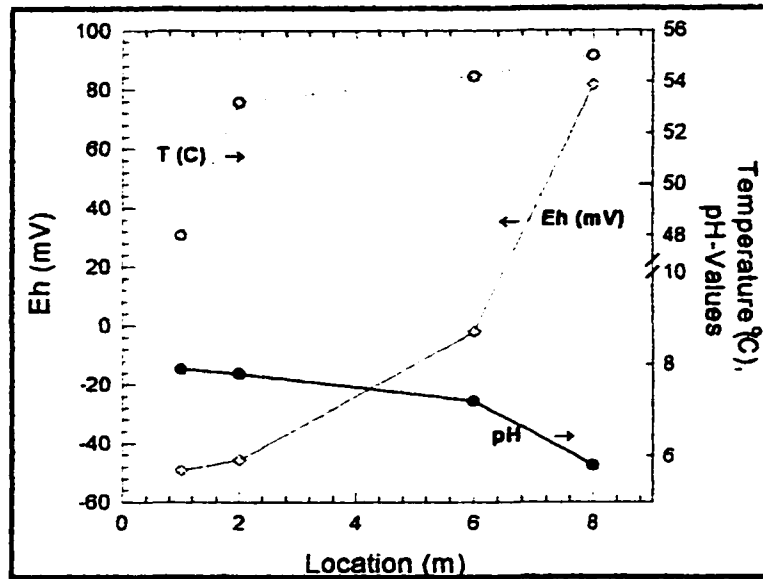


Figure 10. Plot showing variations in temperature, pH, and Eh versus distance from vent.

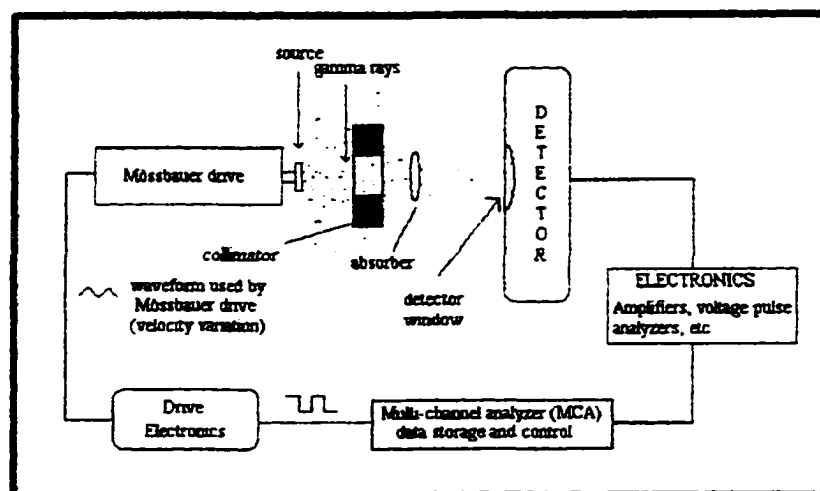


Figure 11. Schematic diagram of Mössbauer spectroscopy experiment

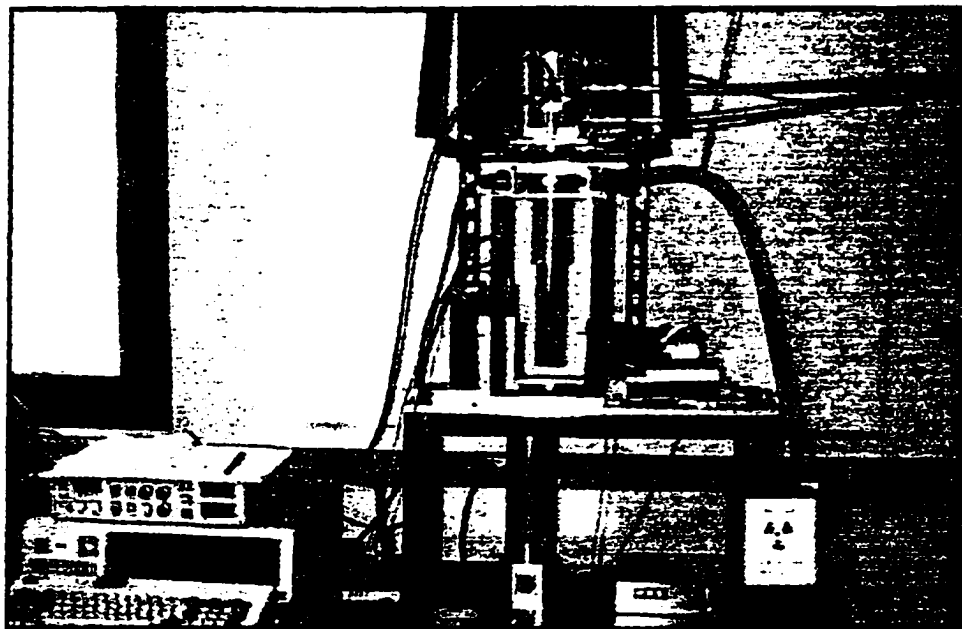


Figure 12. Picture of harness housing the Mössbauer experiment, designed to isolate the sample chamber from the drive and detector and to minimize possible vibration.

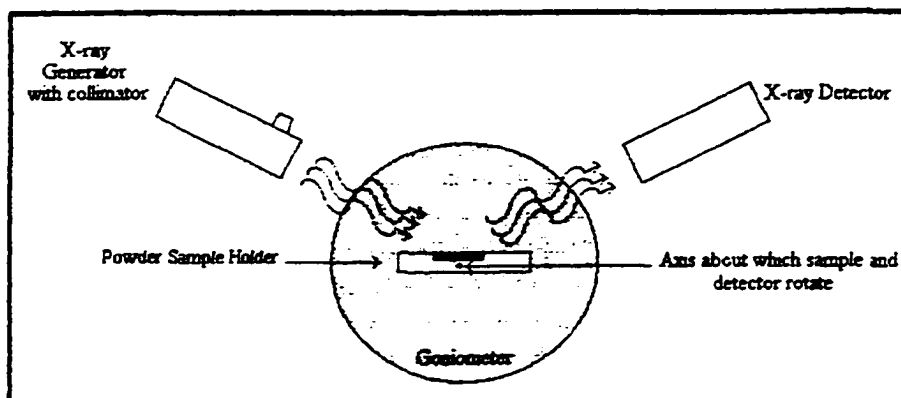


Figure 13. Illustration of the powder x-ray diffraction experiment.

CHAPTER 4

MÖSSBAUER SPECTRAL ANALYSIS

Mössbauer spectral data were analyzed using a least-squares fitting technique employing sum-of-Lorentzian models. For each distinct atomic site (nuclear environment), the adjustable parameters were isomer shift, IS (relative to α -iron metal); electric quadrupole (hyperfine) splitting, QS; effective magnetic hyperfine field at the nucleus, B_{hf} ; Lorentzian linewidth, W (full width at half maximum); and relative spectral area, Area. Each spectrum is modeled as a superposition of individual doublet ($B_{\text{hf}} = 0$) or sextet components ($B_{\text{hf}} \neq 0$) where deviations in fitted parameter values are less than 0.02 mm/s for IS and QS, 0.01 for W , and 0.1 T for B_{hf} . Superposition spectra come about either because of non-equivalent atomic environments within a single mineral phase or because of the presence of several iron-bearing phases. For a doublet component, the two peaks are assigned equal areas, whereas sextet components are modeled with peak areas in the ratio 3:2:1:1:2:3, appropriate for powdered (non-oriented) samples.

A range of measurement temperatures was employed, not only to investigate analogue materials at Mars ambient temperatures, but also to enhance information yield. Parameters generally vary with temperature in a characteristic way, and there may also be a phase change (e.g., magnetic ordering) as temperature is lowered. The first is typically a subtle effect, whereas the latter can dramatically alter the appearance of the spectrum. Several examples of spectra whose components overlap at certain temperatures but are

well separated at others appear later. The typical standard deviations listed above refer to spectra with reduced overlap, which results in smaller correlation among parameter values, especially W and Area, and a reduction in ambiguity of assignments, with a corresponding increase in the reliability of the inferred mineralogy.

Spectral analysis can indicate the valence of iron or the degree of magnetic order (a sextet) in a mineral phase. A doublet component arises when magnetic order is absent (paramagnetic state, $B_{\text{hf}} = 0$) or when a material is magnetically ordered (below its Néel or Curie temperature), but above its blocking temperature (i.e. superparamagnetic state, doublet-sextet spectrum for one mineral phase). When the peak separation (QS) is small, ferric (Fe^{3+}) iron is usually inferred, whereas a more widely spaced doublet suggests ferrous (Fe^{2+}) iron (Figure 7). In a magnetically split spectrum ($B_{\text{hf}} \neq 0$), the effect of the quadrupole interaction is to shift the inner quartet (2:1:1:2) to the left (if $QS > 0$) by $\frac{1}{2} QS$ and the outer doublet (3:3) to the right by the same amount. In extreme cases (large QS), these shifts may be sufficient to reorder the peaks (Appendix A) to an order of 2:3:1:1:2:3, discussed in Chapter 5. The precise values of the principal spectral parameters, IS , QS , and B_{hf} thus serve as a fingerprint in identifying the particular mineral phase or compound.

For well-crystallized material, the typical measured peak width, W , is approximately 0.3 mm/s. However, there are occasions when spectral lines are broadened, indicating either an amorphous nature of the material or a collection of similar crystallites with variable bulk properties, such as particle size, characteristic of the nanophase material, discussed in Chapter 5. Broadened doublet spectra are modeled as a superposition of two sites, with variable quadrupole splitting, QS , and width, W , along

with a common isomer shift, IS. Broadened sextet spectra are generally also skewed (Lorentzian line asymmetry) in a way that preserves the mirror symmetry of peak pairs (1,6; 2,5; 3,4). Peak broadening results from a distribution of hyperfine magnetic fields and therefore can be shown to increase linearly from the center outward, so that a single broadening parameter, Δ , accounts for this ($W_1 = W$; $W_2 = W + \frac{1}{2}\Delta$; $W_3 = W + \Delta$, etc.). Similarly, asymmetry in the field distribution, which is characteristic of nanophase particles, leads to asymmetry in the shape of individual sextet peaks. This skewing effect can be adequately modeled with a single skew parameter, κ , by joining two half Lorentzians at their midline (outer half width = $\frac{1}{2}W_i/\kappa$; inner half width = $\frac{1}{2}W_i \times \kappa$; where $\kappa > 1$ and $i = 1$ to 6) [Morris *et al.*, 1989b]. Although these two added parameters improve the fit, and thus add to the reliability of the model, their precise values do not affect or bias the interpretation of results presented and reported in this work.

In the particular case of material exhibiting superparamagnetic behavior [Kündig *et al.*, 1966], the spectrum typically consists of a doublet-plus-sextet component, whereby the doublet intensity decreases as temperature is lowered while the sextet area correspondingly increases. Even though the material is below its magnetic ordering temperature (where neighboring atomic moments are correlated), for sufficiently small (~10-100 nanometers, hence, "nanophase") particles, thermal effects may overwhelm the tendency of the moments to orient in a particular crystalline direction, the "easy axis." This tendency to orient and, most importantly, to result in a non-zero value of B_{hf} , is proportional to particle volume [Kündig *et al.*, 1966]. Thus, a pure sextet pattern is achieved for small particles only below the so-called blocking temperature, at which the doublet-to-sextet conversion takes place. The range of temperatures over which doublet

and sextet coexist indicates a distribution of particle sizes, the smaller particles (at a given temperature) being associated with the doublet, the larger particles with the sextet. This spectral feature is characteristic of nanophase materials exhibiting superparamagnetic behavior (Appendix A.2).

CHAPTER 5

RESULTS AND DISCUSSION

A. Manitou Springs and Obsidian Pool

Although not the primary focus of this work, additional samples were collected at these sites and analyzed, and their Mössbauer signatures are characteristic of superparamagnetic (nanophase) material. Figure 14 shows a temperature sequence for the sample from Manitou Springs. Fits of three spectra of differing degrees of complexity are shown in Figure 15. To fit the 300 K spectrum, a pair of doublets was used, whereas the 12 K spectrum was fit with a broadened and skewed sextet. The intermediate spectrum (150 K) includes both the doublet and sextet components discussed earlier. The results (Table 7) show that as temperature is lowered, the area of the doublet gradually decreases while the sextet area increases, a characteristic of superparamagnetic behavior. The values determined for the hyperfine parameters tend toward those of low temperature bulk goethite ($\alpha\text{-Fe}^{3+}\text{OOH}$), thus the conclusion that the iron-bearing phase of the Manitou Springs sample is nanophase goethite.

Spectra of the sample taken from Obsidian Pool (Figure 16) are somewhat more complex. The doublet-to-sextet conversion, indicative of superparamagnetism, is still observed, but takes place over a narrower temperature range, and an additional, more widely spaced sextet component, with smaller linewidths, appears. Analysis of the 250 K

spectrum is shown in Figure 17, with values of the fitted parameters given in Table 8.

The new spectral component is consistent with nanophase hematite ($\alpha\text{-Fe}^{3+}_2\text{O}_3$).

Variation of B_{hf} with temperature is shown (Figure 18) for the sextet components of the samples from Manitou Springs and Obsidian Pool, along with the variation for bulk goethite [Mørup *et al.*, 1983]. The upper curve in the figure lies well above the others, as expected for a hematite component ($T_N \gg 300$ K). The curves for the nanophase goethite components of the two samples are quite similar, with Néel temperature of ~ 275 K, well below that of bulk goethite ($T_N = 393$ K) [Coe, 1988].

Table 7. Manitou Springs Mössbauer Parameters

Temperature, K	IS, mm/s	QS, mm/s	B_{hf} , T	W, mm/s	Area, %
300	0.25	0.48	--	0.35	58.0
	0.25	0.89	--	0.42	42.0
250	0.29	0.55	--	0.46	36.5
	-0.08	-0.51	18.9	0.38	63.5
225	0.30	0.67	--	0.56	35.8
	0.32	-0.22	34.2	0.80	64.2
200	0.30	0.69	--	0.57	26.2
	0.35	-0.23	38.9	0.68	73.8
150	0.31	0.68	--	0.53	21.0
	0.37	-0.20	44.4	0.50	79.0
100	0.35	0.69	--	0.54	19.4
	0.41	-0.20	46.2	0.49	80.6
50	0.36	0.69	--	0.63	17.0
	0.41	-0.18	48.1	0.44	83.0
12	0.42	-0.15	49.2	0.43	100
bGt, 22K	0.47	-0.25	49.8	--	--

Fits modeled as a superposition of a doublet ($B_{\text{hf}} = 0$) plus a broadened and skewed sextet ($B_{\text{hf}} \neq 0$). Included also are reference values for bulk goethite (bGt) at 22 K [GTS3 sample of Morris *et al.*, 1989].

Mössbauer spectra acquired at 300 K for all samples (2Cx, 3Cx, 5Cx, and 6C1; Figures 19-21) fall into two distinct categories: a) broad ferric doublets (surface samples and those near the vent, 2C1, 3C1, 5C1-4, 6C1); and b) more complex spectra (samples at depth nearer the stream, 2C2-4, 3C2-4). Intuitively, these two categories correspond to samples that can be considered primary precipitates (at the surface or near the vent, 'surface' samples) and the 'subsurface' samples, which would have had the opportunity to undergo diagenetic change. A similar distinction has been made previously for the deep-sea vent samples when samples from active vents were contrasted with those from inactive vents [Agresti *et al.*, 1994].

Table 8. Obsidian Pool Mössbauer Parameters

Temperature, K	IS, mm/s	QS, mm/s	B _{hf} , T	W, mm/s	Area, %
300	0.24	0.55	--	0.46	89.7
	0.26	- 0.16	46.9	2.32	10.3
250	0.28	0.60	--	0.57	14.3
	0.33	- 0.19	48.3	0.70	6.6
	0.31	- 0.21	34.9	0.71	79.1
200	0.25	0.62	--	1.04	9.5
	0.34	- 0.12	49.7	0.47	5.3
	0.34	- 0.23	40.9	0.56	85.2
100	0.39	- 0.07	51.5	0.30	4.0
	0.40	- 0.19	47.1	0.43	92.0
12	0.43	- 0.05	51.8	0.34	22.7
	0.42	- 0.19	49.2	0.40	75.6
bGt, 22 K	0.47	- 0.25	49.8	--	--
nHm, 22 K	0.48	- 0.08	50.0	--	--

Fits modeled as in Table 7 with an additional sextet component. Included also are reference values for bulk goethite (bGt) and nanophase hematite (nHm)) at T = 22 K. [S6FN21 sample of *Morris et al.*, 1989]

B. Surface Samples

The broad ferric doublets characteristic of the seven surface samples were modeled in two ways, as a single doublet and as a pair of overlapping doublets with common isomer shift. Representative fits (for 6C1 and 2C1) are shown in Figure 22. Note that the 6C1 fit is improved with the two-site model; the 5C1-4 and 3C1 spectra (Figure 23) and are very similar. However, the model fails to fit the background for 2C1, suggesting a contribution from a weak magnetic component with transition temperature near 300 K. The results of the fits to the 300 K spectra of the seven surface samples are presented in Table 9, along with reported parameter values for ferrihydrite ($5\text{Fe}_2\text{O}_3 \cdot 9\text{H}_2\text{O}$ [Coey, 1988] or $\sim\text{Fe}_5\text{HO}_8 \cdot 4\text{H}_2\text{O}$ [Murad, 1988]). A close agreement exists between these parameter values (IS, QS, and W) and those measured for the seven surface samples.

A temperature study of the 6C1 sample (Figure 24) shows it to be similar to those of the 5C1-4 core samples. At 14 K, the peaks are still broad (a result of the amorphous nature of the samples), and a single broadened, skewed sextet model results in an adequate fit. The parameter values are all consistent with those reported for ferrihydrite at 4.2 K (Table 10). Together with the 300 K results, it is clear that the iron-bearing phase in the 6C1 and 5C1-4 samples (see Appendix B) is ferrihydrite with a Néel temperature, T_N , of ~ 45 K. This is consistent with reports having the T_N vary from 77 K down depending on the degree of crystallinity [Murad and Bowden, 1985]. The situation regarding the 2C1 and 3C1 samples is less clear. Although the 300 K data are consistent with ferrihydrite, no magnetic transition is observed down to 13 K. Judging from the low-temperature data, the weak magnetic component seen at 300 K in the 2C1 spectrum may be due to goethite (Table 11). This fact could possibly be due to the presence of

material (precursor to ferrihydrite) of such small particle size that 14 K is not sufficient for magnetic ordering.

Table 9. Mössbauer Parameters for Surface Samples at 300 K

Sample	IS, mm/s	QS, mm/s	W, mm/s	Area, %
2C1	0.35	1.07	0.38	36.0
	0.35	0.61	0.40	64.0
3C1	0.33	1.06	0.38	36.0
	0.33	0.59	0.42	64.0
5C1	0.34	1.08	0.42	48.0
	0.34	0.63	0.36	52.0
5C2	0.34	1.08	0.42	46.0
	0.34	0.63	0.37	54.0
5C3	0.35	1.10	0.39	40.0
	0.35	0.64	0.38	60.0
5C4	0.35	1.03	0.42	52.0
	0.35	0.58	0.35	48.0
6C1	0.35	0.80	0.45	100
6C1	0.35	1.09	0.41	45
	0.35	0.63	0.36	55
Feh*	0.35	0.7-0.85	>0.4	--
Feh*	0.35	~0.90	≈ 0.4	--
	0.35	~0.50	≈ 0.4	--

Fits modeled as a superposition of two doublets with common isomer shifts (including a one doublet fit for 6C1). Included also are reference fit results for natural ferrihydrite (Feh) [Murad, 1988].

XRPD patterns were obtained for the surface samples (Figure 25). They exhibit very broad bands characteristic of amorphous samples. Of course, clear identification from the diffraction pattern is not possible for amorphous material. However, the patterns, especially for 6C1 and 5C1-4, resemble very closely those reported for two-peak

ferrihydrates [Schwertmann, 1988], confirming the Mössbauer results. Note that additional, narrower peaks are observed in the diffraction patterns for 2C1 and 3C1, but not at positions expected for goethite. However, due to the close agreement of the Mössbauer and XRPD, final determination of these phases can be stated with some confidence because of the close association of goethite and ferrihydrate in nature [Schwertmann, 1988].

Table 10. Sample 6C1 Mössbauer Parameters

Temperature, K	IS, mm/s	QS, mm/s	B _{hf} , T	W, mm/s	Area, %
300K	0.35	1.08	--	0.41	46.0
	"	0.63	--	0.36	54.0
100K	0.46	1.11	--	0.44	49.2
	"	0.63	--	0.36	50.8
50K	0.44	1.16	--	0.48	45.0
	"	0.65	--	0.42	55.0
45K	0.47	0.95	--	0.83	92.5
	"	0.61	--	0.31	7.5
30K	0.48	-0.04	38.1	1.06	100
25K	0.47	-0.03	41.4	0.97	100
20K	0.47	-0.03	44.0	0.89	100
14K	0.47	-0.03	46.0	0.73	100
Feh (4.2 K)	0.46	-0.02 - ~ -0.1	46.5 - 50.0	0.9 ~1.7	--

Fits modeled as in Table 9 for higher temperatures. At lower temperatures, fits modeled with a broadened and skewed sextet. Included also are reference values for ferrihydrate (Feh) at T = 4.2 K, where widths are given for the outer lines. For 6C1 at 14 K, outer lines are ~1.4 mm/s.

C. Subsurface Samples

The 2C3 sample, a widely spaced doublet, characteristic of ferrous iron, dominates the 300 K spectrum of this sample (Figure 26). However, the two peaks

Table 11. Sample 2C1 Mössbauer Parameters.

Temperature, K	IS, mm/s	QS, mm/s	B _{hf} , T	W, mm/s	Area, %
300	0.35	1.05	—	0.51	66.5
	0.35	0.60	—	0.42	16.1
	0.46	-0.33	29.5	3.50	17.4
200	0.41	0.95	—	0.56	39.0
	0.41	0.54	—	0.33	13.3
	0.46	-0.29	35.1	3.00	47.7
25	0.40	0.79	—	0.53	68.5
	0.67	0.83	—	0.36	21.3
	0.48	-0.28	50.1	0.49	10.2
20	0.45	0.55	—	0.49	27.7
	0.47	0.97	—	0.69	62.9
	0.49	-0.29	50.4	0.42	9.4
17	0.46	0.79	—	0.90	92.1
	0.47	-0.27	50.2	0.30	7.9
15	0.44	0.76	—	0.99	90.5
	0.48	-0.29	50.3	0.26	9.5
13	0.44	0.73	—	1.09	88.6
	0.46	-0.27	50.2	0.29	11.4
bGt, 22K	0.47	-0.25	49.8	—	—

Fits modeled as a superposition of two doublets at higher temperatures, a sextet and a superposition of doublets at 25K, and a sextet plus a doublet at 13 K. Included also are reference values for bulk goethite (bGt) at 22 K [Morris *et al.*, 1989a and 1989b].

are not symmetric, with the near zero-velocity peak being more intense with some broadening near its base, and there is evidence in the background of a weak, magnetic component. A good fit is obtained with a four-site model (one ferrous doublet, two ferric doublets, and one sextet; Figure 27), with results given in Table 12. Parameter values for the ferrous component are consistent with those reported [Ono and Ito, 1964] for siderite $\text{Fe}^{2+}\text{CO}_3$. The two ferric doublets resemble a broadened singlet, similar to that reported [Sherman and Vergo, 1988] for the smectite clay mineral, nontronite $[(\text{Ca},\text{Na})_{0.66}$

$\text{Fe}^{3+}_4\text{Si}_{7.34}\text{Al}_{0.66}\text{O}_{20}(\text{OH})_4 \cdot n\text{H}_2\text{O}$], and the magnetic component is consistent with nanophase goethite.

In Figure 26, the full temperature sequence of the 2C3 sample, the most striking aspect is an apparent migration of the high velocity siderite peak, between ~45 K and 30 K, to ultimately overlap the fifth peak of a magnetic sextet at 14 K. At the same time, the central region of the spectrum becomes extremely complex, making the analysis very difficult. A temperature sequence (Figure 28) of ground natural siderite (Copper Lake, Antigonish Co., Nova Scotia) shows a similar behavior, with a magnetic transition as temperature is lowered and subsequent increase in B_{hf} . A fit of the 14 K spectrum is shown in Figure 29. Analysis of the 14 K spectrum of the 2C3 sample is shown Figure 30, where the contribution of the siderite sextet is evident. In addition, the spectrum contains a nanophase goethite sextet and a broadened singlet, also observed at 300 K. The fit results for the entire temperature sequence are given in Table 10. One can infer that the transition temperature for the nanophase goethite component is greater than that observed for Manitou Springs or Obsidian Pool from the 300 K spectrum of Figure 27. Variation of B_{hf} and QS with temperature are shown in Figure 31 and 32, respectively, for the Nova Scotia siderite and the siderite component of 2C3 along with plotted values for a synthetic siderite (99.5% pure FeCO_3) [Ok, 1969]. It appears that these three siderite phases converge very nearly to the same low temperature limit of B_{hf} , but have distinctly different magnetic transition temperatures, presumably due to different modes of production and possibly different degrees of substitution for iron in the siderite structure of the natural samples. Like goethite and ferrihydrite, it is obvious that natural siderite(s) exhibit a range of magnetic transition temperatures.

Table 12. Sample 2C3 Mössbauer Parameters

Temperature, K	IS, mm/s	QS mm/s	B _{hf} , T	W, mm/s	Area, %
300	0.23	0.41	--	0.35	13.5
	0.23	1.08	--	0.54	13.6
	1.12	1.78	--	0.27	48.7
	0.32	-0.33	29.9	2.12	24.2
100	0.39	0.44	--	0.61	18.2
	1.37	2.00	--	0.32	47.1
	0.46	-0.26	48.8	0.60	34.7
50	0.42	0.26	--	0.75	17.7
	1.39	2.06	--	0.36	47.3
	0.47	-0.27	49.9	0.54	35.0
45	0.49	--	--	0.70	19.6
	1.39	2.08	--	0.39	46.0
	0.48	-0.25	49.8	0.50	34.4
42.5	0.34	0.18	--	0.32	11.6
	0.34	0.89	--	0.65	4.0
	1.51	2.08	3.79	0.26	28.4
	0.49	-0.28	50.0	0.45	--
40	0.48	0.19	--	0.46	24.0
	0.48	1.19	--	0.20	2.2
	1.34	2.04	12.0	0.26	43.0
	0.49	-0.28	50.0	0.39	30.8
37.5	0.46	0.17	--	0.40	20.9
	0.46	1.02	--	0.44	7.7
	1.36	2.09	13.8	0.20	35.6
	0.49	-0.28	50.2	0.40	35.9
30	0.46	0.21	--	0.38	22.1
	0.46	1.10	--	0.65	10.9
	1.38	2.10	15.9	0.24	35.2
	0.49	-0.28	50.3	0.34	31.8
14	0.46	0.21	--	0.42	33.1
	0.46	1.08	--	0.39	36.3
	1.38	2.08	17.1	0.20	24.9
	0.49	-0.28	50.3	0.28	5.7
bGt, 22K	0.47	-0.25	49.8	--	--
FeCO ₃ , 300K	1.38(2)	1.87(10)	--	--	--
FeCO ₃ , 20K	--	2.10(20)	17.2(1.5)	--	--

Fits modeled as discussed previously in the text. Included also are reference values for bulk goethite (bGt) at 22 K and for siderite (FeCO₃)[Ono and Ito, 1964].

The XRPD pattern of the 2C3 sample is shown in Figure 33 where the three iron-bearing phases, siderite, goethite, and nontronite are identified by the peak labels, S, N, and G. Note that the identification of the broadened Mössbauer singlet as nontronite is

confirmed by XRPD. The assignment of the XRPD peaks appears to be complete, with no other phases being identified. Mössbauer spectroscopy reveals all the mineral components present in 2C3 that are observable with the x-ray diffraction technique.

As for the other subsurface samples, the temperature sequences for samples 2C2 and 2C4 are shown in Figure 34 and 35. Similar low temperature spectra obtained for 3C2-3C4 with spectral analysis similar to that of the 2C3 analysis. The results indicate that these five additional subsurface samples contain the same phases as 2C3, plus hematite, in varying proportions.

An XRPD pattern was obtained for each of the subsurface samples (Figure 36 and 37), showing siderite, nontronite, and goethite identified by their well-defined peaks; however, hematite is not seen. The assignments from Mössbauer spectroscopy are verified.

FESEM and EDX analyses [*Wade et al.*, 1998] reveal that the surface samples exhibit physical and chemical properties that are indeed consistent with the identification of the primary iron oxide precipitate, ferrihydrite, also inferred from Mössbauer and XRPD. However, examination of samples nearer the vent, using light microscopy, showed what appears to be amorphous Fe-oxides interbedded with discrete laminae of amorphous silica and Fe-rich silicates (clays), consistent with FESEM results. XRPD analysis of these samples confirms the amorphous nature of these materials, suggesting that the silica is amorphous (probably Opal-A) and that the Fe-rich silicate is probably a smectite clay, possibly nontronite.

In samples 2C2-4 and 3C2-4, siderite (Fe-carbonate) was identified over a depth range of 1-8 mm using both Mössbauer and XRD. It was not, however, observed in

surface samples. EDX results are consistent with the presence of an Fe-carbonate in sample 2C3. It may also be present at depth in sample 5C, based on the presence of Ca in the EDX spectrum. But under FESEM, no distinct carbonate mineral grains were identified, the carbonate being indistinguishable from the other fine-grained microgranular materials present. The exclusively subsurface occurrence of the siderite suggests it is authigenic. The general increase in pH with depth suggests that it may be precipitating in response to microbial processes (e.g., sulfate reduction, which increases pH) [Beverly Pierson, 1997, personal communication]. In these same samples (2C2-4, 3C2-4), nontronite (an Fe-rich smectite clay) and crystalline Fe-oxides (hematite and goethite) are also present. This suggests that the primary amorphous phase, ferrihydrite, which is being deposited at the surface in this system, is being diagenetically altered to form these ordered phases as the mound accretes and surface sediments become progressively buried.

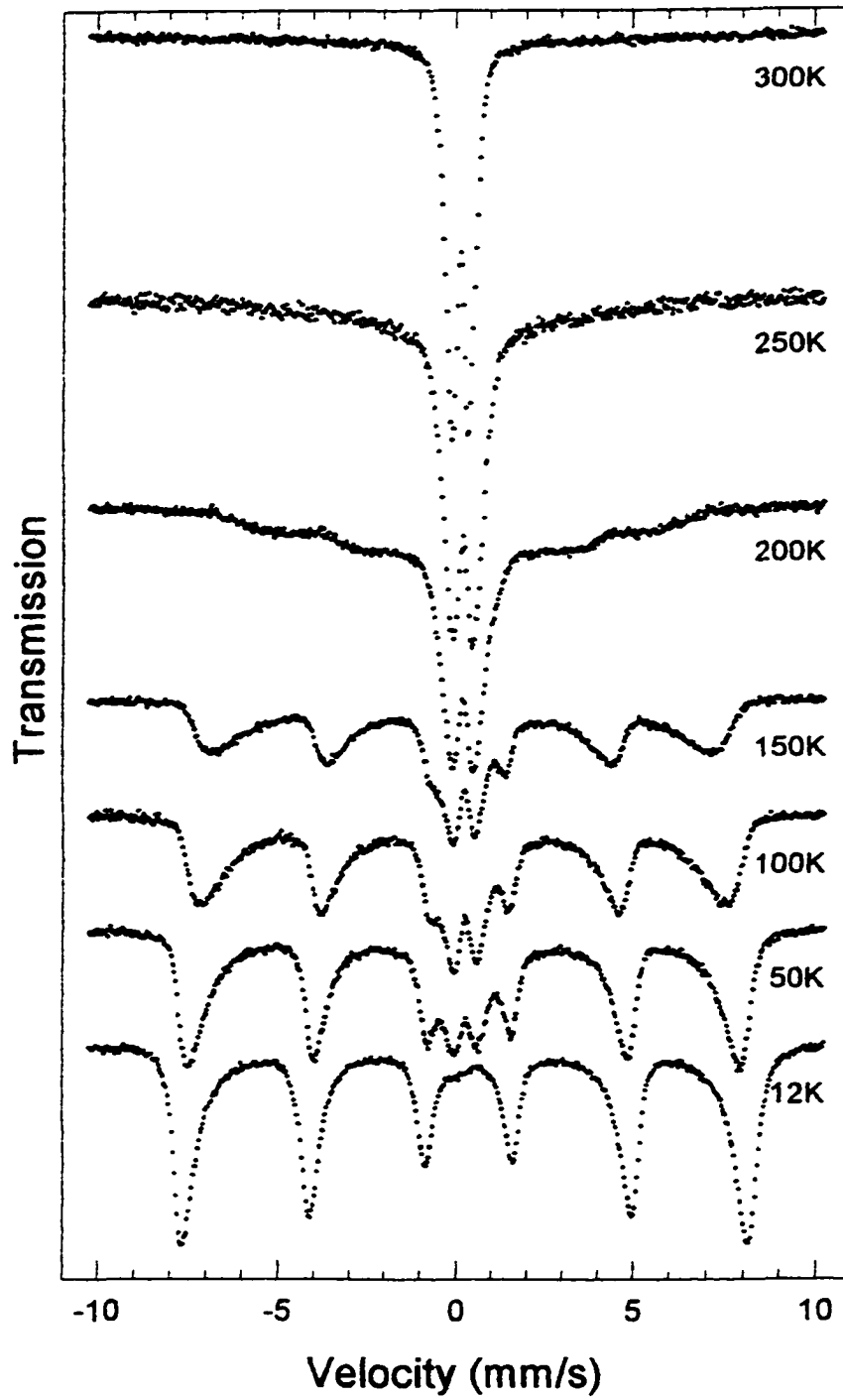


Figure 14. Mössbauer spectra of Manitou Springs temperature sequence.

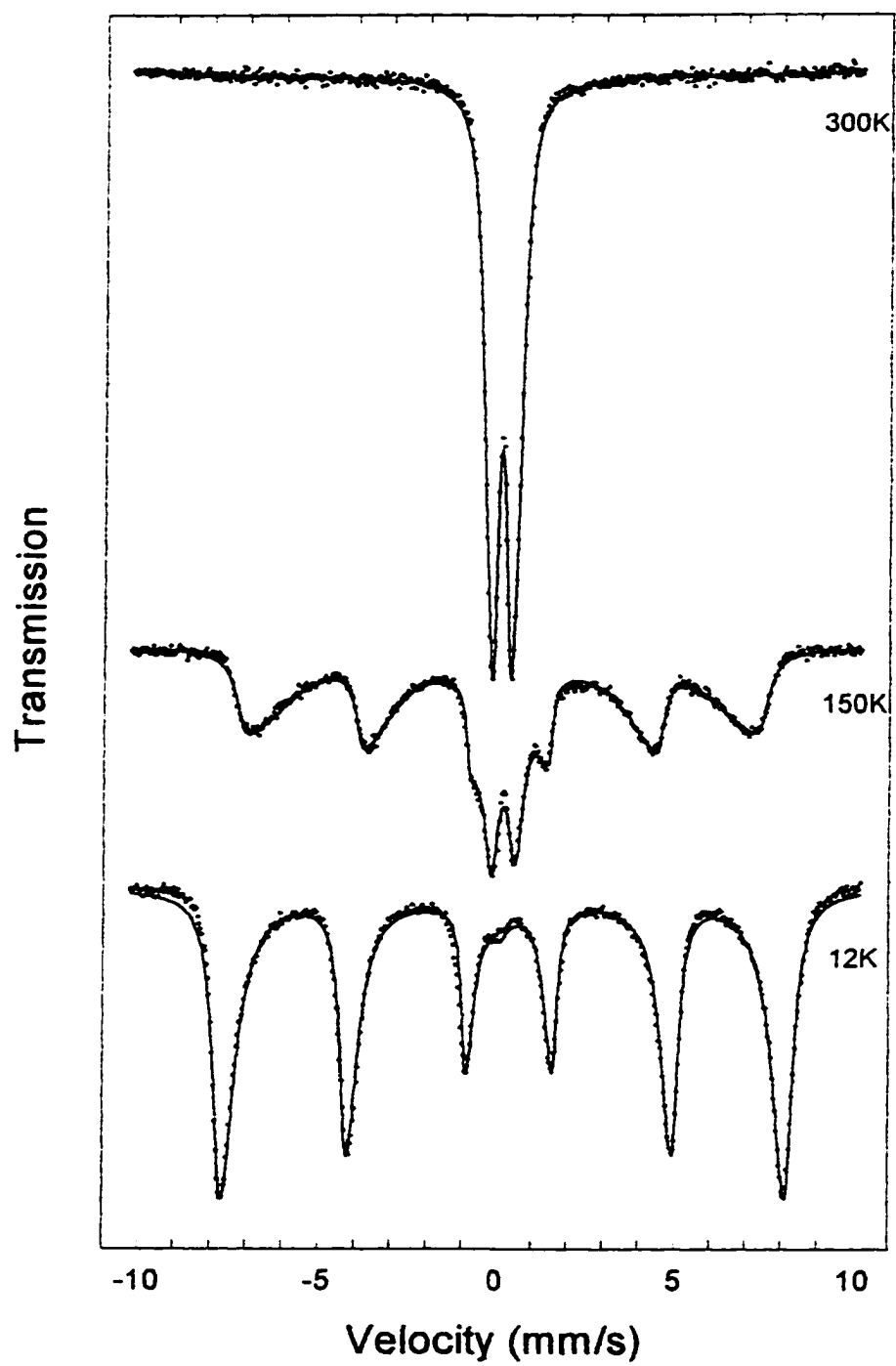


Figure 15. Fit of Manitou Springs spectra at 300 K, 150 K, and 12 K.

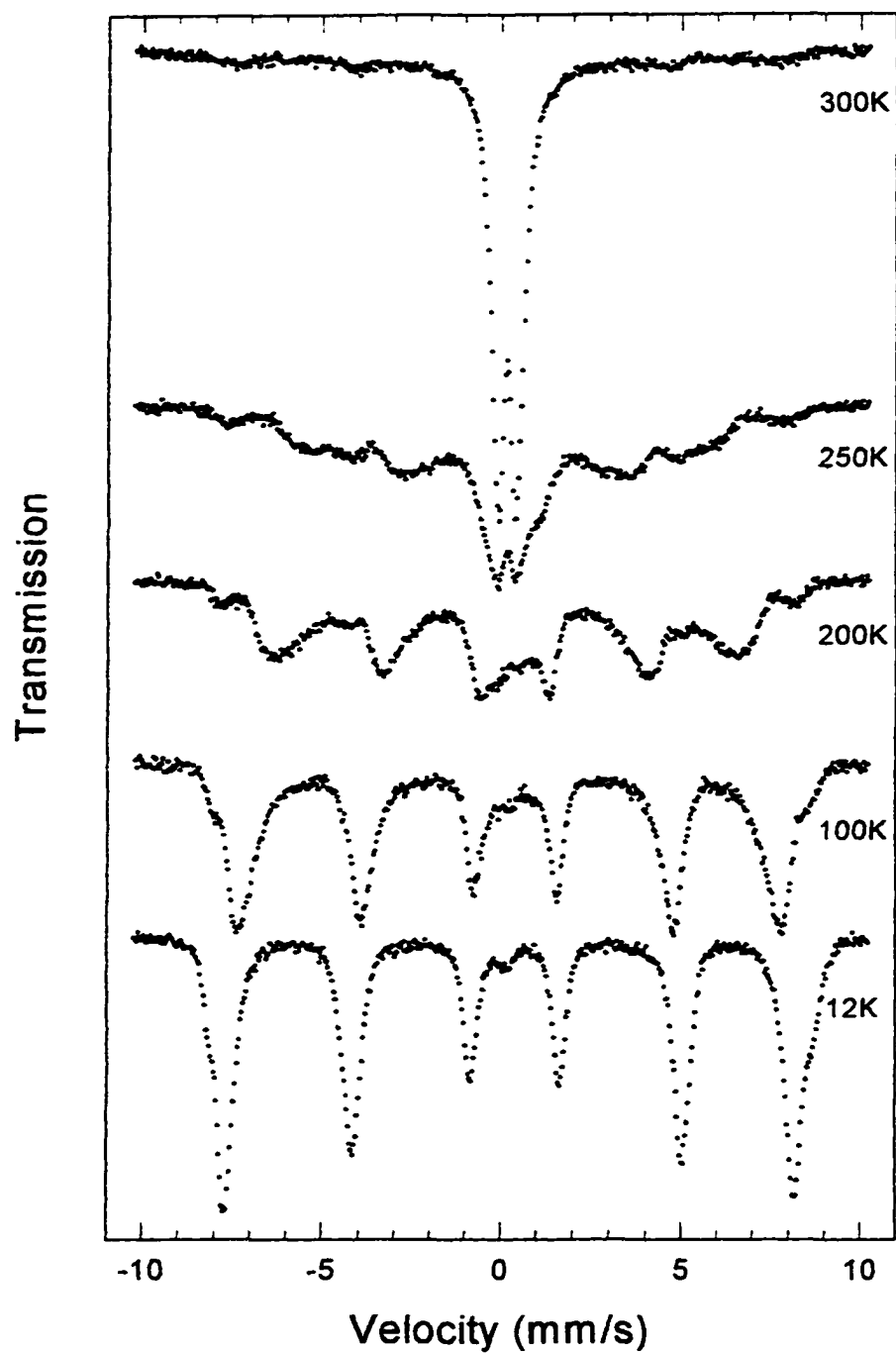


Figure 16. Mössbauer spectra for Obsidian Pool temperature sequence.

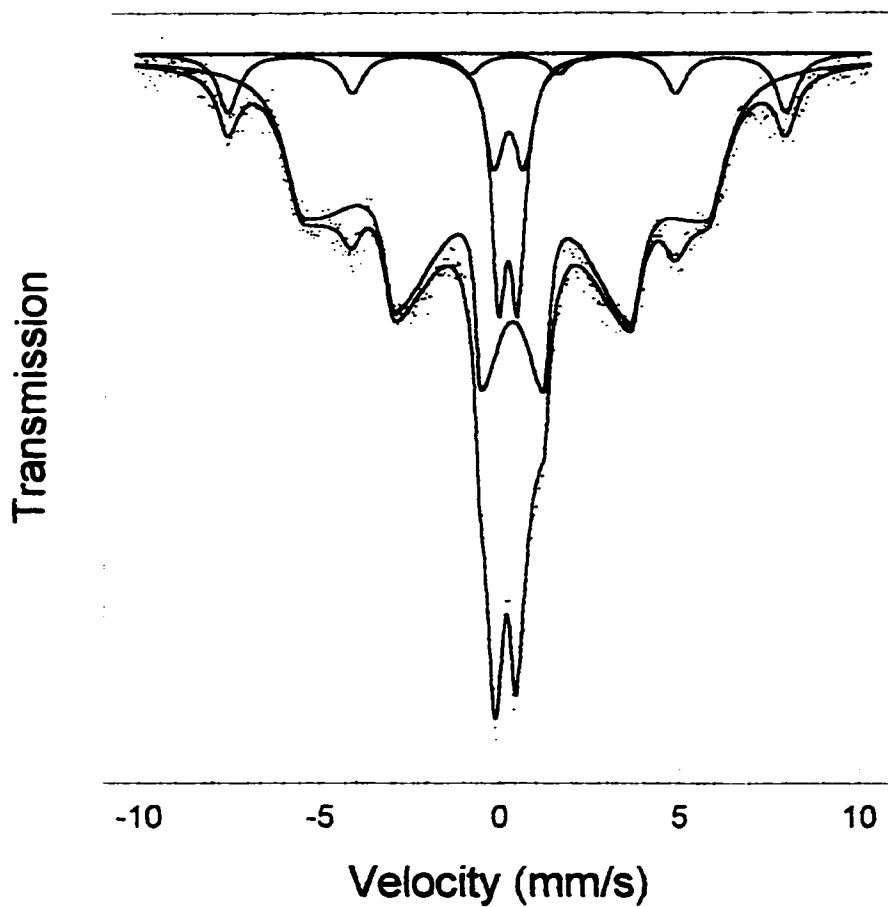


Figure 17. Fit of Obsidian Pool 250 K Mössbauer spectrum showing component sites.

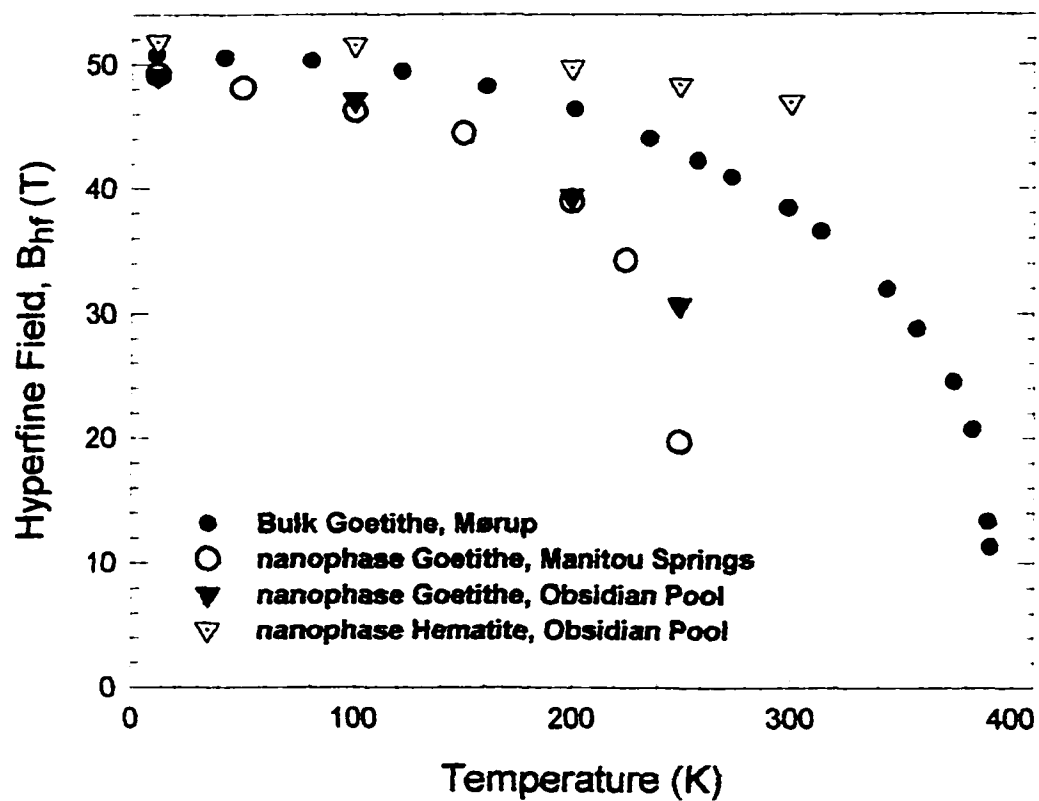


Figure 18. Variation of B_{hf} with temperature for the Manitou Springs, Obsidian Pool, and a bulk goethite sample [Mørup *et al.*, 1983].

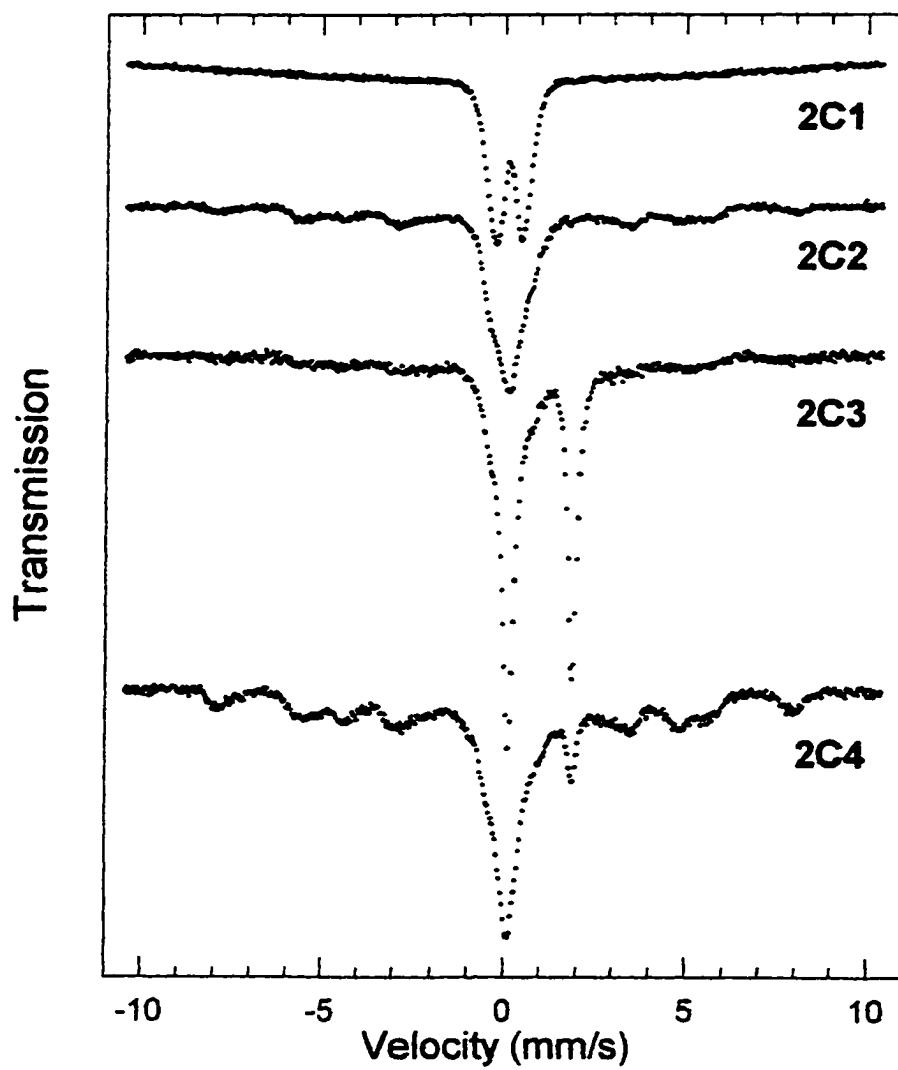


Figure 19. Mössbauer spectra for the 2C core sample.

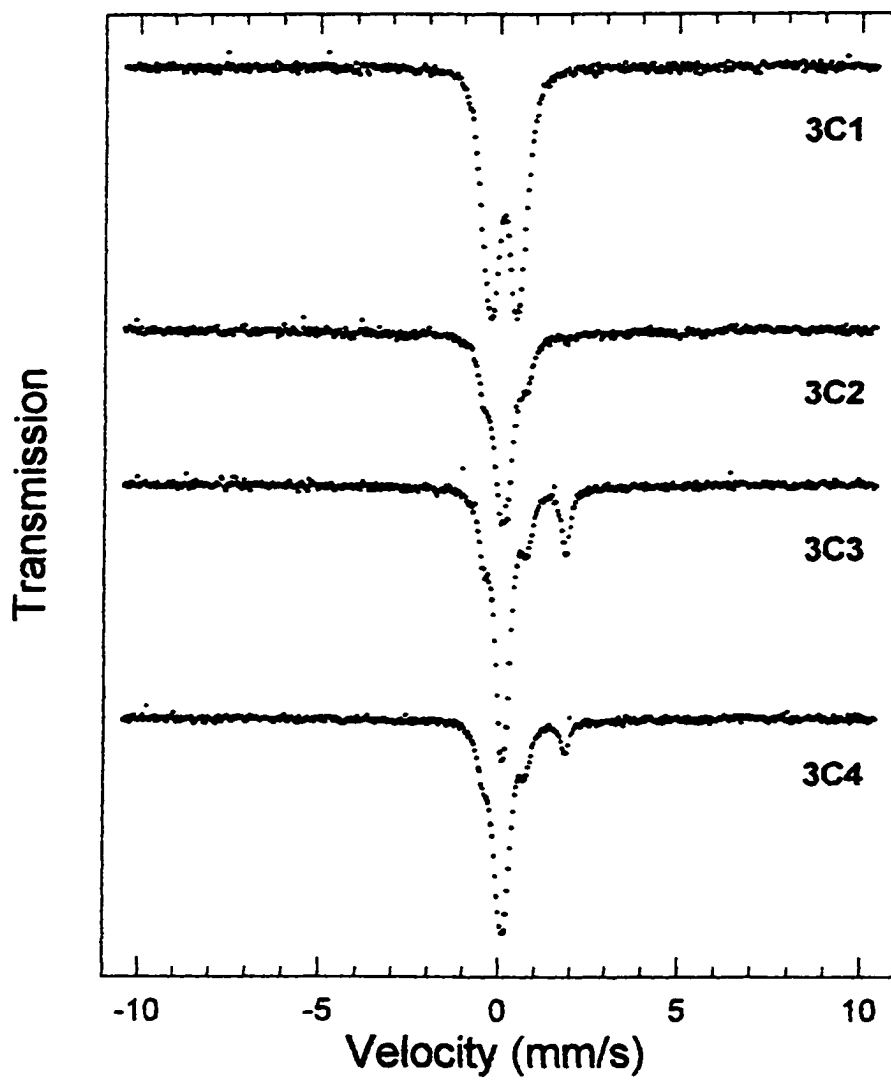


Figure 20. Mössbauer spectra for the 3C core sample.

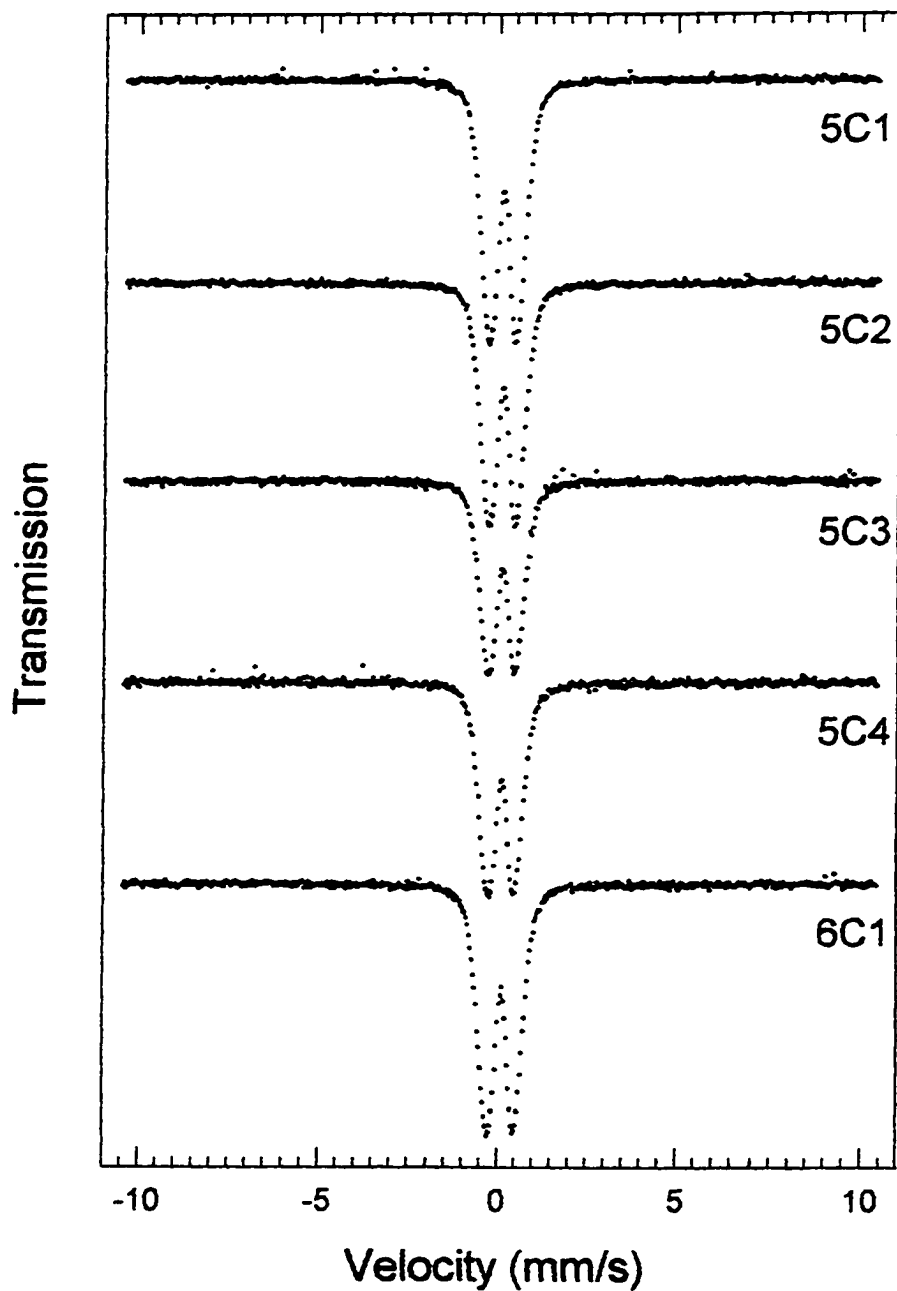


Figure 21. Mössbauer spectra for the 5C core and 6C1 sample.

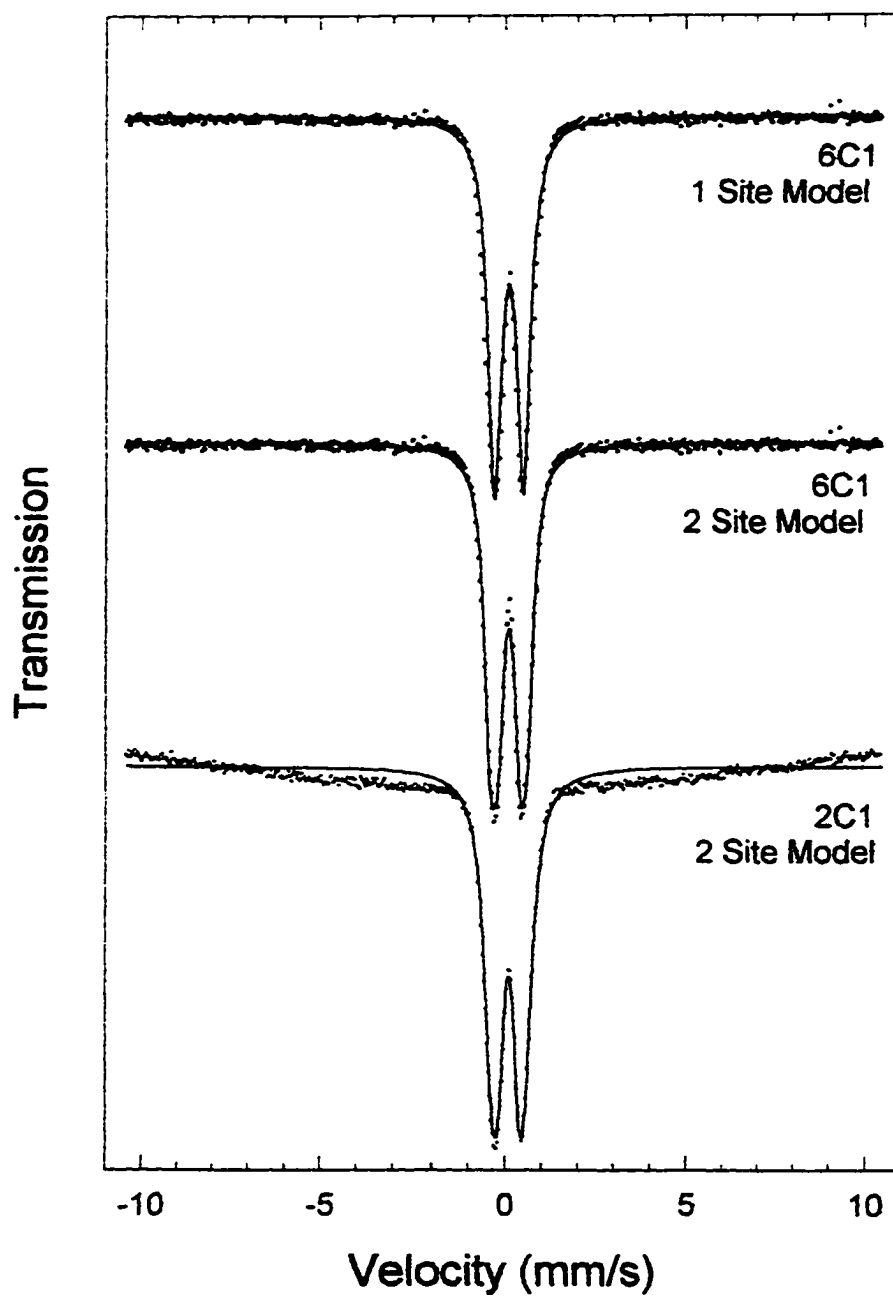


Figure 22. Fits of the 6C1 and 2C1 Mössbauer spectra at 300 K.

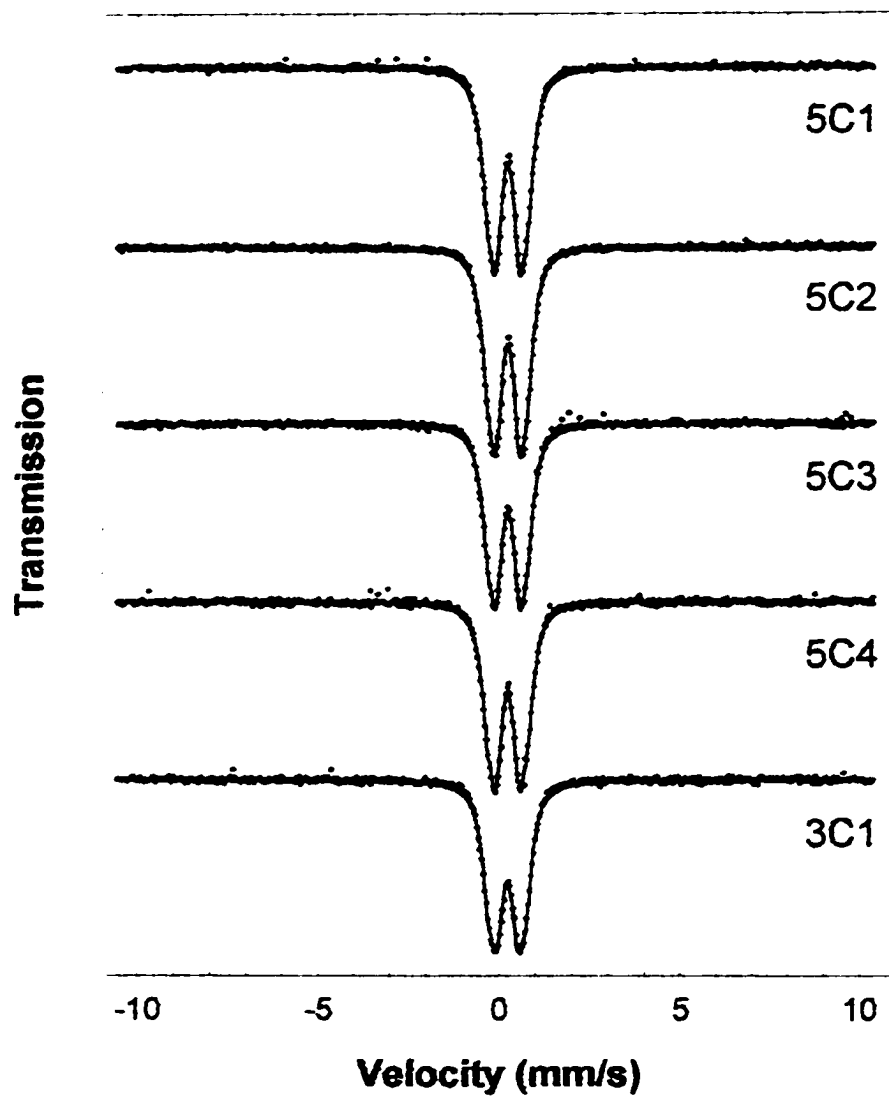


Figure 23. Fits of the 5C1-4 and 3C1 Mössbauer spectra at 300 K.

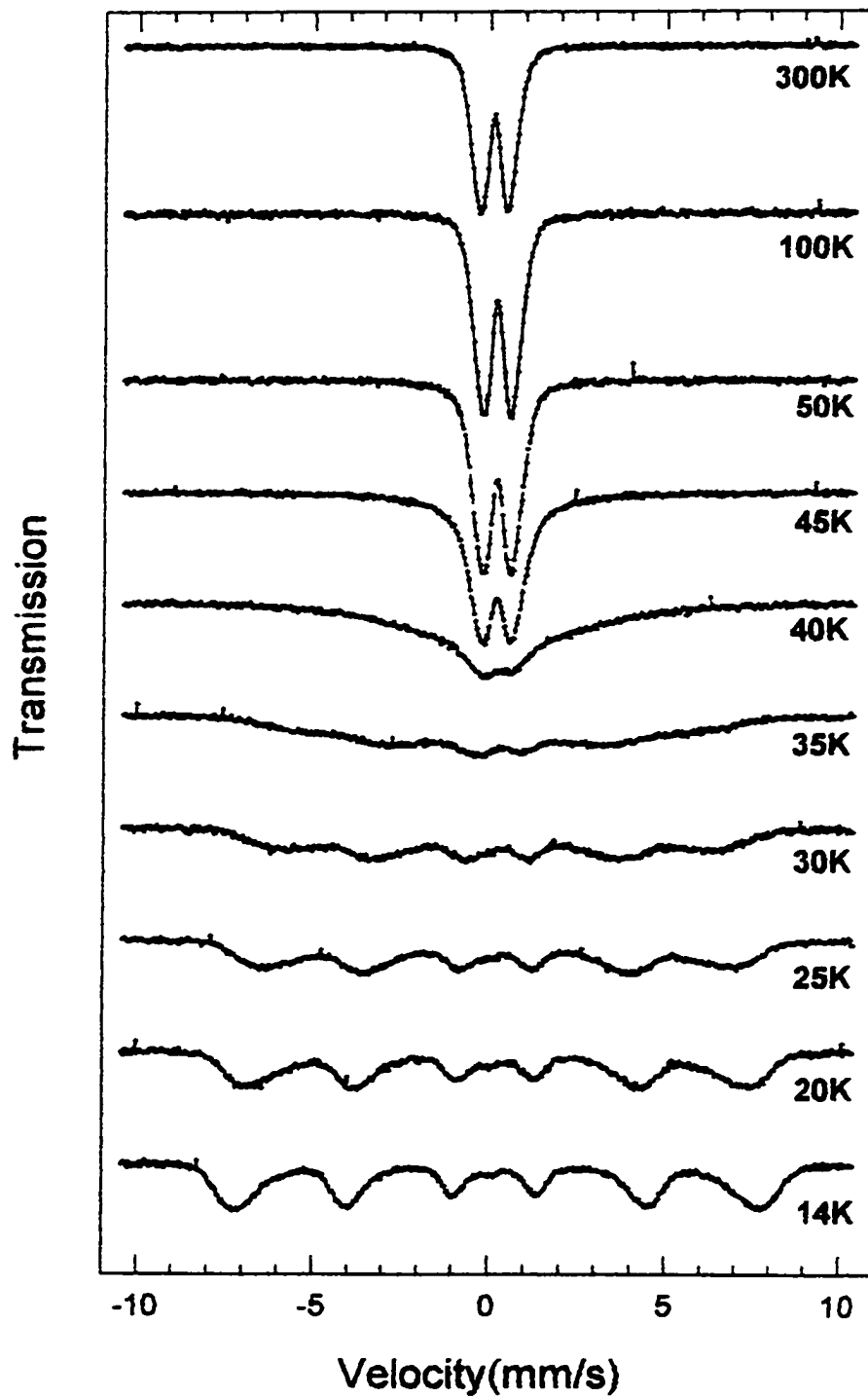


Figure 24. Mössbauer spectra of the 6C1 temperature sequence.

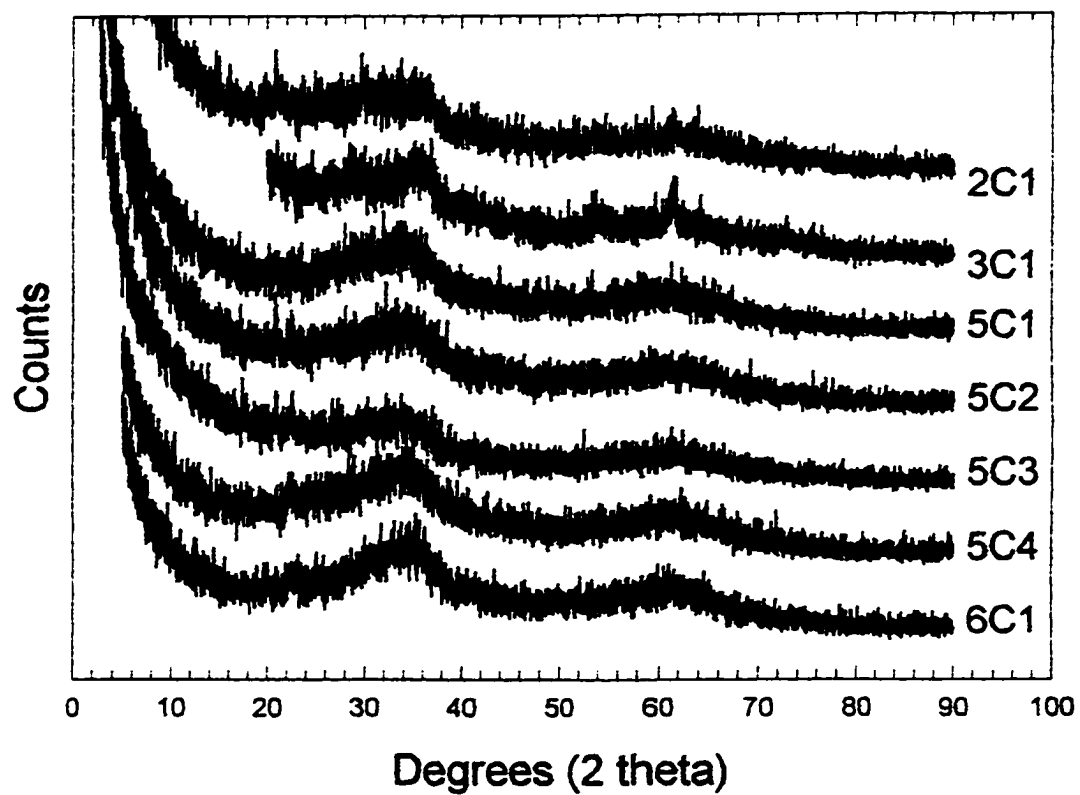


Figure 25. X-ray diffraction spectra for powdered surface samples.

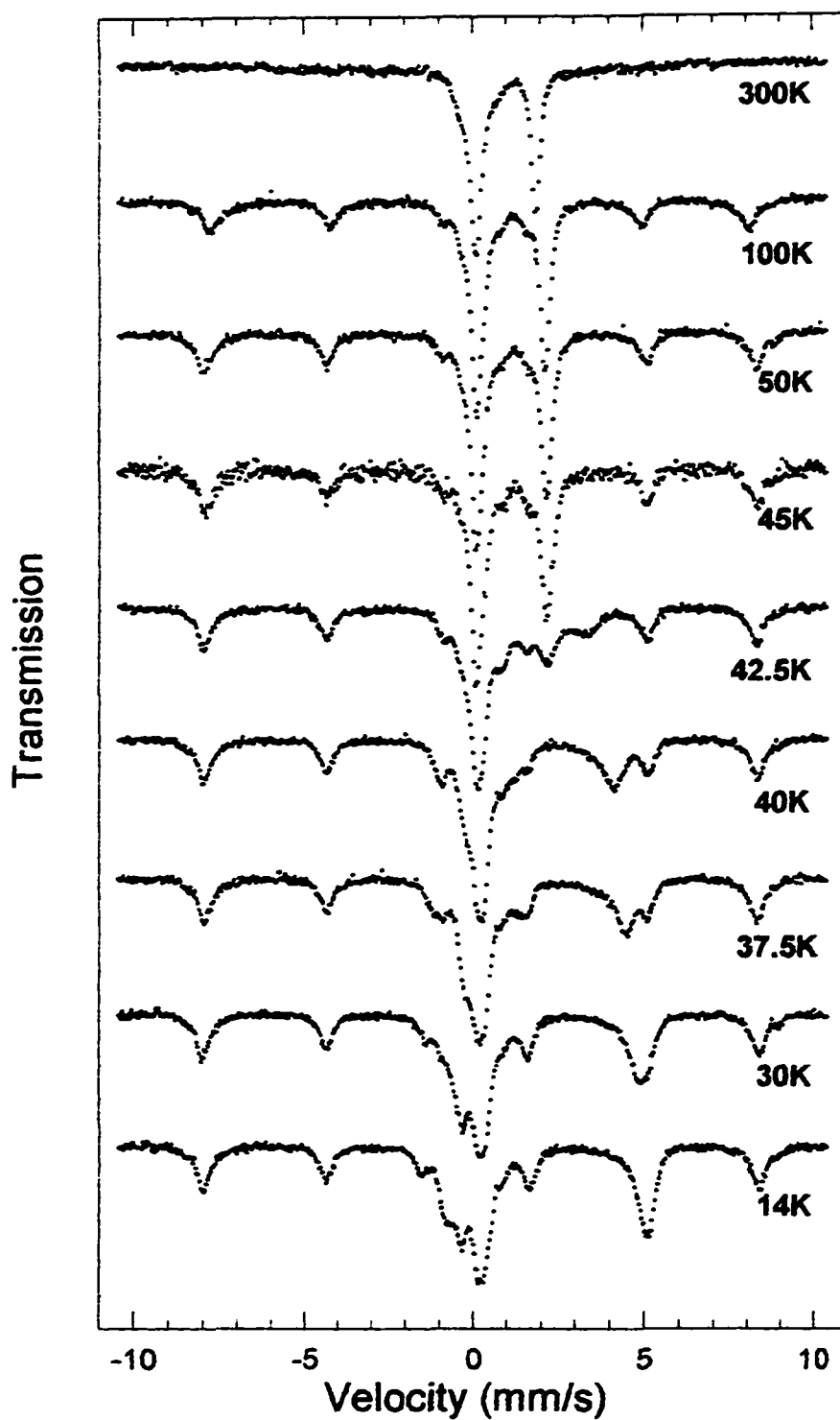


Figure 26. Mössbauer spectra for the 2C3 temperature sequence.

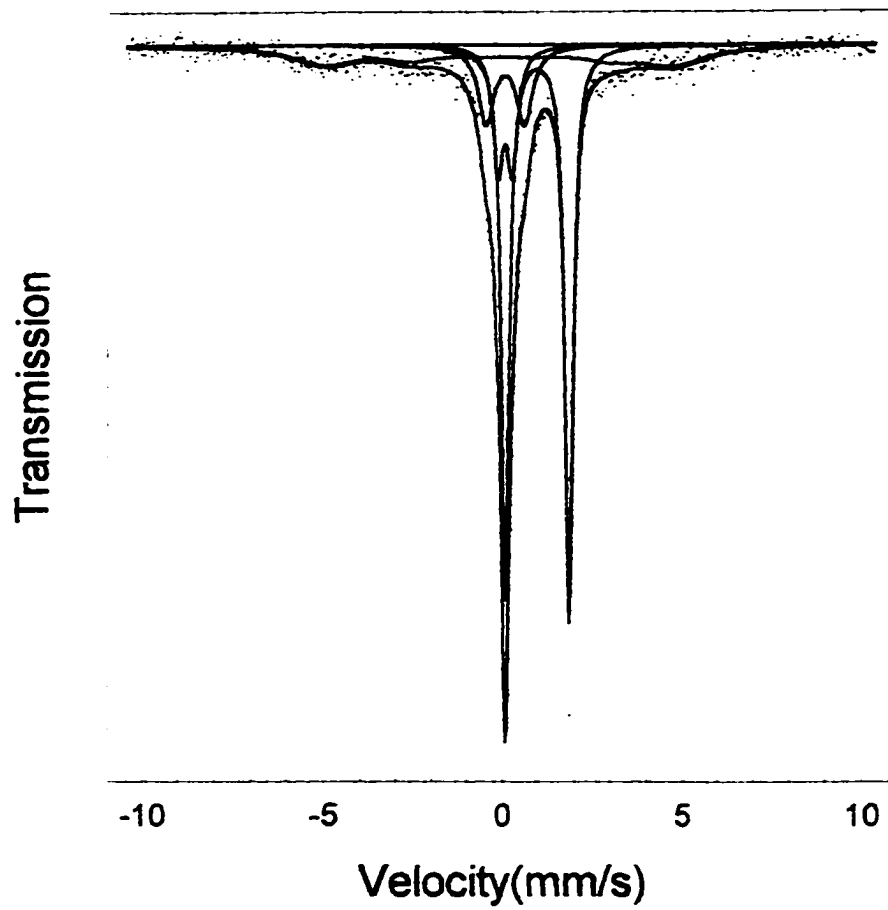


Figure 27. Fit of 2C3 sample at 300 K showing component spectra.

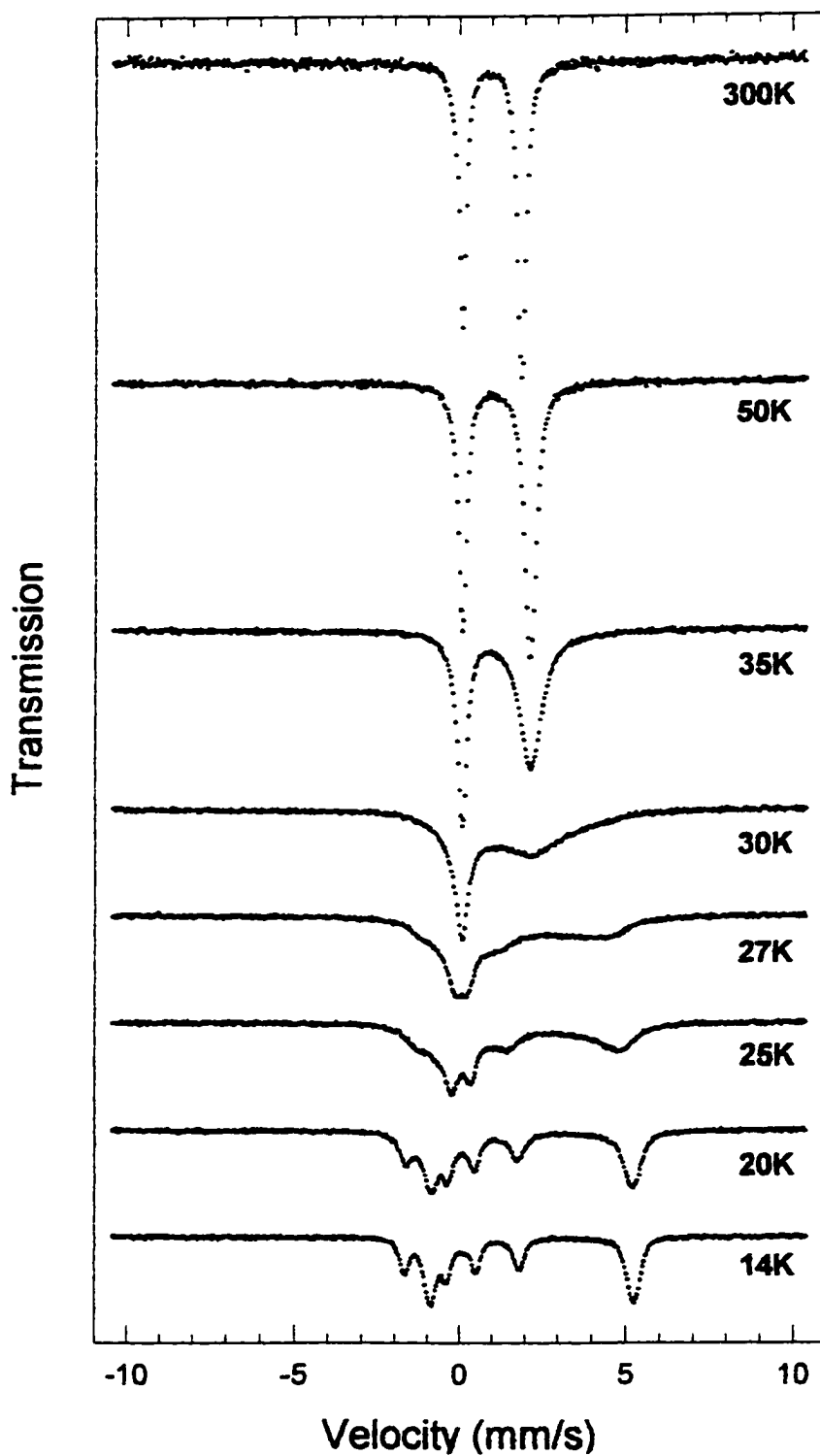


Figure 28. Mössbauer spectra of the natural (Nova Scotia) siderite temperature sequence.

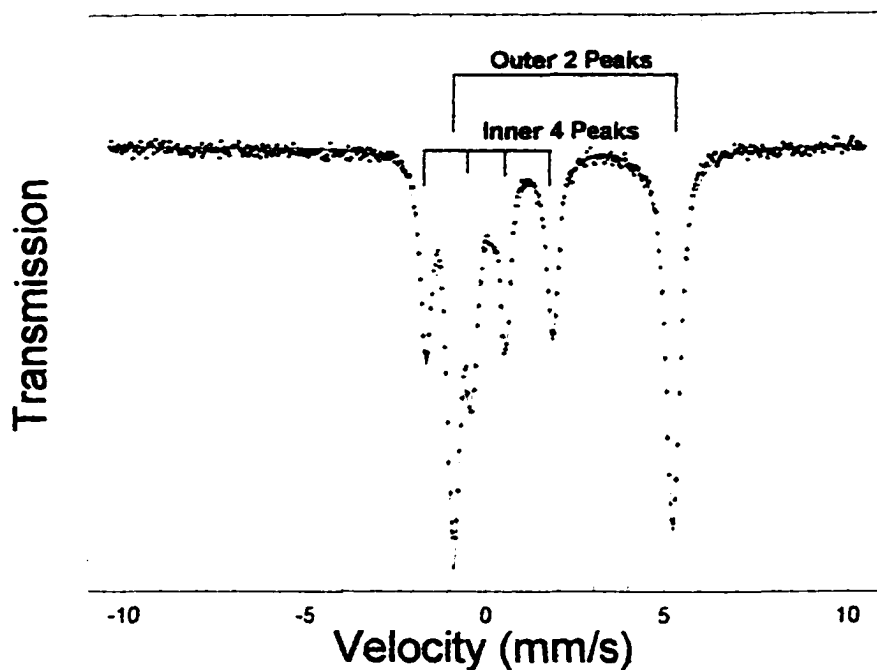


Figure 29. Fit of the natural (Nova Scotia) siderite at 14 K.

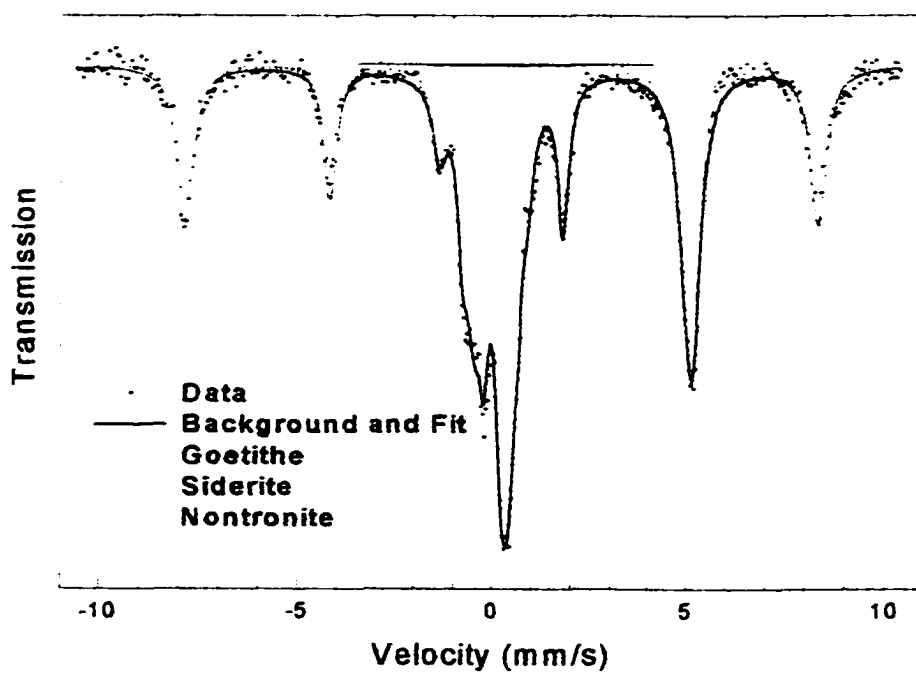


Figure 30. Fit of the 2C3 sample at 14 K showing the component spectra.

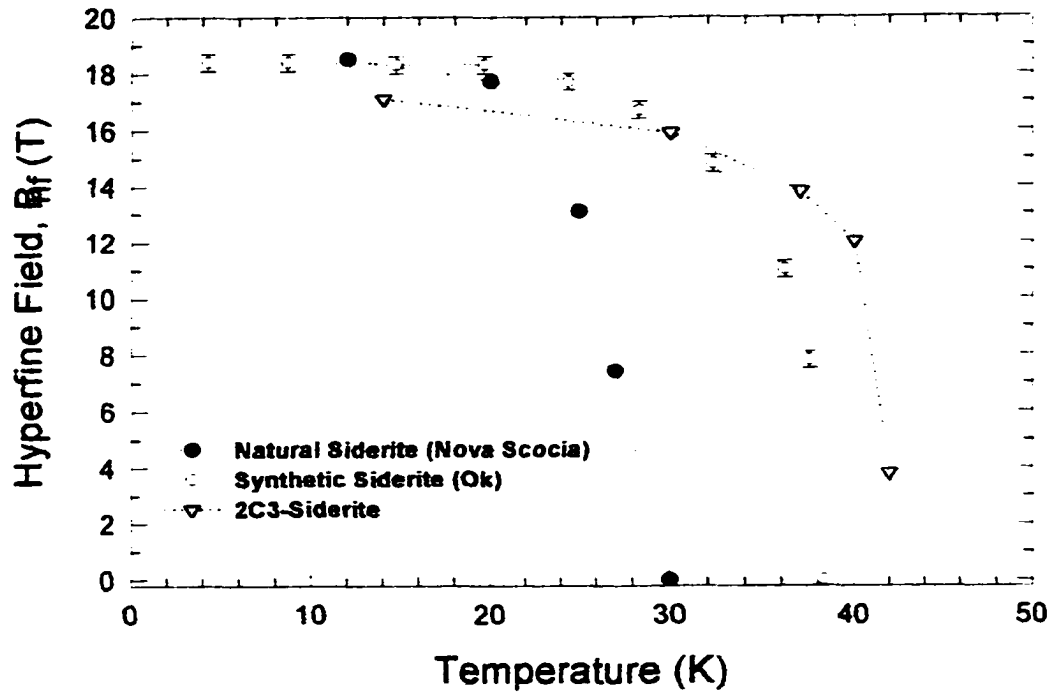


Figure 31. Variation of B_{hf} with temperature for the 2C3 (component), Nova Scotia, and a synthetic (pure) siderite.

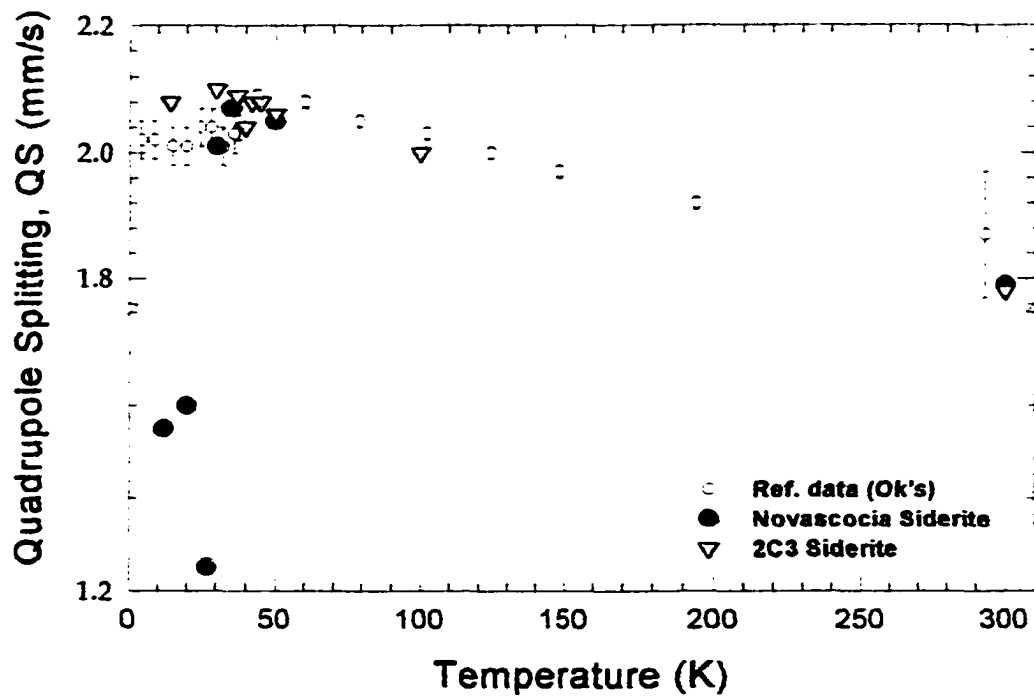


Figure 32. Variation of QS with temperature for the 2C3 (component), Nova Scotia, and a synthetic (pure) siderite.

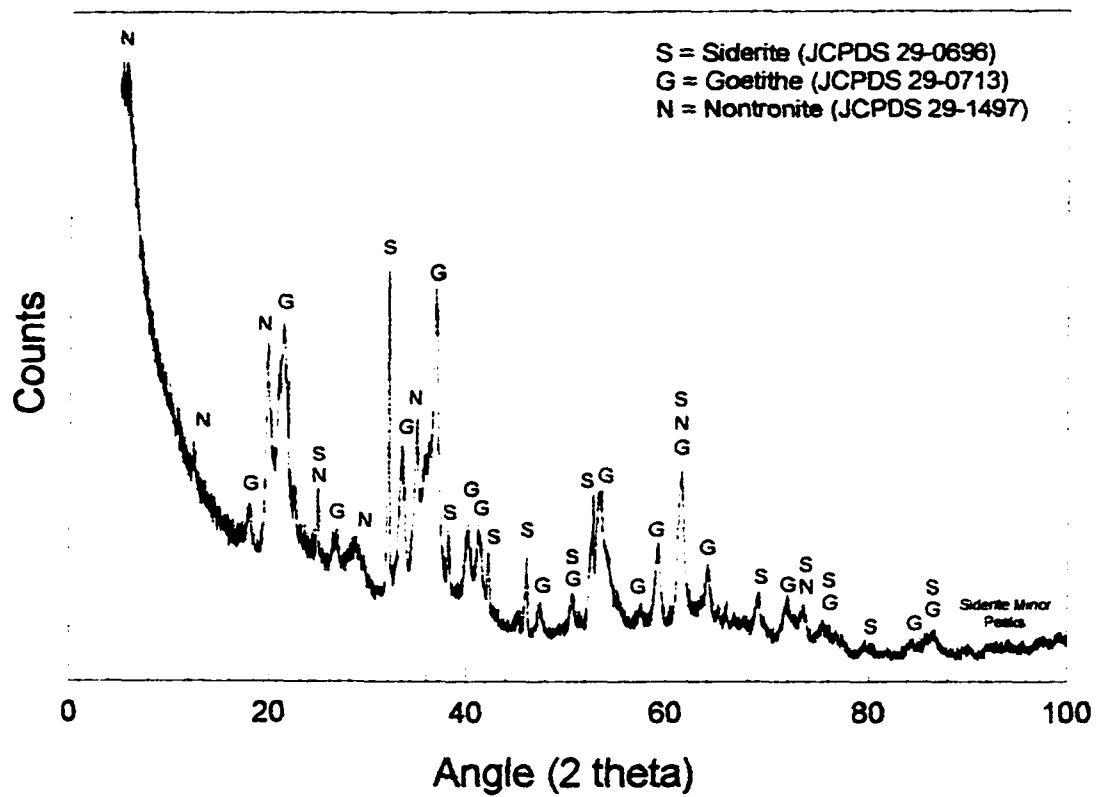


Figure 33. X-ray diffraction spectrum for the powdered 2C3 sample.

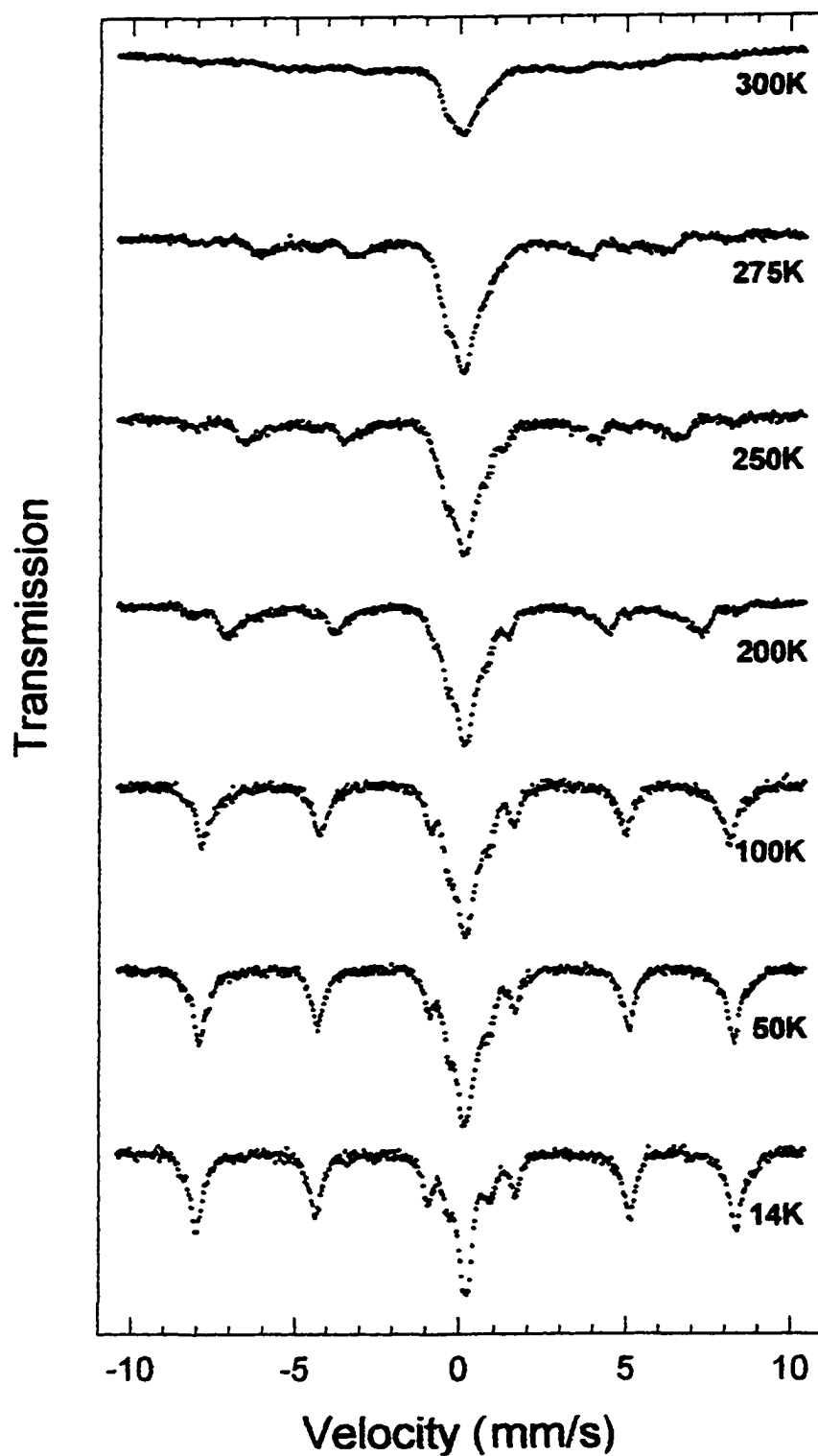


Figure 34. Mössbauer spectra for the 2C2 sample temperature sequence.

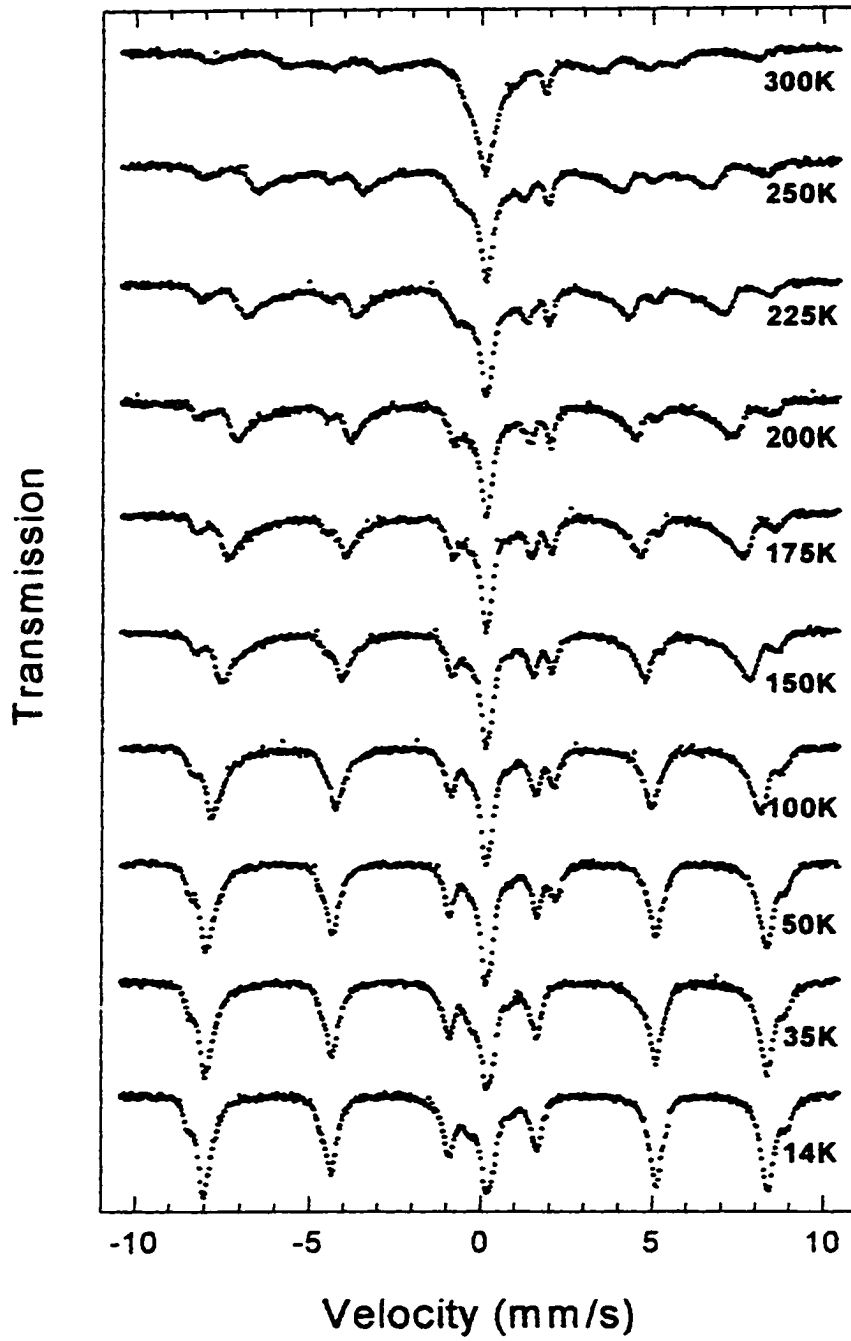


Figure 35. Mössbauer spectra for the 2C4 sample temperature sequence.

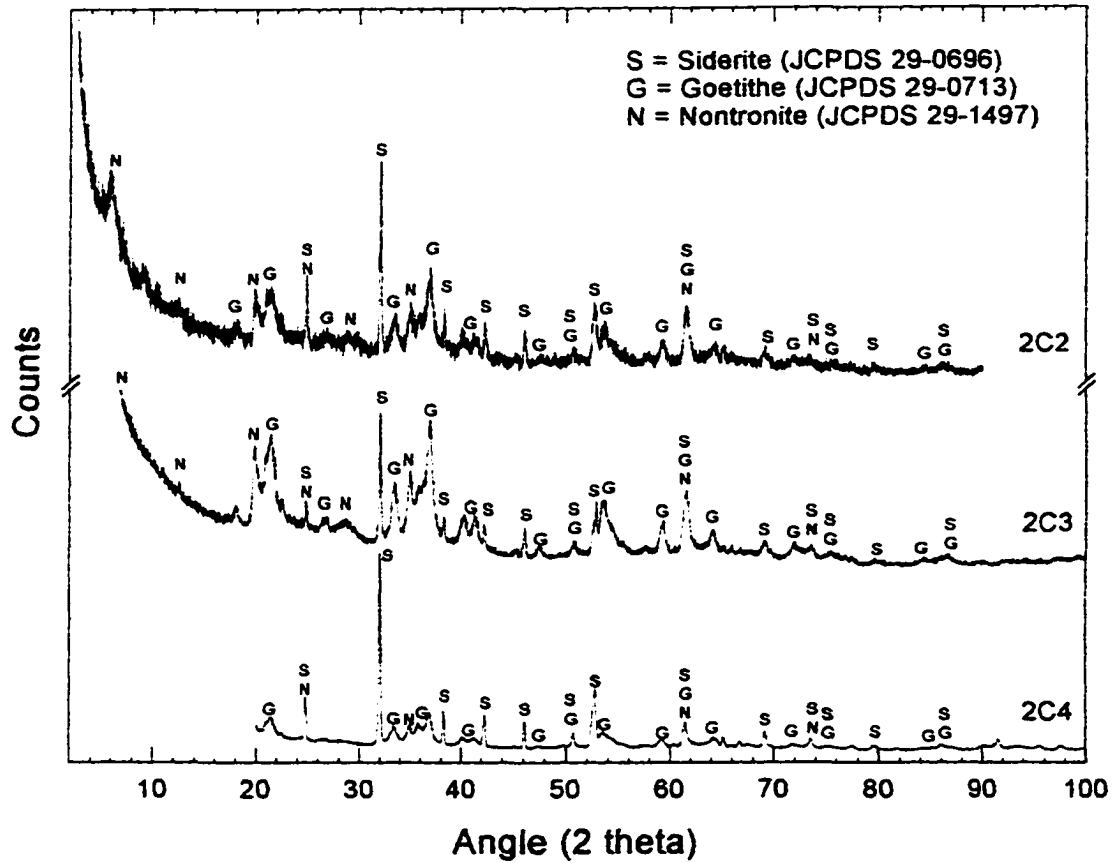


Figure 36. X-ray diffraction spectra for powdered 2C core samples.

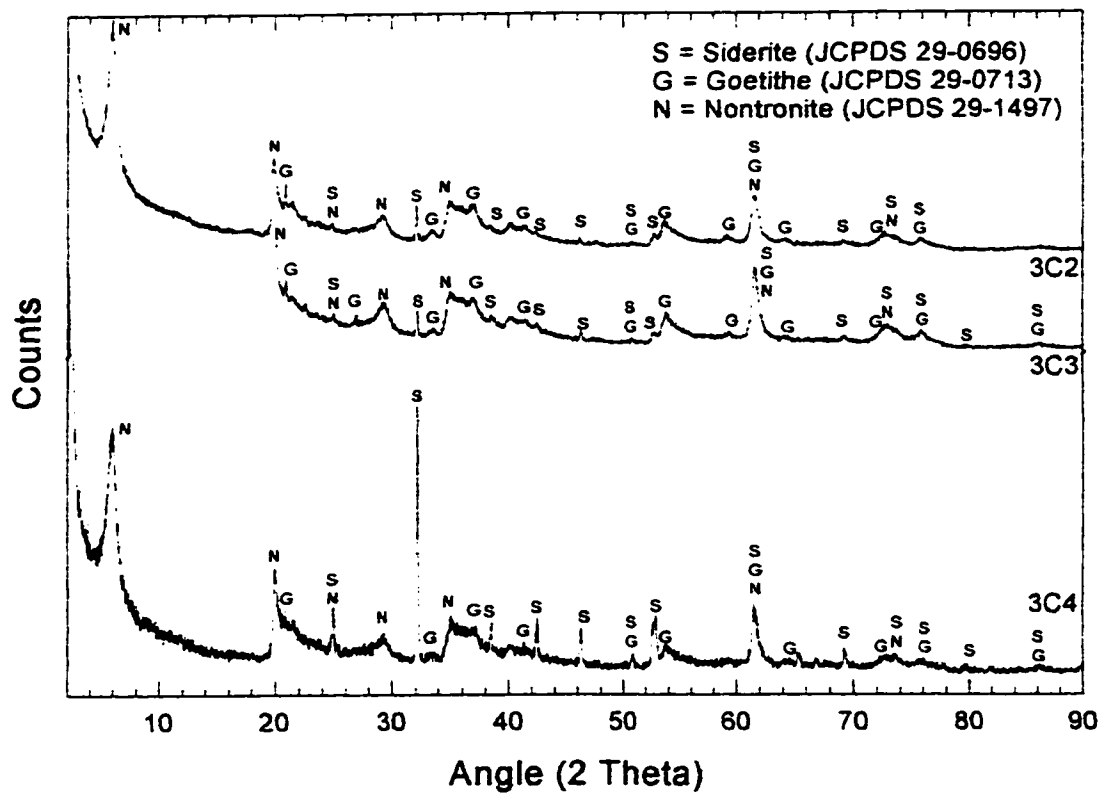


Figure 37. X-ray diffraction spectra for powdered 3C core samples.

CHAPTER 6

CONCLUSIONS

Isotopic data from SNC meteorites suggest the need for an on going mechanism of crustal-atmosphere exchange which *Jakosky and Jones* [1994] have attributed to active subsurface hydrothermal systems. It is generally assumed that CO₂ of the primitive Martian atmosphere was lost through a combination of escape to space and sequestering in the crust as carbonates. Geochemical models of indicate that hydrothermal mineralization could have been a highly effective means for sequestering carbonates in the early Martian crust. The abundance of carbonates present in Martian meteorite ALH 84001 indicates the possibility that disseminated carbonates may be quite abundant in the older crustal regions of Mars [*McKay et al.*, 1996]. The bulk composition of the Martian crust is thought to be primarily basaltic, and therefore enriched in Fe, Mg, and Ca. It is likely that solutes formed through hydrothermal circulation in the Martian crust would be comparatively enriched in these elements and that any carbonates precipitated from those solutions would tend to be Fe-rich varieties. This is consistent with the Fe-rich carbonates present in ALH 84001. While the temperature of formation of the carbonates in the meteorite is still uncertain, implicit in the ongoing debate over the biogenicity of features is the assumption of a hydrothermal origin.

Our ability to detect iron carbonate (siderite) in Mössbauer spectra of our Fe-spring samples from Chocolate Pots in Yellowstone underlines the potential importance of Mössbauer for the in-situ analysis of Martian crustal rocks during future landed

missions. A systematic search for Fe-carbonates in Martian rocks using Mössbauer spectroscopy would afford an opportunity to test the hypotheses discussed in this study regarding the evolution of the Martian atmosphere and climate.

The occurrence of siderite within our subsurface profiles at Chocolate Pots suggests a potentially important connection to the microbiology of the system. Carbonate precipitation has been shown to be biologically mediated as a result of pH increases induced by sulfate reduction (*Krumbein, 1979*). It is possible that a similar mechanism may account for the precipitation of Fe-carbonates within the deeper portions of our mat profiles. If the carbonates are being precipitated through biological controls, the isotopic signatures of the carbonates should reflect enrichment in the heavier isotope. It is also quite possible that these authigenic carbonates have captured microfossils or organic compounds as they precipitated.

XRPD provides the most definitive method for the determination of mineralogy. However, this technique requires the preparation of a powdered sample, which greatly increases the complexity and cost of an instrument payload for Mars. The most effective approaches for mineralogical identification are surface reflectance techniques that require only the exposure of a fresh rock surface. Backscatter x-ray methods have not been shown to provide definitive mineralogy, but our studies of Mössbauer spectroscopy with backscatter geometry indicate that the technique is quite reliable for determinative mineralogy.

This study shows that Mössbauer spectroscopy is capable of identifying a variety of materials associated with iron-rich deposits from terrestrial hydrothermal springs. There is evidence that these materials, and hence their spectral signatures, can be

preserved for billions of years. It is plausible that similar such material was produced in hydrothermal systems early on Mars. If this material survived to the present day and was investigated by an in situ Mössbauer spectrometer on the Martian surface, the likelihood that the instrument would yield evidence for the earlier hydrothermal system is very promising. It would thus have discovered a sample with compelling reason to be collected and returned to Earth for further investigation, including a search for fossils possibly contained therein.

APPENDIX A
THEORETICAL SUPPLEMENT

1. Siderite Model

As discussed in Chapter 2, the electric quadrupole splitting arises as a result of an interaction between the non-spherical charge distribution of the nucleus and an electronic environment of less than cubic symmetry. Usually, for most minerals, the quadrupole splitting will be much less than the magnetic hyperfine splitting, giving rise to an energy level diagram that corresponds to magnetically order spectra (“sextet”; Figure A1). In the spectrum, shown in Figure A2 for hematite, the quadrupole splitting manifests itself as the difference in separation between the peaks corresponding to transitions one and two and those corresponding to transitions five and six.

However, in the case of iron carbonate, which occurs naturally as the mineral siderite, the electric quadrupole splitting is comparable to or greater than the magnetic hyperfine (Zeeman) splitting. This phenomenon has been attributed to the relaxation effects in antiferromagnetic iron carbonates at low temperatures [Ok, 1969]. The corresponding energy level diagram (Figure A3) shows that the $\pm 3/2$ levels are shifted up in energy by $\frac{1}{2} QS$, while the $\pm 1/2$ levels in the excited state are shifted down in energy by $\frac{1}{2} QS$ where $QS > B_{hf}$, resulting in the possible overlap of energies of transition. Figure 29 shows a Mössbauer spectrum for natural siderite exhibiting this phenomenon.

2. Superparamagnetism

In magnetic theory, we look at the different interactions that can occur between atomic or nuclear moments (magnetic) and give rise to magnetic bulk properties. There are four main types of magnetism: ferromagnetism, antiferromagnetism, ferrimagnetism, and paramagnetism. In ferromagnetic coupling, the permanent atomic moments, which

are nearly aligned without any **B**-field, and the individual atomic moments are ordered (aligned and coupled) with each other, Figure A4a, where the net average atomic magnetic moment, **m**, is not 0. In antiferromagnetic coupling, the atomic moments are coupled with each other, but the alignment is anti-parallel and the net average atomic magnetic moment is zero (**m** = 0; Figure A4b). The most general case of magnetic coupling is that of antiferromagnetic coupling, where permanent moments are coupled with each other with anti-parallel alignment, and a nonzero net average atomic magnetic moment (**m** ≠ 0; Figure A4c).

In paramagnetism, individual atomic magnetic moments are no longer coupled (i.e., no exchange coupling interaction between moments) and, therefore, point randomly in all directions in space if applied field is zero (i.e., **B** = 0). In the presence of a weak magnetic field (**B** ≠ 0), individual moments interact not only with their environment but with other moments as well via thermal agitation while precessing about the axis of the magnetic field, **B** (Figure 42). The distribution of moments (i.e., energy states) is proportional to a Boltzmann factor. As the temperature is decreased and the B-field is increased, the moments become more nearly aligned with the **B**-field. This relaxation rate (time moment spends in any one energy state) is proportional to this Boltzmann factor given by the relationship

$$\text{Relaxation Rate} \propto e^{-\mu \cdot \mathbf{B} / kT} \quad (\text{A1})$$

where *k* is the Boltzmann constant, μ is the magnetic moment, and T is the temperature.

In superparamagnetism, permanent atomic magnetic moments experience exchange coupling with each other forming sub-domain size “clusters” of specific

volume, V_i (Figure A6). There is also coupling associated with several special crystalline easy axes (i.e., anisotropy) which lead to an anisotropy energy. Alignment of these clusters with crystal easy axes is dependent on two factors: a) the volume of clusters, and b) the temperature. Just as it was in the case of paramagnetism, there is a relaxation rate associated with the anisotropy of clusters that is proportional to a Boltzmann factor given by

$$\text{Relaxation Rate} \propto e^{-KV/kT} \quad (\text{A2})$$

where K is the anisotropy constant, V is the individual cluster volume, k is the Boltzmann constant, and T is temperature. If $KV \gg kT$, moments remain in particular directions (i.e., static). However, if $KV \ll kT$, the cluster moments flip quickly around the easy axes with a magnetic moment equal to the cluster moment but much, much greater than the atomic moment giving rise to the phenomenon known as super-paramagnetism.

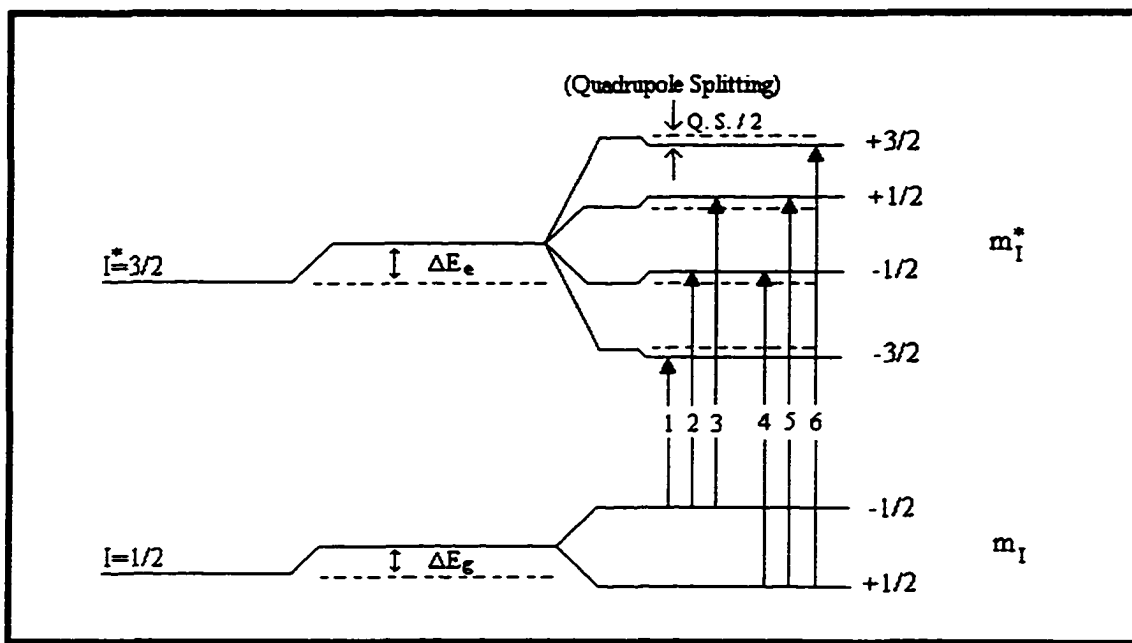


Figure A1. Energy level diagram showing combined isomer shift, electric quadrupole and magnetic hyperfine splitting.

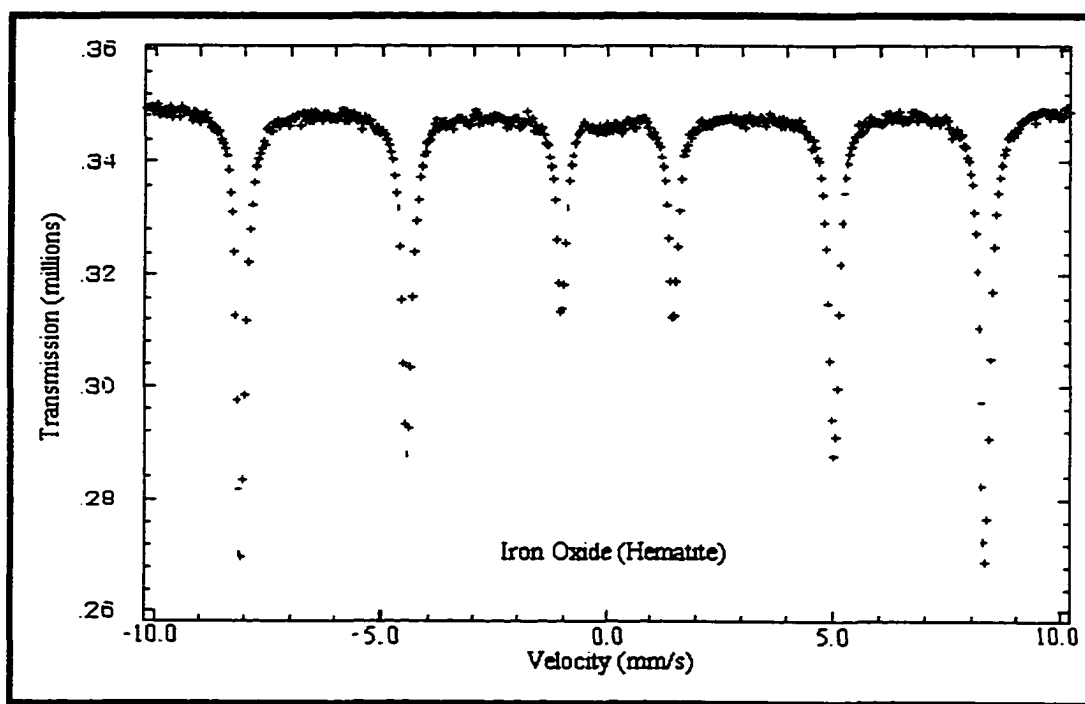


Figure A2. Mössbauer spectrum of iron oxide, hematite (Fe_2O_3)

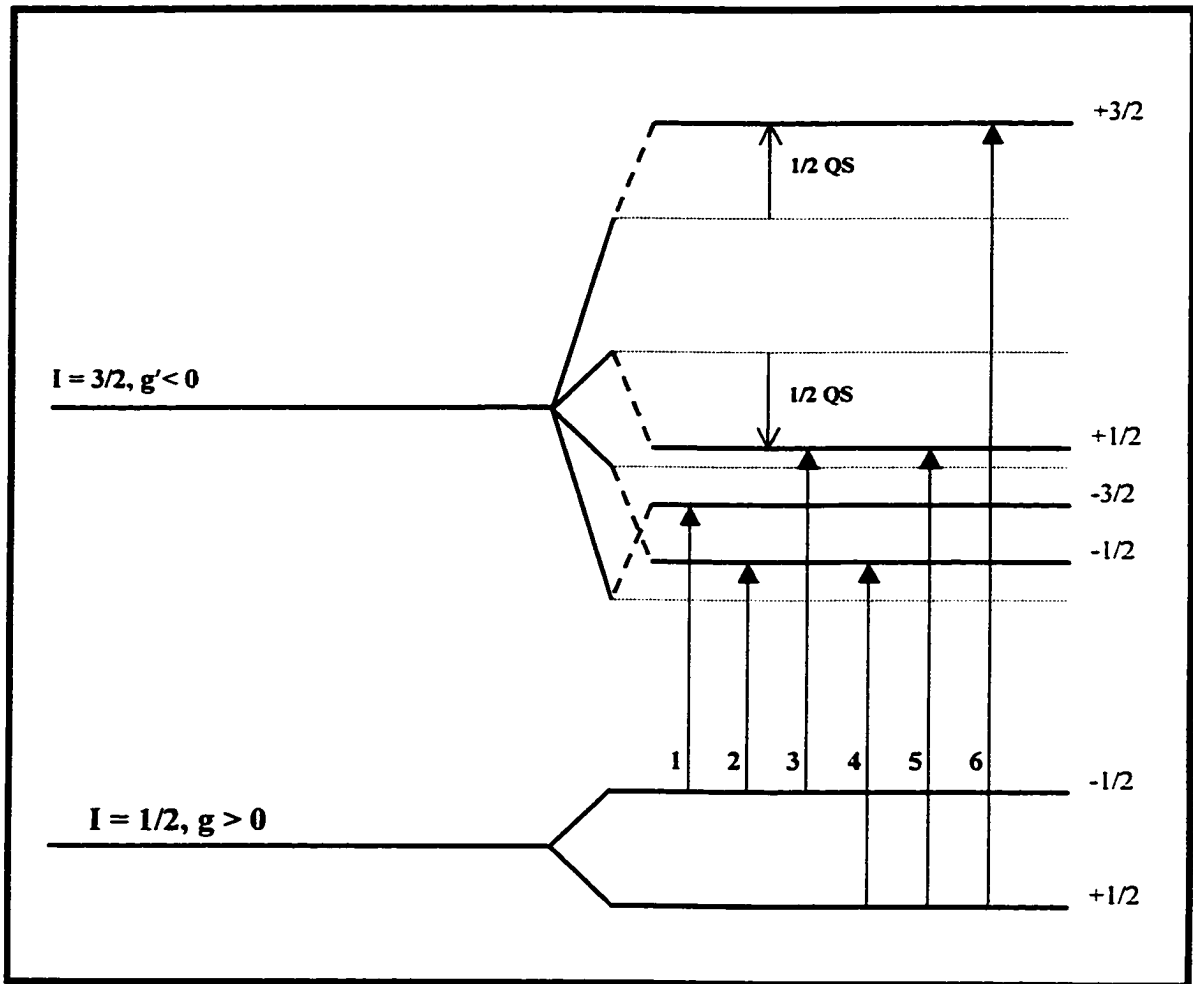


Figure A3. Energy level diagram showing the effect of a large quadrupole splitting compared to the magnetic hyperfine splitting.

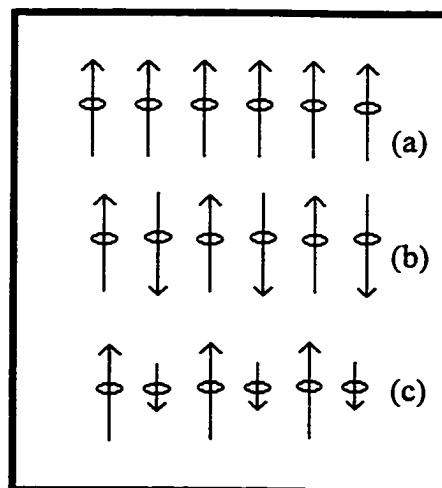


Figure A4. Diagram showing the moment coupling for (a) ferromagnetism, (b) anti-ferromagnetism, and (c) anti-ferrimagnetism.

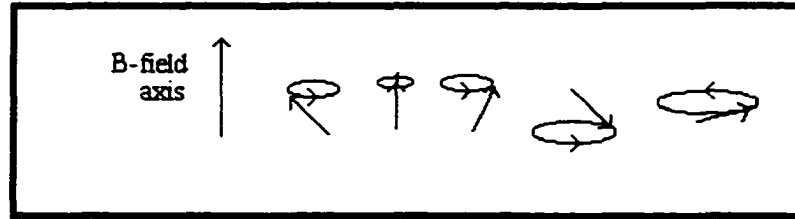


Figure A5. Diagram showing the precession of individual moments and interaction with adjacent moments for paramagnetism.

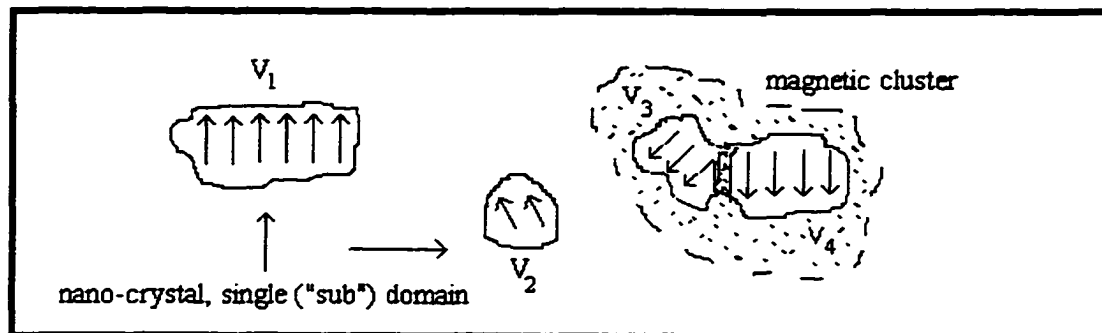


Figure A6. Diagram showing an example of nanocrystalline domains and the possible arrangement of these volume clusters.

APPENDIX B

X-RAY POWDER DIFFRACTION SPECTRAL ANALYSIS

In this section, the reference data tables used for mineral identification are given. Taken from the International Center for Diffraction Data card file database, the characteristic d-spacings and corresponding angles (2-theta) are given for the major components identified in each XRPD spectrum. Shown here are only those samples which showed non-amorphous signatures (samples 2C2-4 and 3C2-4), where unidentified peaks in the spectra may be attributed to the presence of hematite (Fe₂O₃), consistent with Mössbauer data and/or the possible presence of other silicates. These unidentified phases in the XRPD spectra will be addressed in future work.

Table 13. X-Ray Powder Diffraction Reference Data

Siderite (S), d-spacing	Siderite(S), angle (2 Θ)	Goethite(G), d-spacing	Goethite(G), angle (2 Θ)	Nontronite(N), d-spacing	Nontronite(N), d-spacing
3.5930	24.7512	4.9830	17.7797	15.2268	5.7976
2.7959	31.9742	4.1839	21.2116	7.4338	11.8916
2.3459	38.3256	3.3823	26.3199	4.4814	19.7888
2.1344	42.2963	2.6930	33.2307	3.5804	24.8397
1.9655	46.1310	2.5826	34.6953	3.0499	29.2491
1.7965	50.7624	2.4885	36.0514	2.5632	34.9663
1.7385	52.5831	2.4498	36.6410	2.5600	35.0114
1.7312	52.8220	2.2530	39.9718	1.5098	61.3322
1.5064	61.4857	2.1904	41.1651	1.3359	70.3994
1.4267	65.3322	1.9203	47.2820		
1.3970	66.9011	1.8020	50.5966		
1.3549	69.2697	1.7188	53.2329		
1.2824	73.8079	1.6905	54.1963		
1.2001	79.8307	1.5640	58.9915		
		1.5616	59.0912		
		1.5092	61.3593		
		1.4540	63.9579		

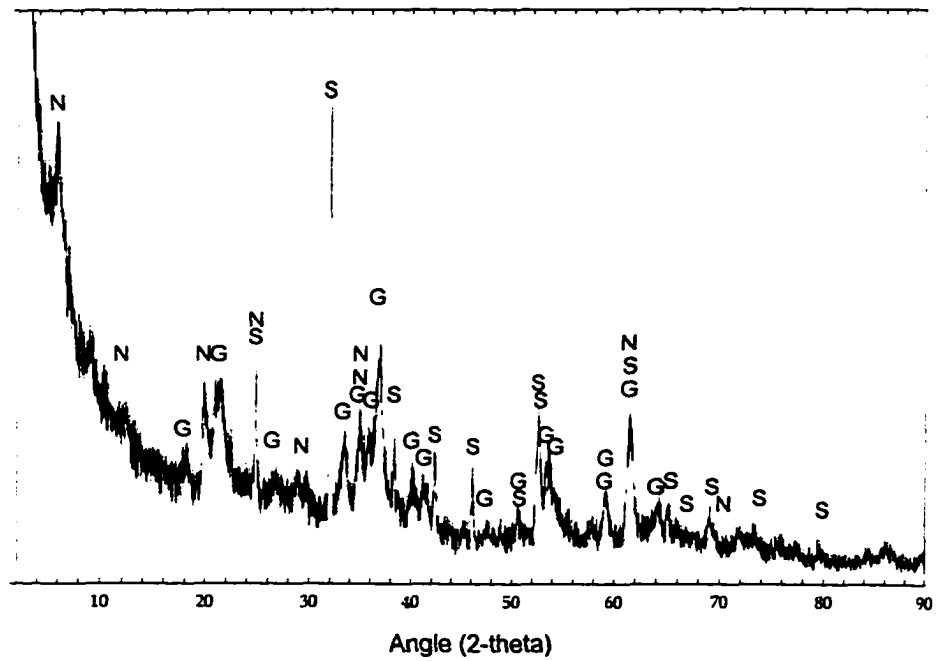


Figure B1. Powder x-ray diffraction spectrum for sample 2C2 with mineral assignments. (S) = Siderite; (G) = goethite; (N) = Nontronite

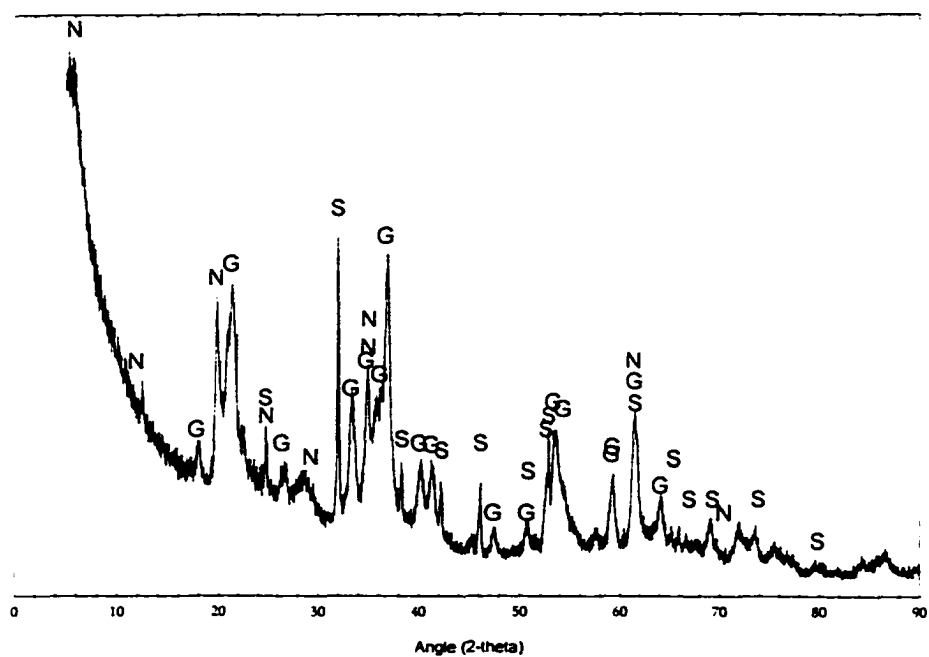


Figure B2. Powder x-ray diffraction spectrum for sample 2C3 with mineral assignments. (S) = Siderite; (G) = goethite; (N) = Nontronite

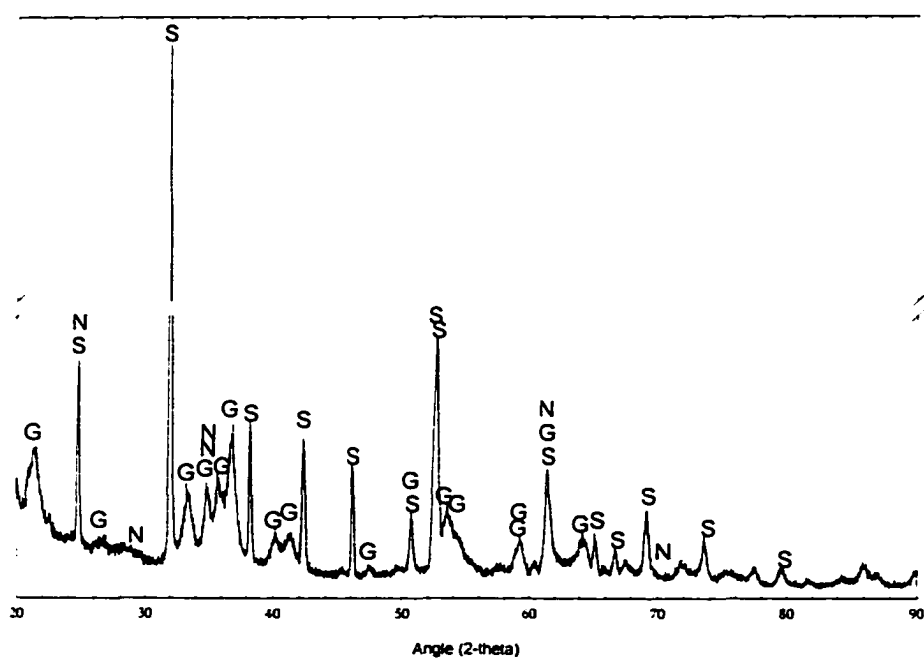


Figure B3. Powder x-ray diffraction spectrum for sample 2C4 with mineral assignments. (S) = Siderite; (G) = goethite; (N) = Nontronite

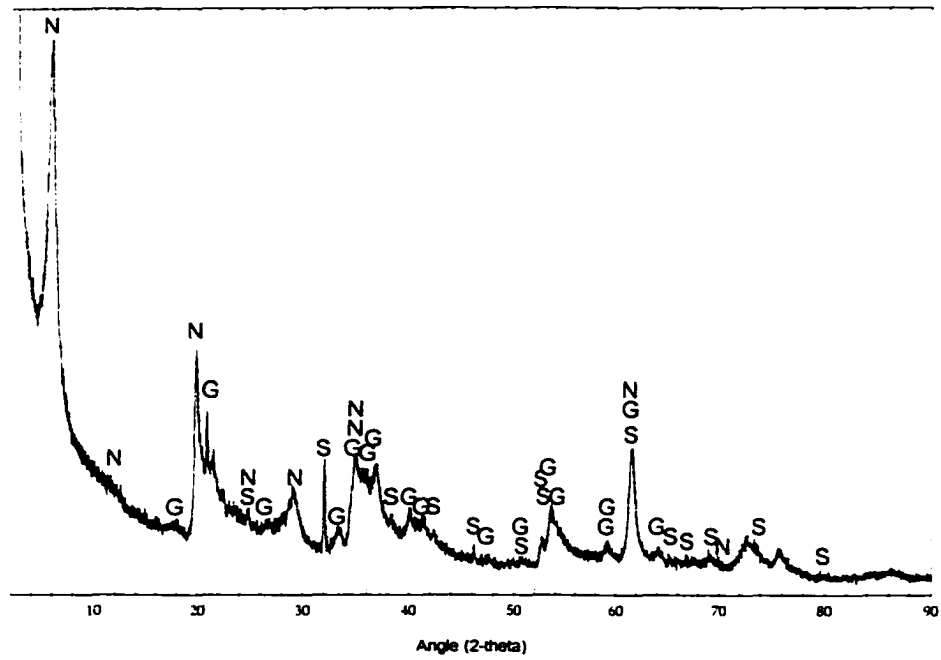


Figure B4. Powder x-ray diffraction spectrum for sample 3C2 with mineral assignments. (S) = Siderite; (G) = goethite; (N) = Nontronite

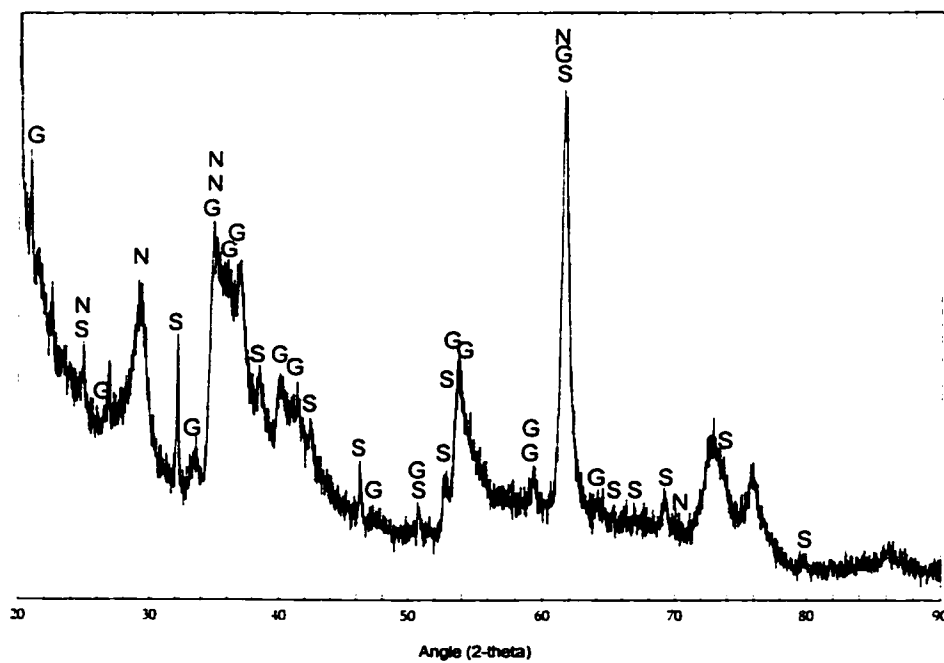


Figure B5. Powder x-ray diffraction spectrum for sample 3C3 with mineral assignments. (S) = Siderite; (G) = goethite; (N) = Nontronite

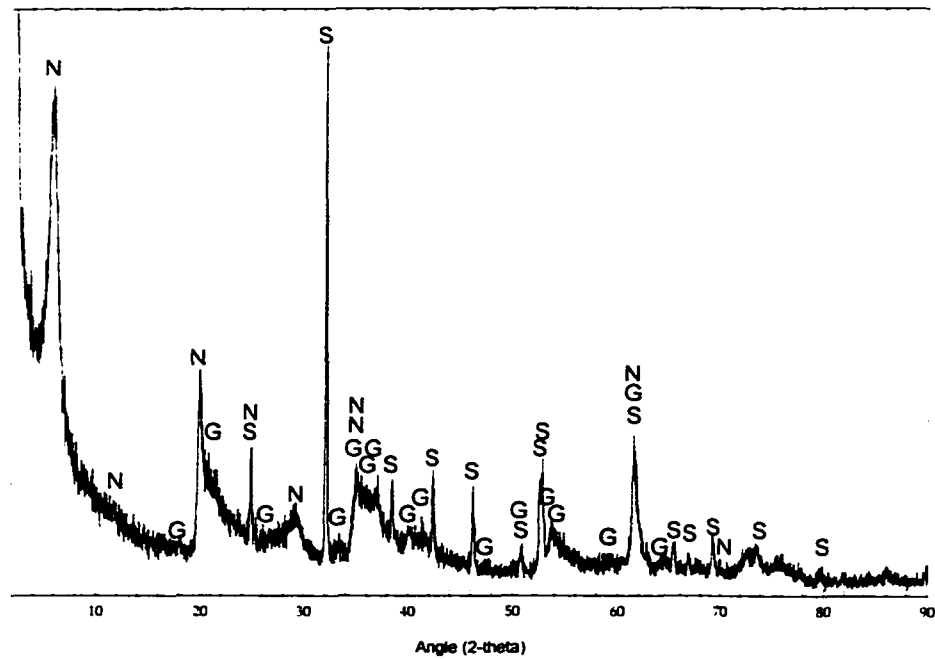


Figure B6. Powder x-ray diffraction spectrum for sample 3C4 with mineral assignments. (S) = Siderite; (G) = goethite; (N) = Nontronite

REFERENCES

- Agresti, D., M. Bent, and B. Persson, A versatile computer program for analysis of Mössbauer spectra, *Nucl. Instr. Meth.*, 72, 235-236, 1969.
- Agresti, D.G., and T.J. Wdowiak, Iron Mössbauer spectroscopy: Superparamagnetism in hydrothermal vents and the search for evidence of past life on Mars, in *Mars Surface and Atmosphere Through Time*, pp. 9-10, Technical Report Number 92-02, Lunar and Planetary Institute, Houston, 1992.
- Agresti, D.G., T.J. Wdowiak, and M.L. Wade, Mössbauer spectroscopy as a tool in the search for evidence of past life on Mars, *Hyperfine Interactions*, 91, 523-528, 1994.
- Agresti, D.G., T.J. Wdowiak, M.L. Wade, L.P. Armendarez, and J.D. Farmer, A Mössbauer investigation of hot springs iron deposits, *Lunar Planet. Sci.*, 26, 7-8, 1995.
- Agresti, D.G., T.J. Wdowiak, M.L. Wade, L.P. Armendarez and J.D. Farmer, Mössbauer spectroscopy of thermal springs iron deposits as Martian analogs. In *Conference on Early Mars: Geologic and Hydrologic Evolution, Physical and Chemical Environments, and the Implications for Life*, edited by S.M. Clifford, A.H. Treiman, H.E. Newson, J.D. Farmer, pp. 1-2, Lunar and Planetary Institute, Houston, LPI Contribution No. 916, 1-2, 1997.
- Alt, J.C., Hydrothermal/Bacterial oxide deposits on seamounts in the Eastern Pacific., *Mar. Geol.*, 81, 227, 1988.
- Banin, A., X.F. Han, I. Kan, and A. Cicelsky, Acidic volatiles and the Mars soil, *J. Geophys. Res.*, 102, 13,341-13,356, 1997a.
- Bancroft, G.M., *Mössbauer Spectroscopy: An instrument for Inorganic Chemists and Geochemists*, Halsted Press, Chicago, 1973.
- Bent, M.F., B.I. Persson, and D.G. Agresti, Versatile program for analysis of Mössbauer spectra, *Computer Phys. Commun.*, 1, 67-87, 1969.
- Baross, J.A., and S.E. Hoffman, Submarine hydrothermal vents and associated gradient environments as sites for the origin and evolution of life, *Orig. Life Evol. Biosph.*, 15, 327-345, 1985.

- Coe, J.M.D., Magnetic properties of iron in soil iron oxides and clay minerals, in *Iron in Soils and Clay Minerals*, edited by J.W. Stucki, B.A. Goodman, and U. Schwertmann, pp. 397-466, D. Reidel Publishing Company, Dordrecht, 1988.
- Corliss, J.B., J.A. Baross, and S.E. Hoffman, An hypothesis concerning the relationship between submarine hot springs and the origin of life on Earth, *Ocean. Acta*, 4, 59-69, 1981.
- Corliss, J.B., Hot springs and the origin of life, *Nature*, 347, 624, 1990.
- Erlich, *Geomicrobiology*, 646 pp., Dekker, Detroit, 1990.
- Farmer, J.D., Mars Exopaleontology, *Palaios*, 10, 197-198, 1995.
- Farmer, J.D., Hydrothermal Processes on Mars: An Assessment of Present Evidence, in *Evolution of Hydrothermal Ecosystems on Earth (and Mars?)*, edited by G.A. Bock and J.A. Goode, pp. 273-299, John Wiley and Sons, New York, 1996.
- Farmer, J.D., and D.J. Des Marais, Exopaleontology and the search for a fossil record on Mars, *Lunar Planet. Sci.*, 25, 367-368, 1994.
- Griffith, L.L., E.L. Shock, and R.E. Arvidson, Calculating the effects of hydrothermal alteration on Mars, *Lunar Planet. Sci.*, 26, 517-518, 1996.
- Jakosky, B.M., and J.H. Jones, Evolution of water on Mars, *Nature*, 370, 328-329, 1994.
- Joint Committee on Powder Diffraction Standards (JCPDS), *Mineral Powder Diffraction File Data Book*, JCPDS, Swarthmore, PA, 1980.
- Krumbein, *Biogeochemical Cycling of Mineral-forming Elements*, 612 pp., Elsevier, New York, 1979.
- Kündig, W., H. Bömmel, G. Constabaris, and R.H. Lindquist, Some properties of supported small α -Fe₂O₃ particles determined with the Mössbauer effect, *Phys. Rev.*, 142, 327-333, 1966.
- McKay, D.S., E.K.J. Gibson, K.L. Thomas-Keprta, H. Vali, C.S. Romanek, S.J. Clemett, X.D.F. Chillier, C.R. Maechling, and R.N. Zare, Search for past life on Mars: Possible relic biogenic activity in Martian meteorite ALH84001, *Science*, 273, 924-930, 1996.
- Mitra, S., *Applied Mössbauer Spectroscopy: Theory and Practice for Geochemists and Archaeologists*, 1-43, Pergamon Press, New York, 1992.

- Morris, R.V., D.G. Agresti, T.D. Shelfer, and T.J. Wdowiak, Mössbauer spectroscopy for mineralogical analysis on planetary surfaces, in *Proceedings, Pathfinder Sample Acquisition, Analysis, and Preservation Instrument Technology Workshop*, NASA, Houston, 1988.
- Morris, R.V., D.G. Agresti, T.D. Shelfer, and T.J. Wdowiak, Mössbauer backscatter spectrometer: a new approach for mineralogical analysis on planetary surfaces, *Lunar Planet. Sci.*, 20, 721-722, 1989a.
- Morris, R.V., D.G. Agresti, H.V. Lauer, Jr., J.A. Newcomb, T.D. Shelfer, and A.V. Murali, Evidence for pigmentary hematite on Mars based on optical, magnetic, and Mössbauer studies of superparamagnetic (nanocrystalline) hematite, *J. Geophys. Res.*, 94, 2760-2778, 1989b.
- Mørup, Steen, Magnetic hyperfine splitting in Mössbauer spectra of microcrystals, *J. Magnetism Magnetic Mater.*, 37, 39-50, 1983.
- Murad, Enver, Properties and behavior of iron oxides as determined by Mössbauer spectroscopy, in *Iron in Soils and Clay Minerals*, edited by J.W. Stucki, B.A. Goodman, and U. Schwertmann, pp. 309-350, D. Reidel Publishing Company, Dordrecht, 1988.
- Murad, E. and Bowen, L.H., The character of magnetic ordering in high-Al goethite and ferrihydrite, in *International Clay Conferences Abstracts*, p.163, Denver, 1985.
- Ok, Hang Nam, Relaxation effects in antiferromagnetic ferrous carbonate, *Phys. Rev.*, 185, 472-476, 1969.
- Ono, K., and A. Ito, A Mössbauer study of magnetic properties in ferrous compounds, 19, 899, *J. Phys. Soc. Japan*, 1964.
- Russell, M.J., A.J. Hall, A.G. Cairns-Smith, and P.S. Braterman, Submarine hot springs and the origin of life, *Nature*, 336, 117, 1988.
- Schwertmann, U., Occurrence and formation of iron oxides in various pedoenvironments, in *Iron in Soils and Clay Minerals*, edited by J.W. Stucki, B.A. Goodman, and U. Schwertmann, pp. 267-308, D. Reidel Publishing Company, Dordrecht, 1988.
- Shelfer, Tad D. Combined backscatter Mössbauer spectrometer / x-ray fluorescence analyzer (BaMS/XRF) for planetary surface materials, Ph.D. Thesis (University of Alabama at Birmingham, 1992).
- Sherman, D.M., and N. Vergo, Optical (diffuse reflectance) and Mössbauer spectroscopic study of nontronite and related Fe-bearing smectites, *Am. Mineral.*, 73, 1346-1354, 1988.

- Squyres, S., Mars Surveyor Athena Rover mission, Mössbauer instrument pages, on the Web at: <http://astrosun.tn.cornell.edu/athena/mossbauer.html>, 1998.
- Wade, M.L., *Synthesis and characterization of pure barium ferrite particles prepared by a new glycine-metal nitrate combustion method*, (University of Alabama at Birmingham Master's Thesis), 1991.
- Wade, M.L., Agresti, D.G., Wdowiak, T.J., Armendarez, L.P., Farmer, J.D., A Mössbauer investigation of iron-rich terrestrial hydrothermal vent systems: Lessons for Mars exploration, (submitted for publication, *J. Geophys. Res.*), 1998.
- Walter, M.R., and D.J. Des Marais, Preservation of biological information in thermal spring deposits: Developing a strategy for the search for a fossil record on Mars. *Icarus*, 101, 129-143, 1993.
- Wdowiak, T.J., and D.G. Agresti, Presence of a superparamagnetic component in the Orgueil meteorite, *Nature*, 311, 140-142, 1984.
- Wdowiak, T.J., D.G. Agresti, and J.D. Farmer, Mössbauer spectroscopy in the exploration for a Martian biosphere, in *Earth Observing Systems (EOS)/Supplement*, 76, 335, 1995.
- Whan, R.E., *Metals Handbook*, 9th. Edition, Volume 10, *Materials Characterization*, edited by Mills, K., Davis, J.R., Destifani, J.D., Dieterich, D.A., Crankovic, G.M., Frissell, H.J., pp. 325-344, American Society for Metals, Ohio, 1986.

**GRADUATE SCHOOL
UNIVERSITY OF ALABAMA AT BIRMINGHAM
DISSERTATION APPROVAL FORM
DOCTOR OF PHILOSOPHY**

Name of Candidate Manson LaShawn Wade

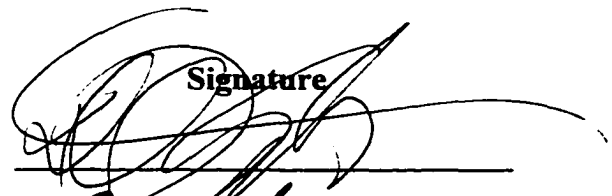
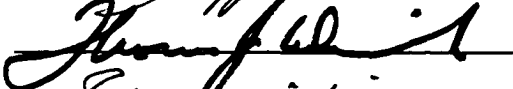

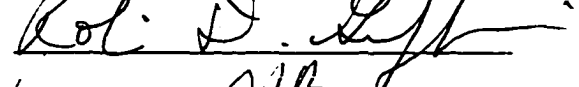
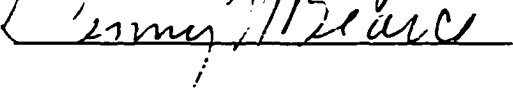
Major Subject Physics

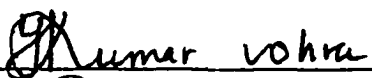
Title of Dissertation A Mossbauer Spectroscopic Study of Iron-rich Deposits

of Hydrothermal Springs as Martian Analogues

I certify that I have read this document and examined the student regarding its content. In my opinion, this dissertation conforms to acceptable standards of scholarly presentation and is adequate in scope and quality, and the attainments of this student are such that he may be recommended for the degree of Doctor of Philosophy.

Dissertation Committee:

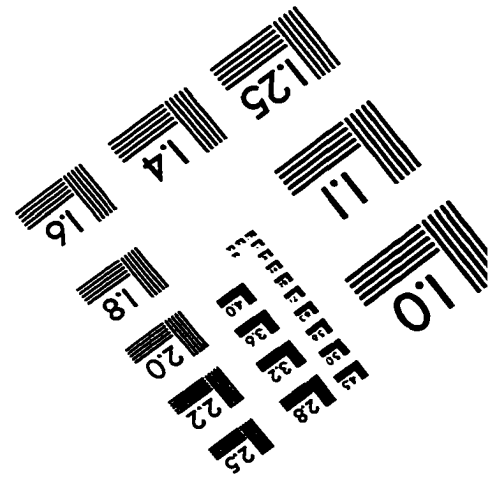
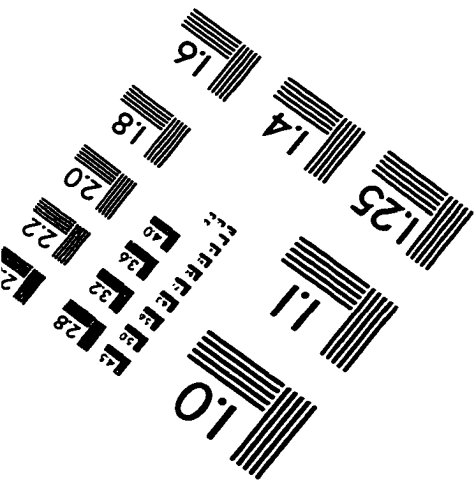
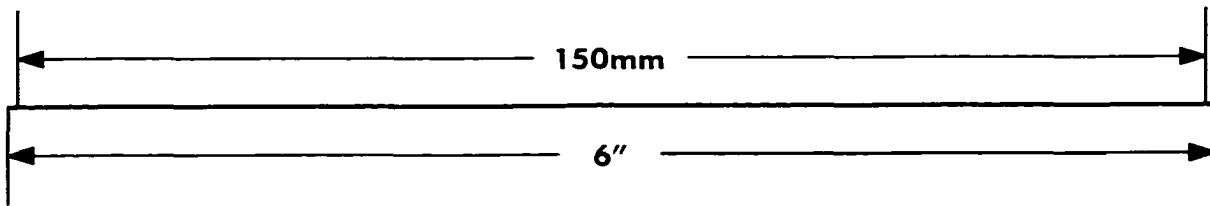
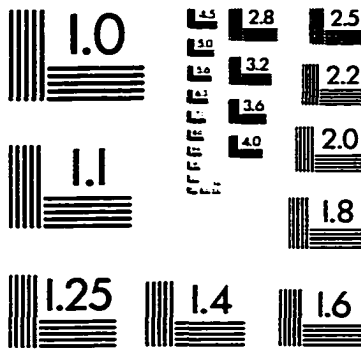
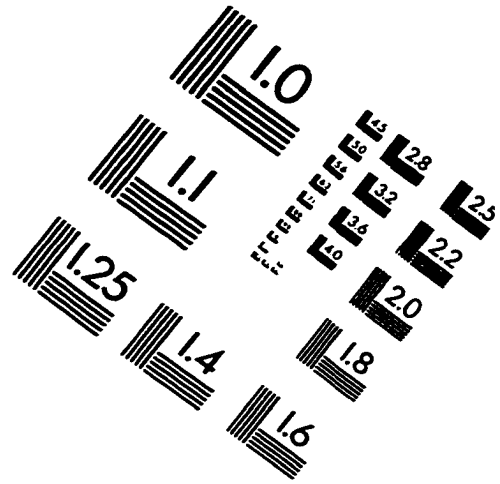
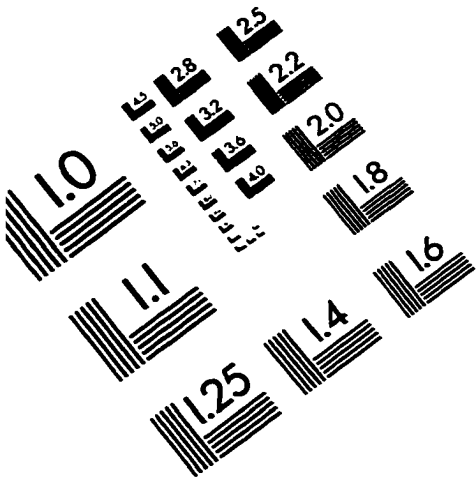
Name	Signature
<u>David G. Agresti, Ph.D.</u> , Chair	
<u>Thomas J. Wdowiak, Ph.D.</u>	
<u>Edward L. Wills, Ph.D.</u>	
<u>Robin D. Griffin, Ph.D.</u>	
<u>Denny N. Bearce, Ph.D.</u>	

Director of Graduate Program 

Dean, UAB Graduate School 

Date 4/16/99

IMAGE EVALUATION TEST TARGET (QA-3)



APPLIED IMAGE, Inc
 1653 East Main Street
 Rochester, NY 14609 USA
 Phone: 716/482-0300
 Fax: 716/288-5989

© 1993, Applied Image, Inc., All Rights Reserved